ECMWF COPERNICUS REPORT

Copernicus Atmosphere Monitoring Service

# Compendium of case studies for the period 2015-2018

Issued by: KNMI

Date: 4/12/2018

Ref: CAMS84_2015SC3_D84.7.2.1_casestudies_v1

IMPLEMENTED BY ECMWF

# Compendium of case studies for the period 2015-2018

***AUTHORS:***
N. Sudarchikova (MPG), S. Basart (BSC), E. Katragkou (AUTH), K. Petersen (MPG), D. Akritidis (AUTH), S. Kartsios (AUTH), P. Zanis (AUTH), D. Melas (AUTH), S. Chabrillat (BIRA-IASB), Y. Christophe (BIRA-IASB), M. Ramonet (LSCE), Y. Bennouna (CNRS-LA), H. Clark (CNRS-LA), A. Wagner (MPG), M. Schulz (MetNo), A.-M. Blechschmidt (IUP-UB), E. Cuevas (AEMET), H. Flentje (DWD), K. M. Hansen (AU), J. Kapsomenakis (AA), B. Langerock (BIRA-IASB), T. Warneke (UBC), H.J. Eskes (KNMI)

**REPORT OF THE COPERNICUS ATMOSPHERE MONITORING SERVICE, VALIDATION SUBPROJECT.**

**AVAILABLE AT:**
http://atmosphere.copernicus.eu/

***CITATION:***
Sudarchikova, N., S. Basart, E. Katragkou, K. Petersen, D. Akritidis, S. Kartsios, P. Zanis, D. Melas, S. Chabrillat, Y. Christophe, M. Ramonet, Y. Bennouna, H. Clark, A. Wagner, M. Schulz, A.-M. Blechschmidt, E. Cuevas, H. Flentje, K. M. Hansen, J. Kapsomenakis, B. Langerock, T. Warneke, H.J. Eskes, Compendium of case studies for the period 2015-2018, Copernicus Atmosphere Monitoring Service (CAMS) report, CAMS84_2015SC3_D84.7.2.1_casestudies_v1.pdf, December 2018.

***STATUS:***
Version 1, Final

***DATE:***
4/12/2018

## Summary

The Copernicus Atmosphere Monitoring Service (http://atmosphere.copernicus.eu, CAMS) is a component of the European Earth Observation programme Copernicus.

CAMS has an activity (CAMS-84) dedicated to the validation of the CAMS products made available to the user community. This activity provides validation reports for the CAMS-global real-time services, the CAMS-global reanalysis and evaluates the CAMS-regional service products focussing on concentrations above the surface. Most of these reports include case studies dedicated to large-scale or extreme events. One case study dedicated to the stratosphere-to-troposphere ozone transport over Europe has recently been published in the peer-reviewed literature (Akritidis et al., 2018).

This document contains a collection of these case studies, conducted during CAMS-84 phase 1 (2015-2018). Included are CAMS-global events like major wild fires, dust storms, greenhouse gas transport and the ozone hole, and CAMS-regional events like intrusions of stratospheric ozone-rich air into the troposphere, dust transport from Africa, and air pollution in the Mediterranean countries. Much of the material presented in this report is taken from the public validation reports. However, several case studies, in particular for the CAMS-regional system, have not been published before. The main aim of this report is to bring all these case studies together into one document. This provides a unique overview of the skill of CAMS in forecasting extreme events.

# Table of Contents

# 1 CAMS service components

## 1.1 Global CAMS system based on the ECMWF IFS model

The CAMS-global operational assimilation/forecast system for reactive gases and aerosols consists of the IFS-CB05 chemistry modules combined with the MACC aerosol model, further developed during CAMS. Apart from this CAMS provides high-resolution $CO_2$ and $CH_4$ forecasts and delayed-mode greenhouse gas analyses.

In the sections below we will use the following terms to refer to the global CAMS products:

**CAMS-global** or **o-suite**: These are names used for the main product of the operational global production system. Twice a day, CAMS issues a worldwide forecast of the composition of the atmosphere over the next five days. This is based on the ECMWF Integrated Forecast System (IFS) which contains modules to model the trace gases and aerosols in the atmosphere. To produce the CAMS global products, the model simulations are merged with satellite observations of the atmosphere (weather aspects as well as atmospheric composition) to ensure the forecasts are as accurate as possible.

**Control** run: An experiment which is identical to the o-suite, except that there is no assimilation of atmospheric composition satellite data. It is produced on a daily basis. This run is evaluated by the CAMS validation team and provides information on the improvements brought by the assimilation and uncertainties in the modelling of atmospheric composition.

**Reanalysis**: The reanalysis produced with the CAMS-global production system for the period 2003-2016, released in September 2018.

**Control** run for the reanalysis: An experiment which is identical to the reanalysis, except that there is no assimilation of atmospheric composition satellite data.

For more details on the different IFS configurations, satellite datasets assimilated, and the data products we refer to the CAMS website, e.g. https://atmosphere.copernicus.eu/global-products. An overview of the CAMS-global system is also provided in each of the "near-real time" validation reports, see the list of references.

**BASCOE**: An independent assimilation system for the stratosphere, developed by the Belgian institute BIRA-IASB, used to evaluate the stratospheric ozone product of CAMS-global.

**SDS-WAS Multi-model**: The CAMS simulations are also compared with dust preductions from an ensemble of models from the WMO Sand and Dust Storm Warning Advisory and Assessment System (http://sds-was.aemet.es/).

## 1.2 CAMS regional air quality forecasts

The European air quality forecast and analysis products are provided by the CAMS-regional activity, coordinated by Météo-France. The daily products are available in Near Real Time (NRT) and consist of four forecast days and one analysis day.

These NRT forecasts and analyses are produced by an ensemble of seven European air quality models: MOCAGE, LOTOS-EUROS, EMEP MSC-W, MATCH, EURAD-IM, CHIMERE and SILAM. From these 7 forecast and analysis runs an ensemble product is compiled, which is the main service product of CAMS-regional. This ensemble product is referred to as "**Ensemble**", "**CAMS-regional**" or simply "**ENS**" in the sections below.

Documentation about the seven models and the ensemble may be found on the CAMS website, e.g. http://www.regional.atmosphere.copernicus.eu.

Validation reports of the CAMS regional products are available at https://atmosphere.copernicus.eu/regional-services.

# 2 Major wild fire events

## 2.1 Fire events in Southeast Asia in April 2018

*Taken from the March-May 2018 NRT validation report [nrt2018a].*

A large number of fire events were detected during April in Southeast Asia. Fig. 2.1.1 represents some cases in mid-April. IASI shows an increase of CO emissions over East Asia on 11 April 2018, followed by a spreading and transport of the high concentration plume to the east on 14 and 15 April. Both CAMS-global e-suite and control capture locations of the emission plumes and transport pathway. Both runs seem to overestimate the emissions over the source regions, e.g. over India and underestimate CO values over the Pacific Ocean along the transport pathway.

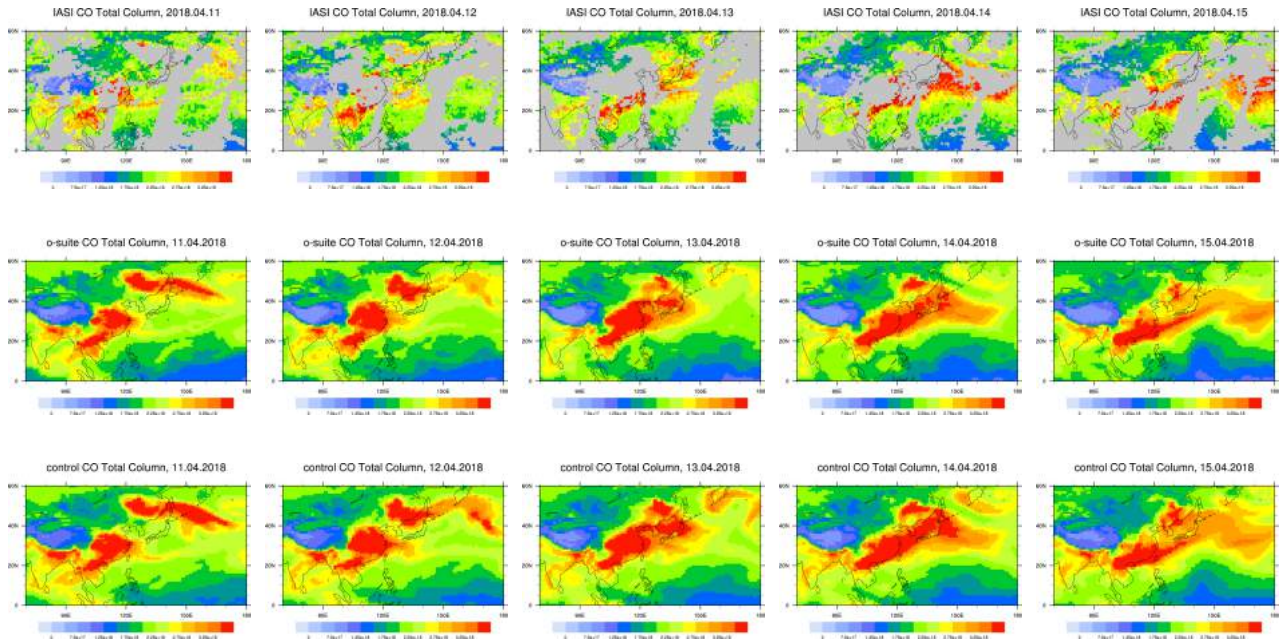


Fig. 2.1.1. CO total column for IASI (top), o-suite (middle) and control runs (bottom) from 11-15 April 2018 over the region of East Asia.

## 2.2 Rapid increase of modelled CO total columns in May 2018 over Alaskan and Siberian fire regions

*Taken from the March-May 2018 NRT validation report [nrt2018a].*

In May 2018, both, MOPITT and IASI instruments show high CO values over eastern China and northern India (more pronounced in IASI), Fig. 2.2.1. Additional to these plumes the modelled data from CAMS-global e-suite and control indicate a high CO spot over the Siberian fire region which is not represented in the satellite data. The control run has also high CO values over Alaskan fire region and along the transport pathway towards North America.

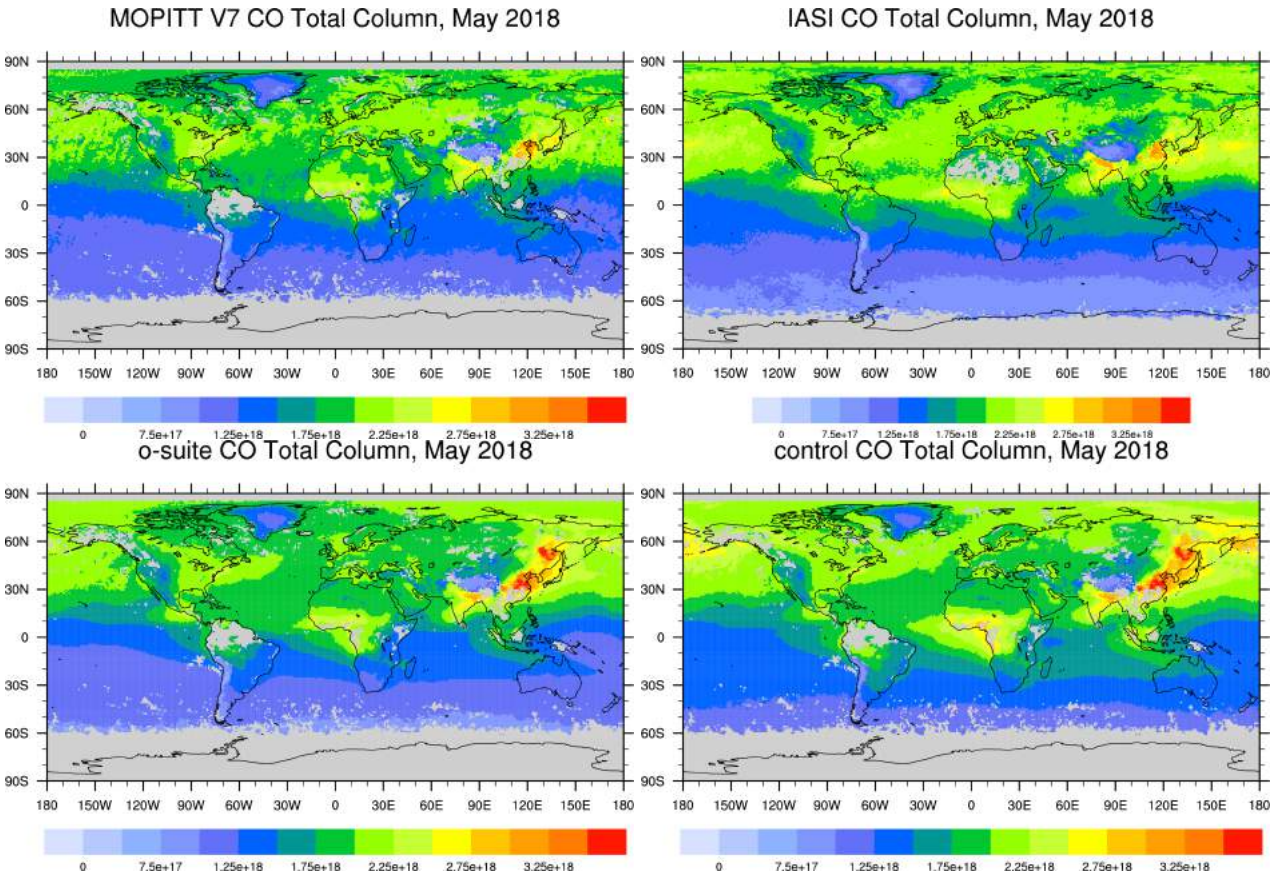


Fig. 2.2.1 CO total columns for MOPITT v7 (left), o-suite (middle) and control (right) runs for May 2018.

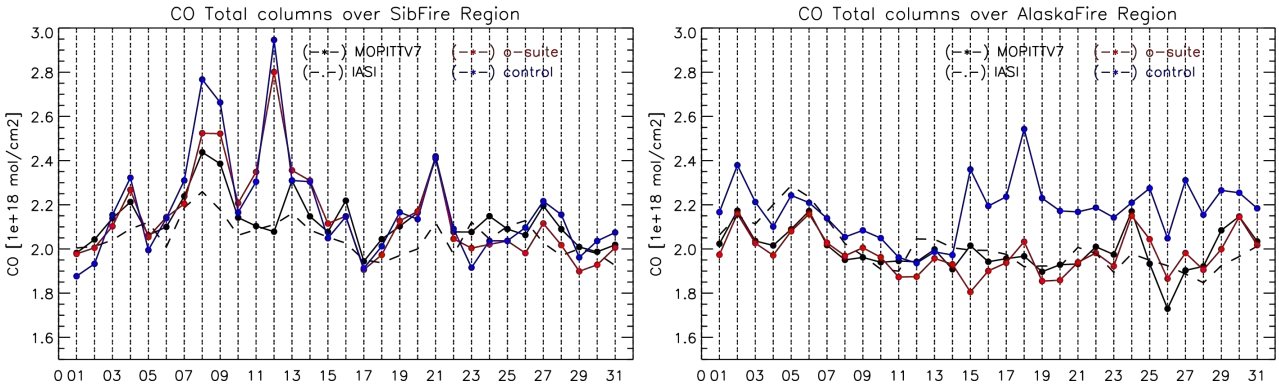


Fig. 2.2.2. Time series of CO total columns during May 2018 over Siberian (left) and Alaskan (right) regions from: MOPITT v7 and IASI (black), o-suite (red) and control (blue) runs.

Time series of CO total columns during May (Fig. 2.2.2) show that both the o-suite and the control run show a rapid increase of concentrations during 8, 9, 12 and 21 May over the Siberian fire region, which is inconsistent with the satellite observations. Over the Alaskan fire region, the o-suite is in good agreement with the satellite data, while the control run shows a rapid increase of CO starting from May 15 with continuously high values till the end of May.

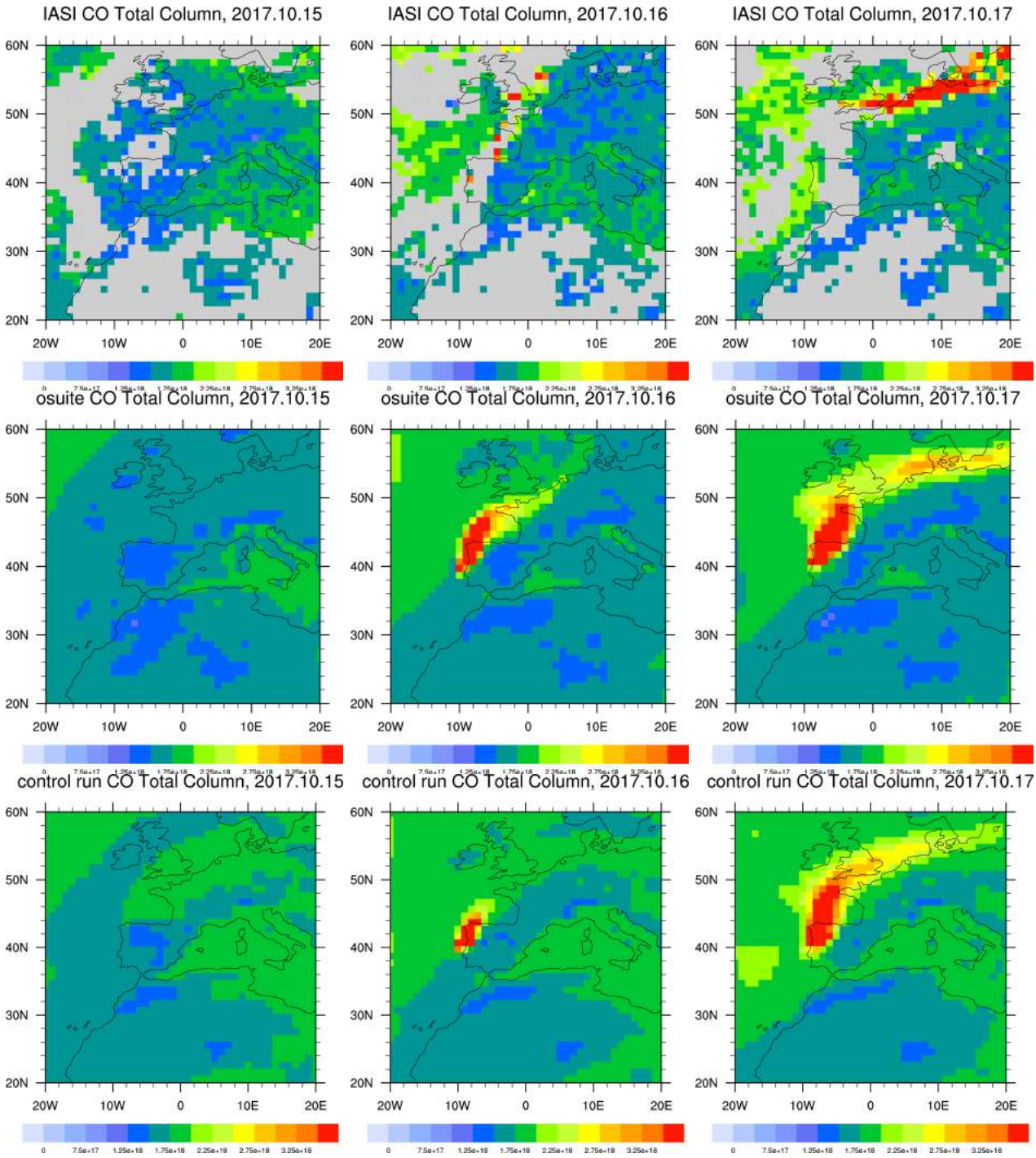


Figure 2.3.1. CO total columns for IASI observations (top row) with CAMS-global o-suite (middle row) and control run (lowest row) for October 15, 16 and 17, 2017.

## 2.3 Fires in Portugal and Spain, 14-17 October 2017

*Taken from the SON-2017 NRT validation report [nrt2018c].*

On the weekend of 14/15 October more than 140 wildfires broke out in central and northern Portugal and Galicia in Spain. The fires caused widespread devastation and more than 30 people were reported to have died,
(https://www.eumetsat.int/website/home/Images/ImageLibrary/DAT_3688467.html)

IASI data (Fig. 2.3.1) show rapidly increasing CO over the region starting from October 16th and north/northeastward transport across the ocean, but with many missing data points, especially over the location of the fire and the location of the plume. Both model simulations reproduce well the transport of CO as seen by IASI. The o-suite shows higher CO than the control run in the region of the fire. On the 17th October, the model has captured the location of the fire event, but underestimate the CO plume over northern Europe.

## 2.4 Fire case in Portugal, June 2017

*Taken from the JJA-2017 NRT validation report [nrt2017a].*

On 17 June 2017, lightning reportedly ignited a deadly wildfire that spread across the mountainous areas of Pedrógão Grande—a municipality in central Portugal located about 160 kilometers (100 miles) northeast of Lisbon (https://earthobservatory.nasa.gov/NaturalHazards/view.php?id=90427&src=nha). Fires across Portugal's forested landscape during the warm, dry summer months are not uncommon. In 2016, hundreds of fires raged on the mainland and also on the Portuguese island of Madeira. The high number of deaths associated with that fire in June, however, led *The New York Times* and other media to report it as "Portugal's worst forest fire in more than half a century."

IASI data show rapidly increasing CO over this region starting from June 18th and northwestward transport across the ocean, later on turning to north/northeast direction, but with many missing data points, especially over the location of the fire and the location of the plume (Fig. 2.4.1). Only two days after the fire has been reported, the CAMS system shows enhanced CO columns, with the o-suite showing higher CO than the control run in the grid box of the fire, while the control run shows higher CO everywhere else. Both model runs show very similar patterns in the transport of CO, but are not in good agreement with the observed CO total columns from IASI where data is available, and show less extended CO plumes than IASI.

This delay can to some extent be explained by the fact that the CAMS o-suite uses GFAS fire emissions from the day before. GFAS currently needs a full day of FRP observations to generate daily emissions and therefore the real-time modelling system has to rely on the emissions of the previous day. With the current development of GFAS to provide more timely hourly emission estimates, this issue will be (partly) mitigated.

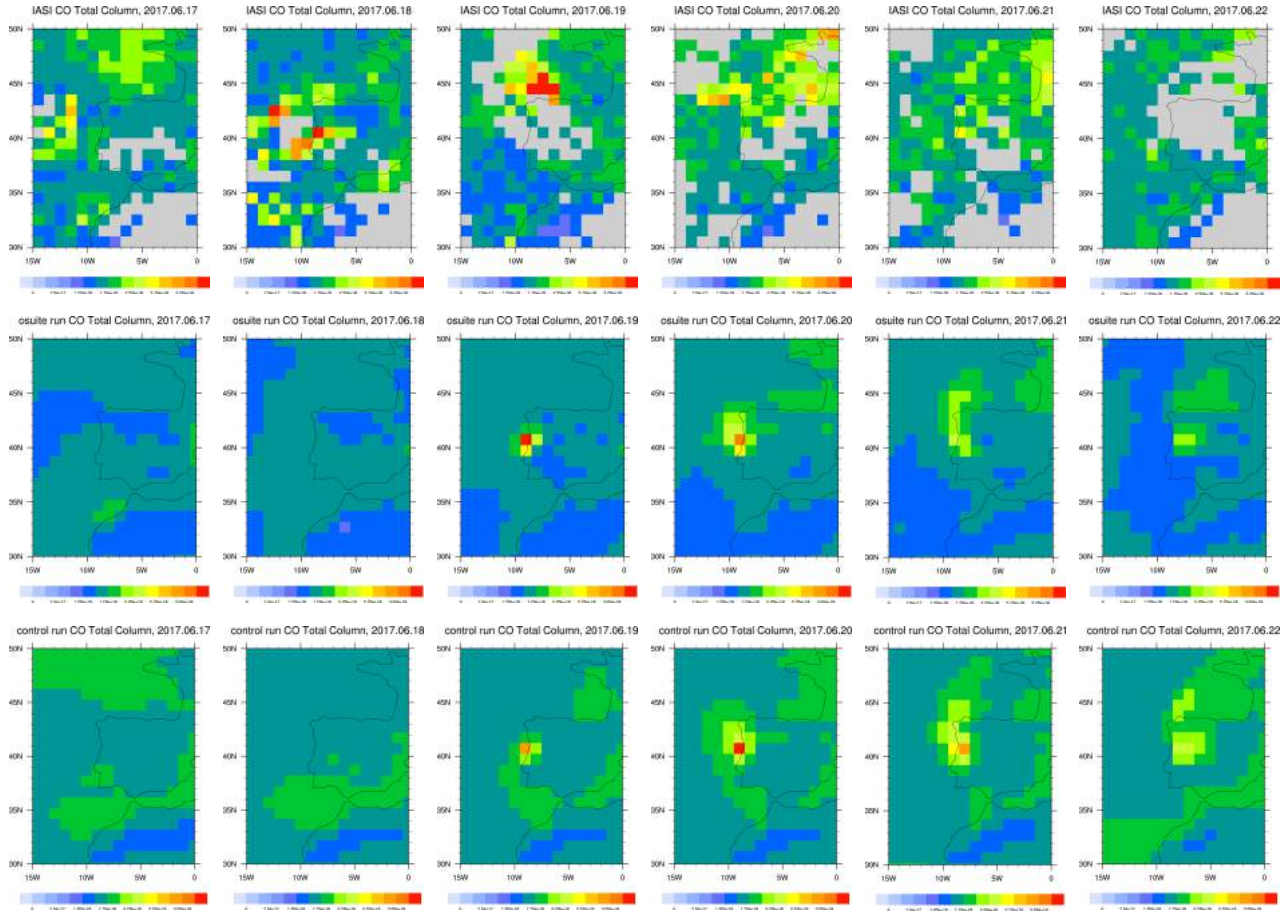


Fig. 2.4.1. CO total column for IASI (top), o-suite (middle) and control runs (bottom) over west Europe including Portugal.

## 2.5 Fire case in Siberia, June 2017

*Taken from the JJA-2017 NRT validation report [nrt2017a].*

Wildfires spread across southern Siberia in late June 2017. According to Russian state media, at least 27,000 hectares (100 square miles) were burning in the Irkutsk Oblast region. Another 27,000 hectares burned in neighbouring states and regions. More than 200 firefighters were sent to control the blazes. Dry lightning and human carelessness were cited as the causes of some of the fires (https://earthobservatory.nasa.gov/NaturalHazards/view.php?id=90470&src=nha).

IASI data show rapidly increasing CO over this region starting from June 21th followed by eastward transport (Fig. 2.5.1). Both model runs captured the location of the plume and the northwestward transport of CO. Pictures from both model runs show very similar patterns in the transport of CO, but higher values in the control run, while the o-suite run is in good agreement with the observed CO total columns from IASI.

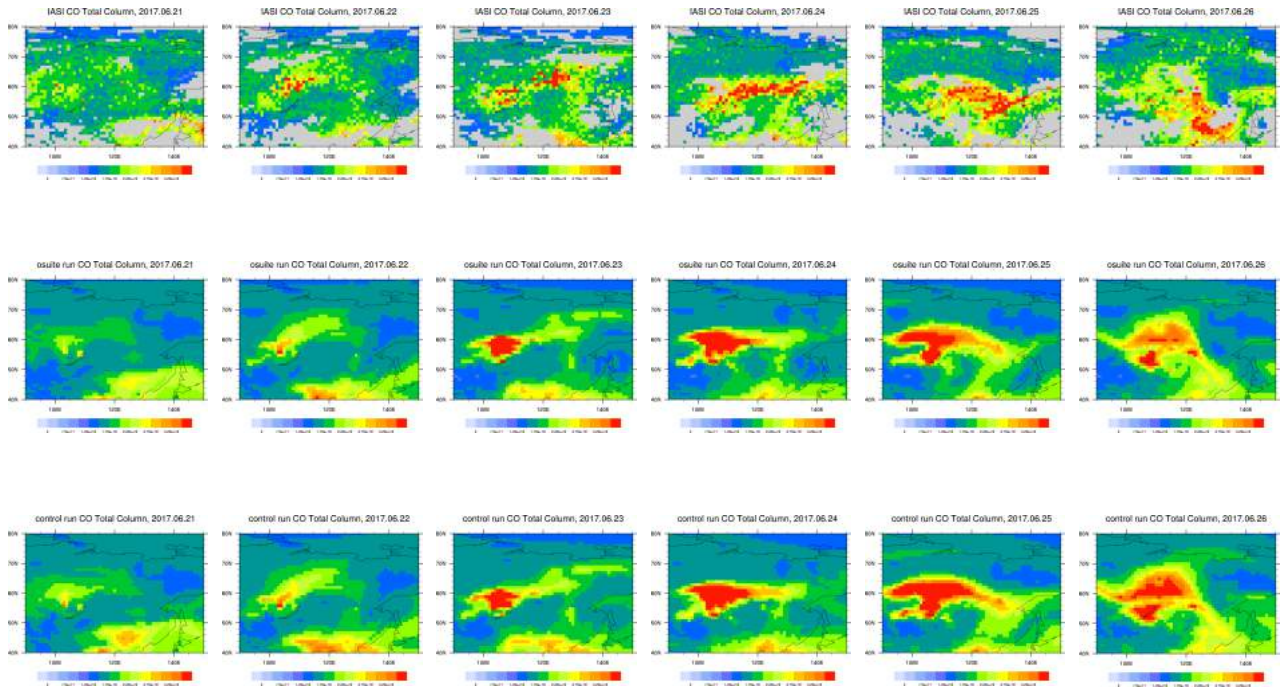


Fig. 2.5.1. CO total column for IASI (top), o-suite (middle) and control runs (bottom) over the area including Siberia.

## 2.6 Fire case in Canada, August 2017

*Taken from the JJA-2017 NRT validation report [nrt2017a].*

In August 2017, the widespread fires in British Columbia, that had been burning since July, flared up and sent a lot of smoke towards the North Pole. The smoke reached the Arctic Circle and from there skirted the top of Greenland to arrive in Europe. Another plume ducked south of Greenland and travelled across the Atlantic to rejoin the northern column. This smoke then persisted over Europe for more than a week (https://atmosphere.copernicus.eu/news-and-media/news/taking-heat-out-wildfire-prediction).

IASI data show a rapidly increasing CO plume over Canada and Alaska from August 10$^{th}$ with a maximum on the 15$^{th}$ August (Fig. 2.6.1). Both model runs captured the location of the plume and the northwestward transport of CO, as well as the magnitude of the CO plume. The control run is slightly higher than the o-suite, especially in the outflow of the plume.

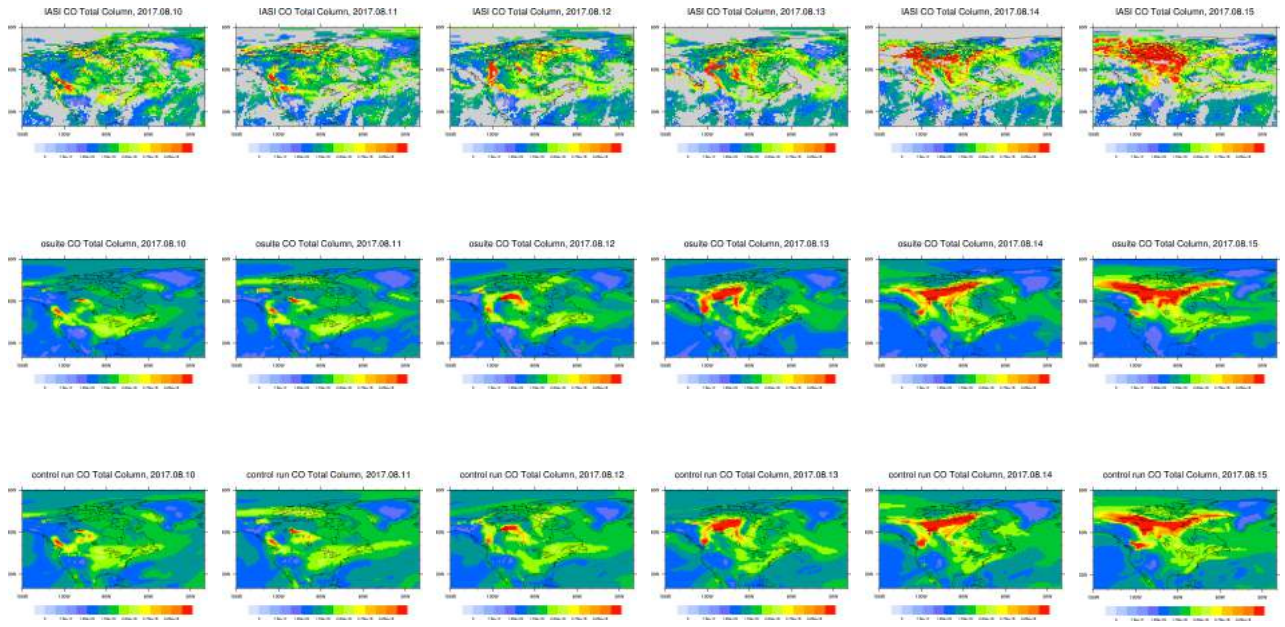


Fig. 2.6.1. CO total column for IASI (top), o-suite (middle) and control runs (bottom) over the area including Canada.

## 2.7 Fire case in Chile, South America in January 2017

*Taken from the DJF-2017 NRT validation report [nrt2017c].*

Wildfires, driven by strong winds, high temperatures, and long-term drought, have caused devastation across several regions of Chile in January 2017 as widely reported by the global media. From 1 July 2016 to 2 February 2017 approximately 3,000 fires have affected more than 575,000 hectares and 6,000 people (source: http://erccportal.jrc.ec.europa.eu/getdailymap/docId/1930, accessed 3 February 2017).

IASI data show rapidly increasing CO over this region starting from January 25 and northwestward transport across the ocean later on, but with many missing data points, especially over the location of the plume (Fig. 2.7.1). Both model runs captured the location of the plume and northwestward transport of CO. Pictures from both model runs show very similar patterns in the transport of the CO, but higher values in the control run, while the o-suite run is in good agreement with the observed CO total columns from IASI, where data is available.

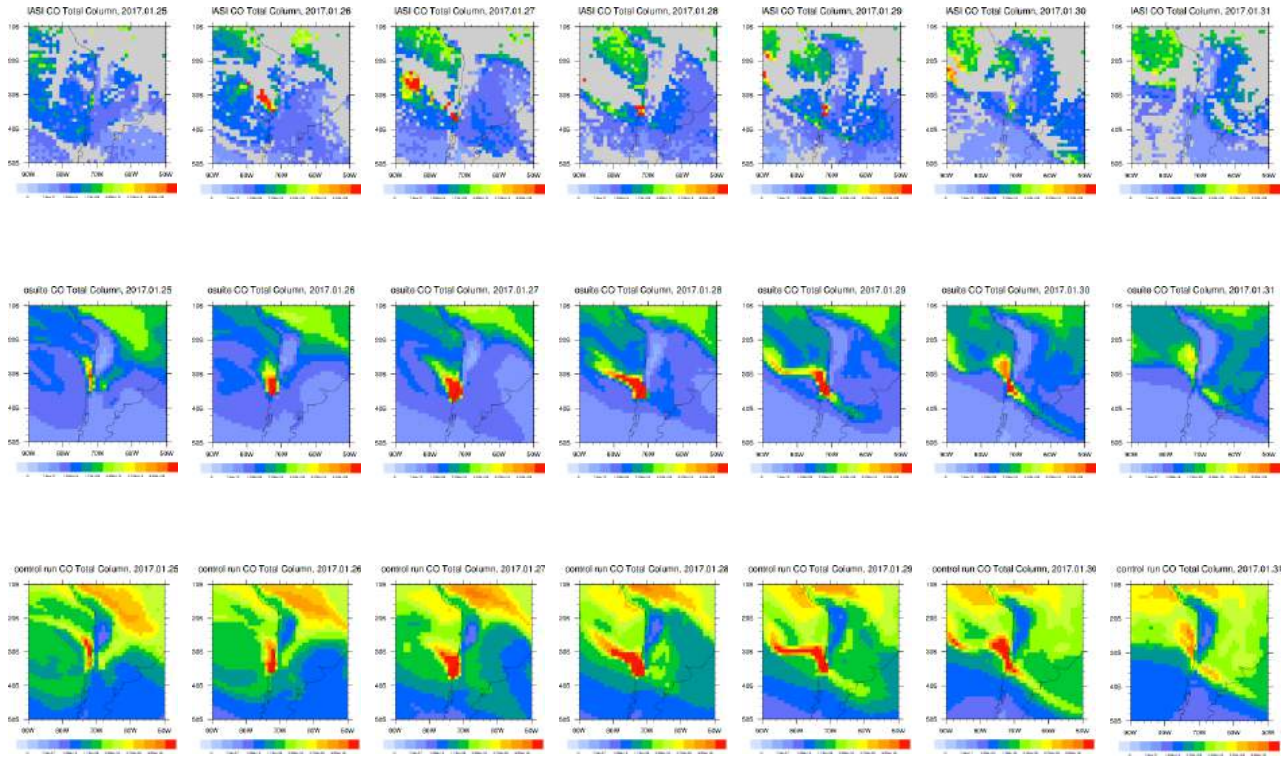

Fig. 2.7.1: CO total column from IASI (top), o-suite (middle) and control runs (bottom) for 25 to 31 January 2017 over the selected region.

## 2.8 Fire case in Siberia, Russian Federation in September 2016

*Taken from the SON-2016 NRT validation report [nrt2017d].*

Several big fire events took place in Siberia, Russian Federation, in September 2016. IASI data show rapidly increasing CO over this region starting from September 18 and eastward transport across the continent later on (Fig. 2.8.1). Both model runs captured the location of the plume and the eastward transport of CO. Pictures from both model runs are very similar with slightly lower values in the control run. In the beginning of the fire event, on September 18, both runs overestimated CO values in the plume, but show an underestimation in the transport pathway on September 23 and 25.

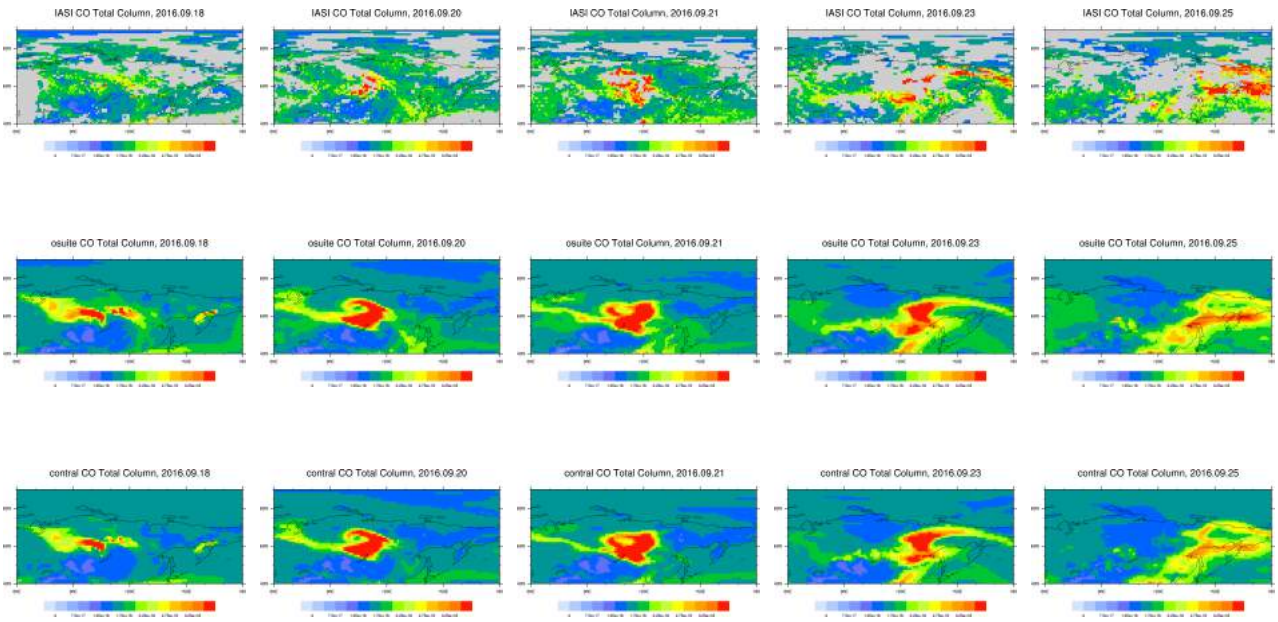


Fig. 2.8.1: CO total column from IASI (top), o-suite (middle) and control runs (bottom) for 18, 20, 21, 23 and 25 of September 2016 over the selected region.

## 2.9 Fire case in the central part of South America in late August 2016

*Taken from the JJA-2016 NRT validation report [nrt2016a].*

A fire event took place in the central part of South America during the 20$^{th}$ of August 2016. IASI measurements show a plume of CO over this region with south-east transport towards the Atlantic Ocean later on (Fig. 2.9.1). It is difficult to compare model results with IASI data for this case due to missing values, but it still can be seen that both model runs captured the location of the plume on 25$^{th}$ and 26$^{th}$ of August and south-east transport of CO on 29 and 30 August. CO values from both model runs are very similar and are in good agreement with the satellite data over the region of the fires and the transport plume in the grid boxes where data are present. Over the oceans the control run shows larger values than the satellite data.

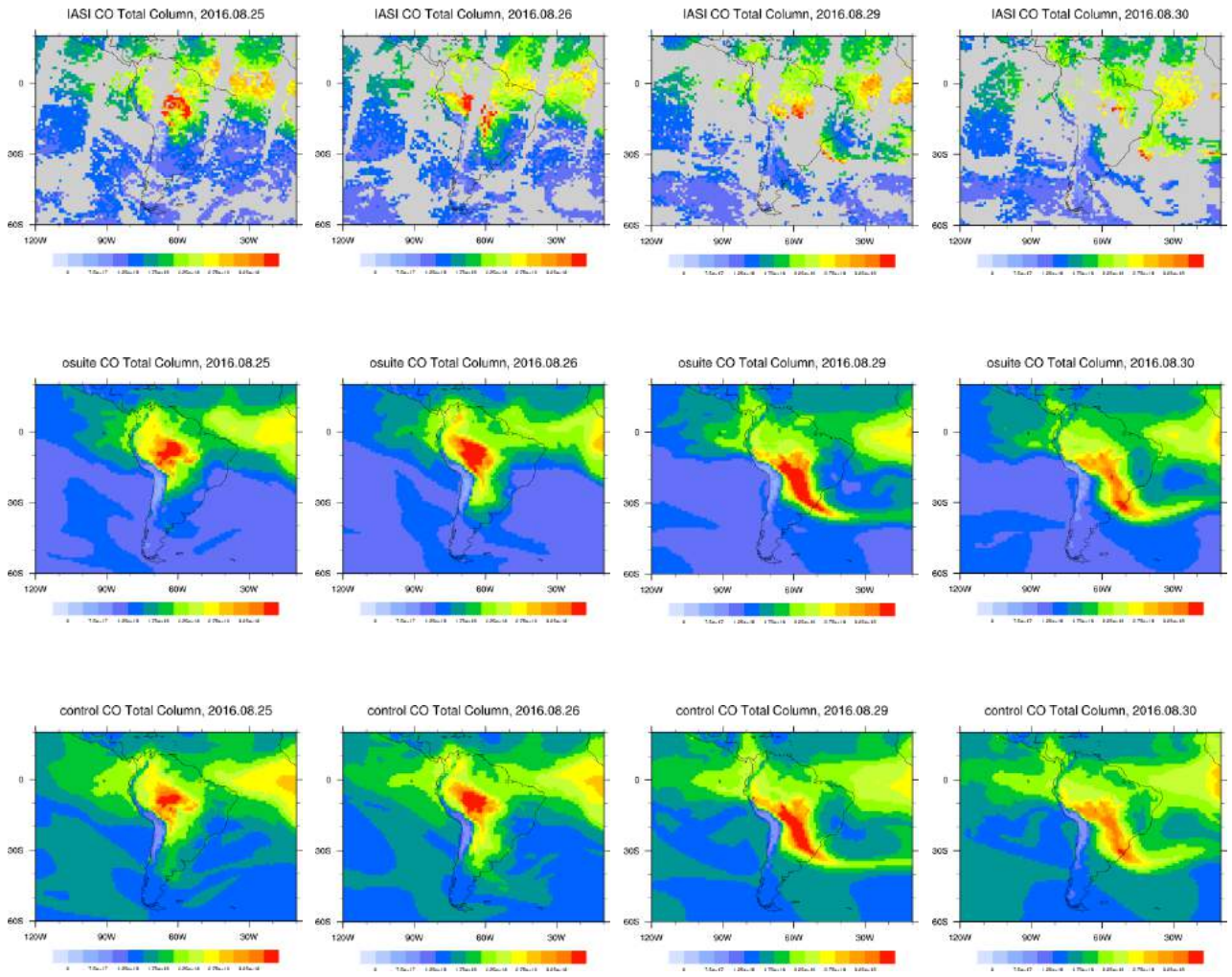


Fig. 2.9.1: CO total column from IASI (top), o-suite (middle) and control runs (bottom) for 25, 26, 29 and 30 of August 2016 over the selected region.

## 2.10 Fire case in the Far East of Russia in May 2016

*Taken from the MAM-2016 NRT validation report [nrt2016b].*

The Far East of Russia was affected by fires in May 2016, see also http://atmosphere.copernicus.eu/news-and-media/news/cams-monitors-siberian-wildfires-associated-warmest-month-record. Analysis of IASI measurements for one of these fires shows a clear plume of CO over this region, increasing with time and followed by a south-east transport towards the North Pacific Ocean (Fig. 2.10.1). Both model runs, o-suite and control run, captured the location of the plume and the transport of CO. Modelled CO values underestimate IASI data over the easternmost area of Russia and over the Ocean and overestimate satellite data over the Baikal Lake area. Two model runs are very similar. The difference can be seen over the very Far East and over the Ocean where the run without data assimilation shows slightly higher values which fits better with IASI data. Figure 2.10.2 shows a strong overestimation of $NO_2$ and HCHO fire emissions over east of Russia by the both model runs compared to the GOME-2 satellite data.

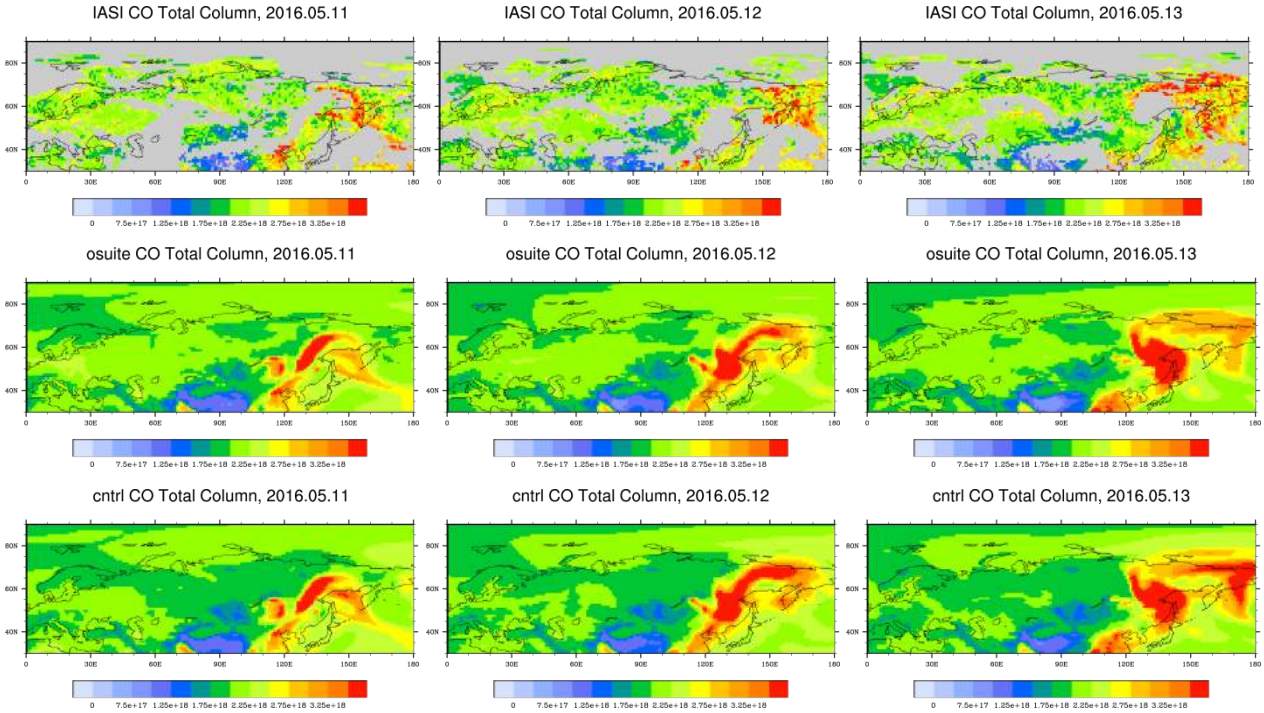


Fig. 2.10.1: CO total column from IASI (top), o-suite (middle) and control runs (bottom) for 11, 12 and 13 May 2016 over the selected region.

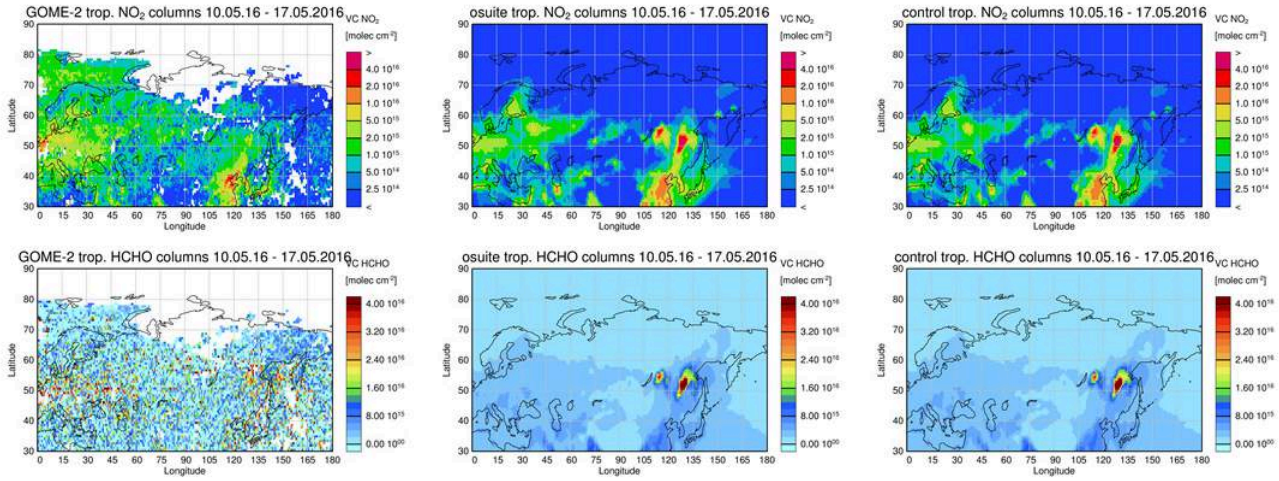


Fig. 2.10.2: Tropospheric $NO_2$ (top) and HCHO (bottom) columns from GOME-2 (left), o-suite (middle) and control runs (right) averaged for the time period 10-17 May 2016 over the selected region. GOME-2 data were gridded to model resolution (i.e. 0.75° deg x 0.75° deg). Model data were treated with the same reference sector subtraction approach as the satellite data.

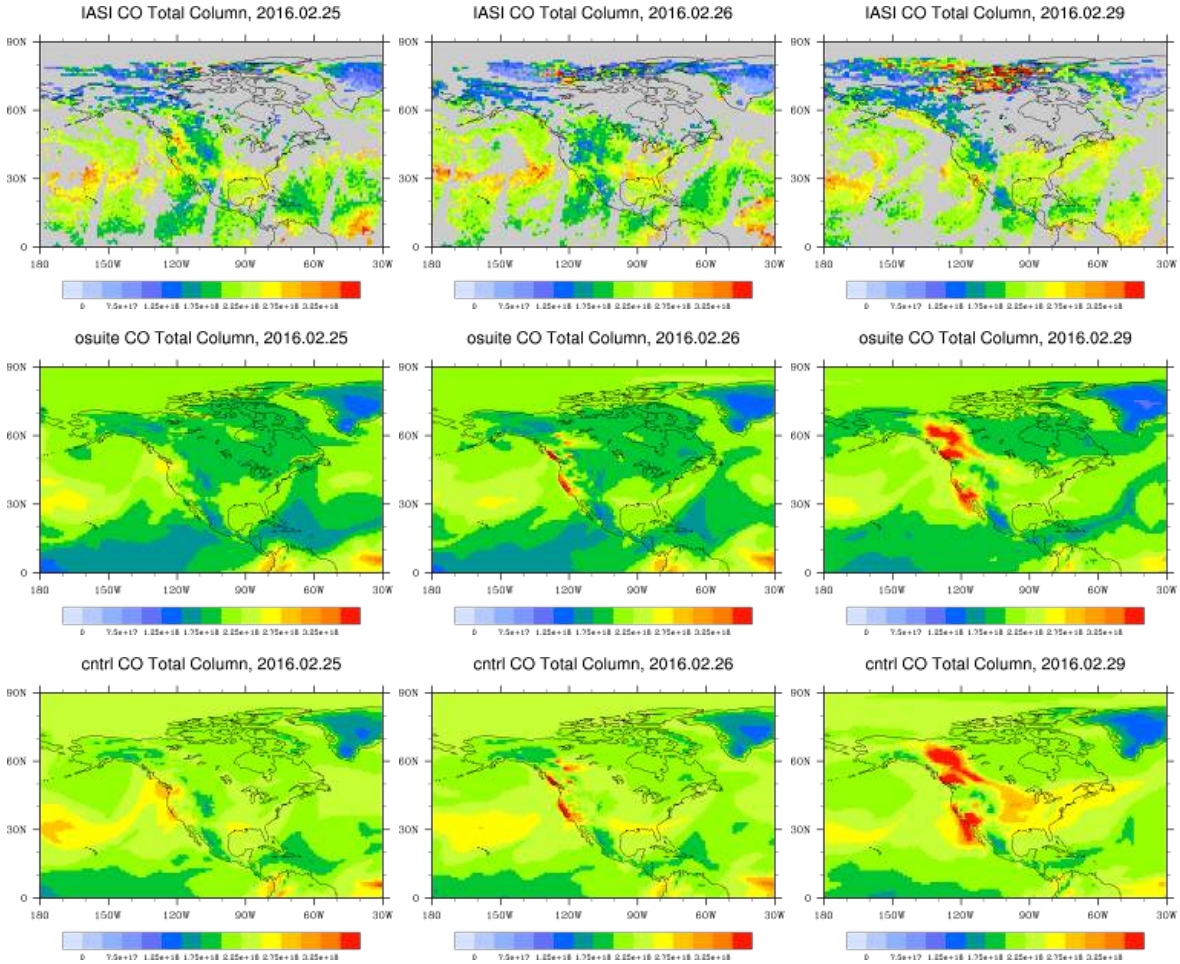


Fig. 2.11.1: CO total column from IASI (top), o-suite (middle) and control runs (bottom) for 25, 26, and 29 February 2016 over selected region.

## 2.11 A false CO plume over North America, end of February 2016

*Taken from the DJF-2016 NRT validation report [nrt2016c].*

On February 26 both o-suite and control indicated a plume with high CO values over Western part of US (Fig. 2.11.1). In the following days the air parcels with high CO concentrations spread to the east, over the American continent. As can be seen from the upper row of Figure 2.11.1, IASI retrievals does not show this high CO event. Also no fire events were found in this area for this time period. Note that there was no data available for the MOPITT and MODIS instruments from 18 February till 2 March 2016 due to an operational issue with the Terra satellite (https://www2.acom.ucar.edu/mopitt/news). The large modelled CO plume is an artifact of the erroneous GFAS fire emissions, caused by inaccurate TERRA-MODIS observations between 26 February and 1 March.

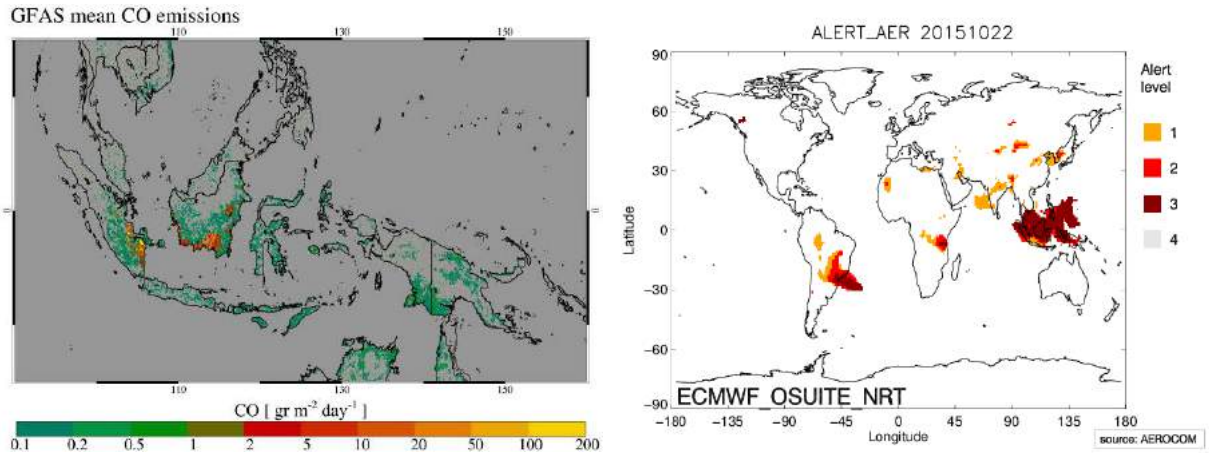


Fig.1.12.1 Left: Mean GFAS CO emissions during September-October 2015. Right: Aerosol alert map for 22 October 2015 derived from the o-suite.

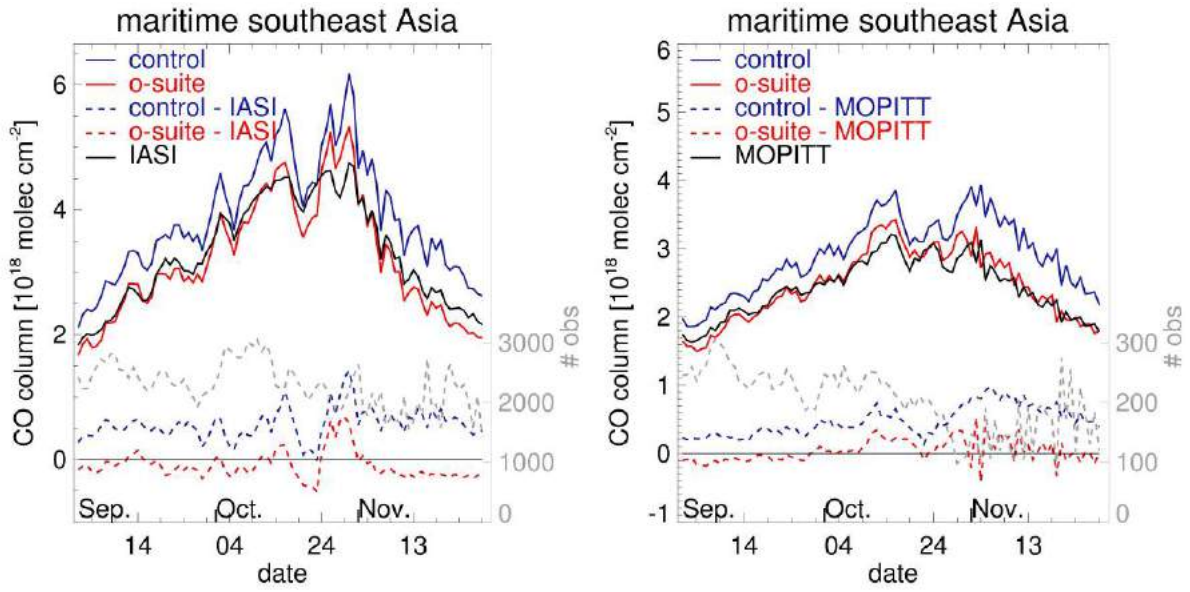


Fig.1.12.2 Time series of three-day running mean CO total column from model simulations and IASI (left) and MOPITT (right) satellite observations over a region including Indonesia and its outflow region over the ocean (70ºE-150ºE and 11ºS – 6ºN), and their biases (dashed lines). The scaled daily number of available observations (right axis) is given in gray.

## 2.12 Fires in Indonesia, September-October 2015

*Taken from the SON-2015 NRT validation report [nrt2016d].*

the year 2015 was marked by a strong El Niño event which intensified the dry season over large regions in Indonesia. September and October 2015 were characterized by the largest number of fire events in Indonesia since e.g. the start of the CAMS reanalysis (2003), and the emissions are likely the highest since the last large El Niño event from 1997 (see also http://atmosphere.copernicus.eu/news-and-media/news/smoke-and-carbon-emission-worsen-south-east-asias-fires). In Figure 2.12.1 the main fire emission regions over Sumatra and Borneo as

detected from the MODIS satellite instrument in September and October are shown. The corresponding aerosol alert map for the o-suite for 22 October 2015 shows daily mean aerosol optical depth simulated as being significantly larger than climatology, associated with the excessive aerosol loadings during this event.

Daily CO total columns from the model simulations over a region covering Indonesia (70°E-150°E and 11°S – 6°N) for September and October 2015 were compared to IASI and MOPITT data. Observations show an area-average increase of CO total column from ~ $2\times10^{18}$ molec $cm^{-2}$ in the beginning of September to ~ $4.5\times10^{18}$ molec $cm^{-2}$ in IASI and $3\times10^{18}$ molec $cm^{-2}$ in MOPITT by the end of October, Figure 2.12.2. Evaluation of model results shows that the o-suite CO total columns are in agreement with both satellite observations, considering that model sampling and averaging kernels lead to different model columns for MOPITT and IASI evaluations. The control run shows a growing positive bias by ~ 0.2 to 1.0 × $10^{18}$ molec $cm^{-2}$. At the end of October both o-suite and control runs overestimated IASI CO data, associated with a change in observation density due to growing cloud coverage. In this period, also the seasonal rains have started, extinguishing many of the fires. In November, the average CO columns decrease again to more normal levels.

The geographical distribution on 11, 13 September and 22, 25 October 2015 of the CO fire plume can be seen in Fig. 2.12.3. Note that this region is larger than the one shown on Fig.1.12.2. IASI data show a plume with very high values in September, but still largely confined to the Indonesian islands. In October, the air parcels with high CO concentrations is more spread, ranging from the Indian Ocean to the Philippine Sea. Both runs captured the location of the plume in September. In October, it can be seen that the o-suite better matches IASI over the land areas and shows underestimation over the Indian Ocean. The control run shows an overestimation over land, but better matches IASI over the Indian Ocean. Figure 2.12.4 suggests a net positive bias in GFAS CO emissions over Indonesia, mostly attributed to Sumatra, while negative biases in emissions appear over Borneo and West Papua.

Evaluation against HCHO suggests further that emissions used by the o-suite seem to be largely overestimated, resulting in model simulated HCHO columns which are almost twice as large as those retrieved by GOME-2. Note that a cloud flag (using only data with less than 20% cloud fraction) was applied to satellite retrievals shown in Figure 2.12.5 and model values correspond to these cloud-flagged regions only. This may potentially cause an underestimation in satellite retrieved values, if smoke plumes are incorrectly classified as clouds. However, further investigation using non-cloud-flagged satellite data and corresponding collocated o-suite data also shows the strong overestimation of the peak observed for September and October 2015, with satellite retrieved and o-suite values not very much larger compared to the cloud-flagged case.

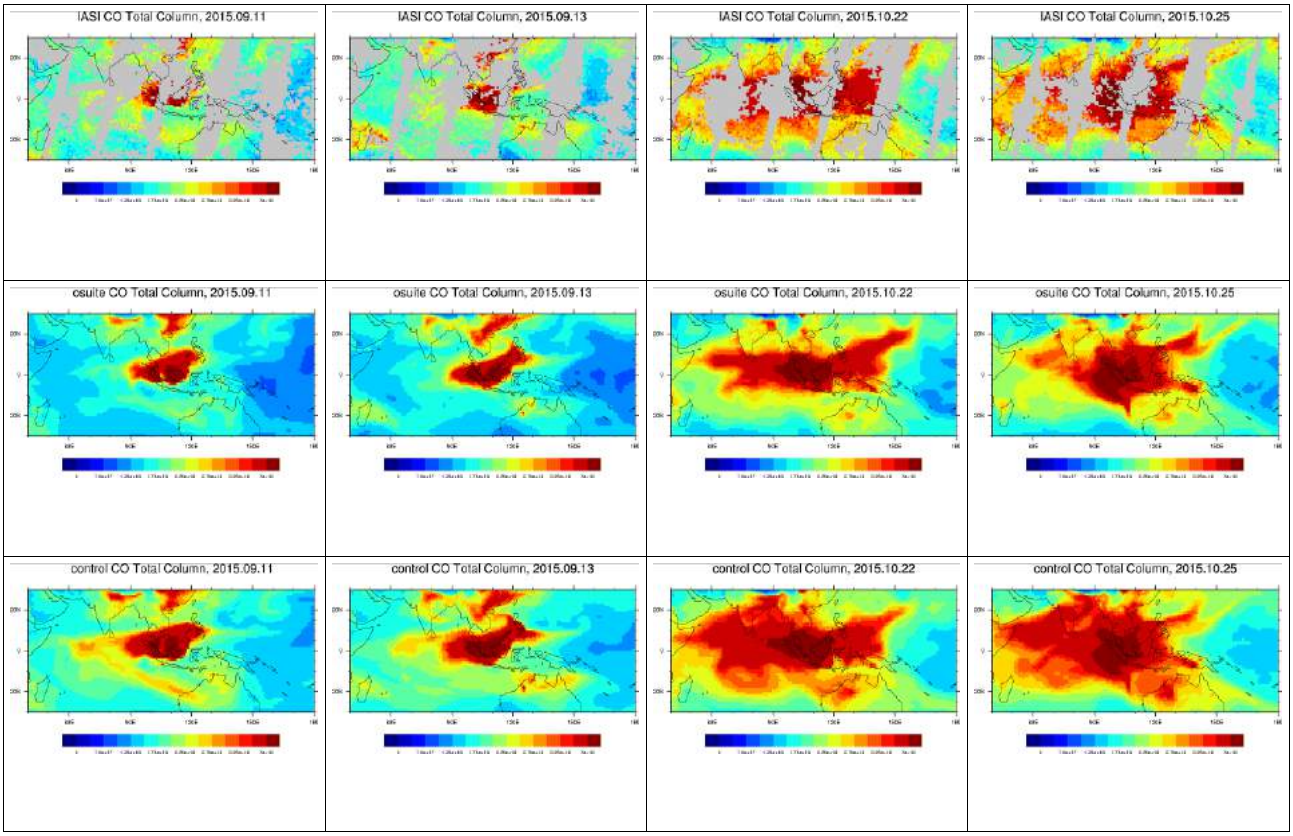


Fig. 2.12.3 CO total column from IASI (top), o-suite (middle) and control run (bottom) for 11, 13 September and 22, 25 October 2015 over the selected region.

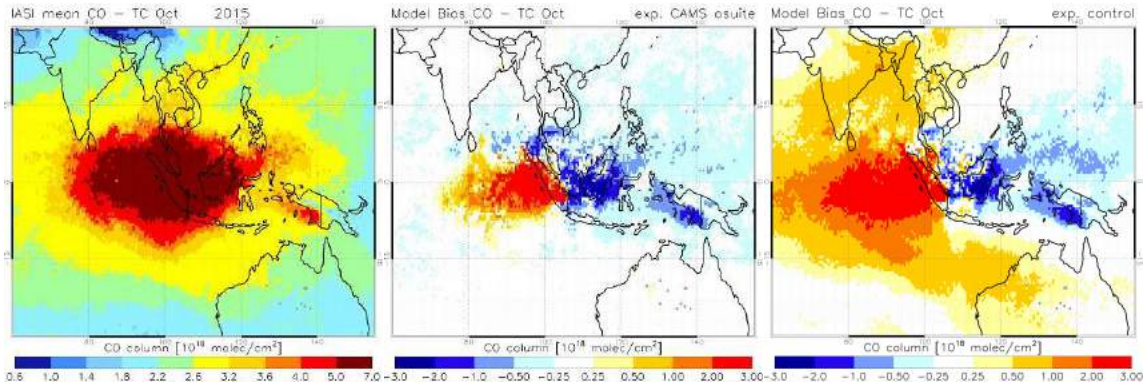


Fig. 2.12.4. IASI monthly mean CO total column (left), and corresponding bias for o-suite (middle) and control (right), for October 2015.

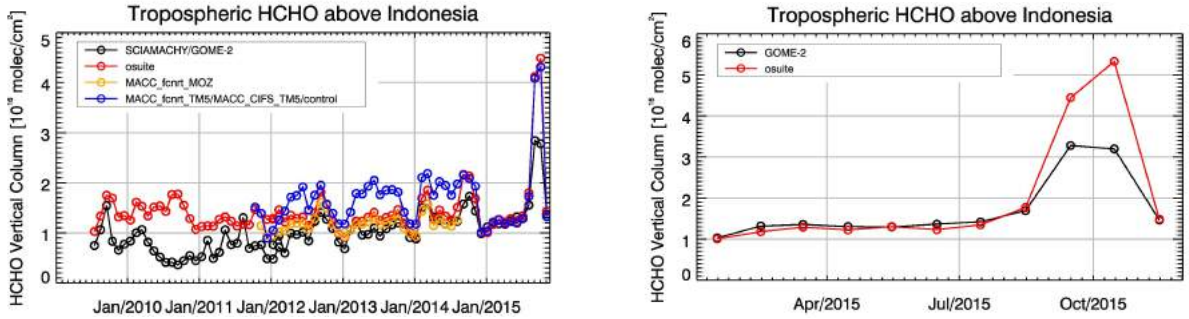


Figure 2.12.5: Left: HCHO time series over Indonesia, filtered for clouds. Right: o-suite HCHO without cloud-flagged data over Indonesia for 2015. See text for further details.

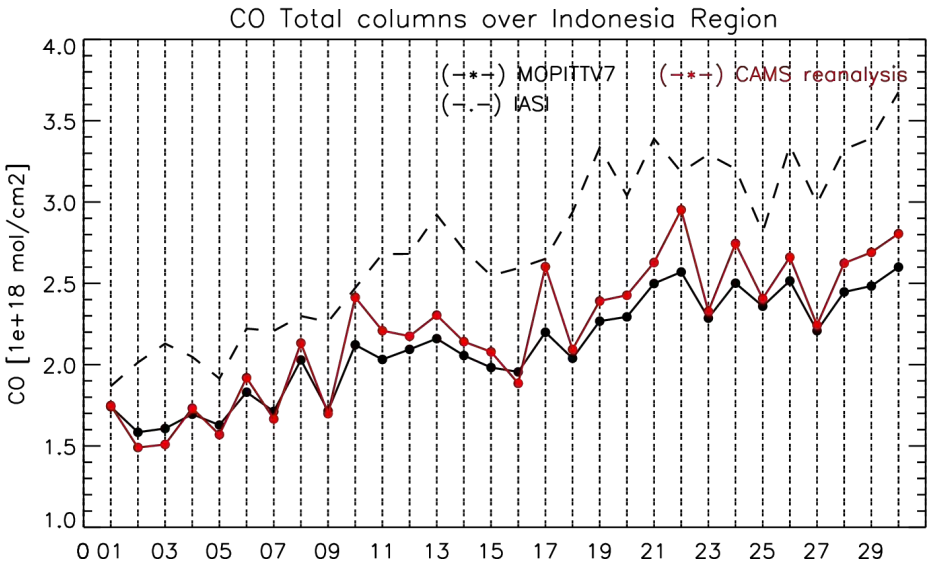


Figure 2.13.1: CO total column from satellite observations MOPITT V7 and IASI (black) and model simulations: reanalysis (red) and control run data (dark blue), over Indonesia (70E-150E and 11S-6N) during September 2015.

## 2.13 Fire events in Indonesia in autumn 2015

*Taken from the 2003-2016 CAMS-global reanalysis report [rea2018].*

The year 2015 was marked by a strong El Nino event which intensified the dry season over large parts of Indonesia. During September and October 2015, the largest amount of fire emissions were recorded in Indonesia since 1997, based on GFAS and GFED emissions time series. Daily CO total columns from the CAMS-global reanalysis over a region covering Indonesia (70E-150E and 11S-6N) for September 2015 were compared to IASI and MOPITT data. Observations show an area-average increase of CO total column from ~ $1.8 \times 10^{18}$ molec/cm$^2$ in the beginning of September to ~ $2.6 \times 10^{18}$ molec/cm$^2$ in MOPITT and $3.7 \times 10^{18}$ molec/cm$^2$ in IASI by the end of September, indicating IASI data up to 40 % higher compared to MOPITT (Fig. 2.13.1). Evaluation of model results shows that the reanalysis CO total columns are in good agreement with the MOPITT observations with a positive bias less than 15 %.

## 2.14 Alaskan fires in June 2015

*Taken from the JJA-2015 NRT validation report [nrt2015a].*

Several fires started on the 20th of June 2015 in Alaska. An analysis of IASI CO total column shows a strong plume of CO in this region and eastward transport inland of the continent by 26 of June. Both model simulations, o-suite and control run, captured both the location of the plume and inland transport of CO. Another fire event took place in Western Canada (~ 55°N, 115°W) and started on 28 of June. This can be seen in IASI CO total column data. Atmospheric transport of CO towards north-east and south-east from these fires is clearly seen in the satellite data in the end of June, Figure 2.14.1. Both model runs captured the location of the West Canadian fire and south-eastern plume of CO. Modelled CO values in transatlantic transportation pathway towards Europe are weaker compared to IASI data, but o-suite results show slightly better agreement with satellite data over the North-Atlantic Ocean than the control run. Over the polar region, IASI observations show high CO values on 28 and 29 of June, but both model runs show difficulties to capture this distribution patterns.

An IAGOS landing and departure from Chicaco captured a plume with elevated CO and $O_3$ on 28 June, Figure 2.14.2. This comparison shows the improved performance of the o-suite compared to control to capture the plume, although the $O_3$ enhancement appears over-estimated.

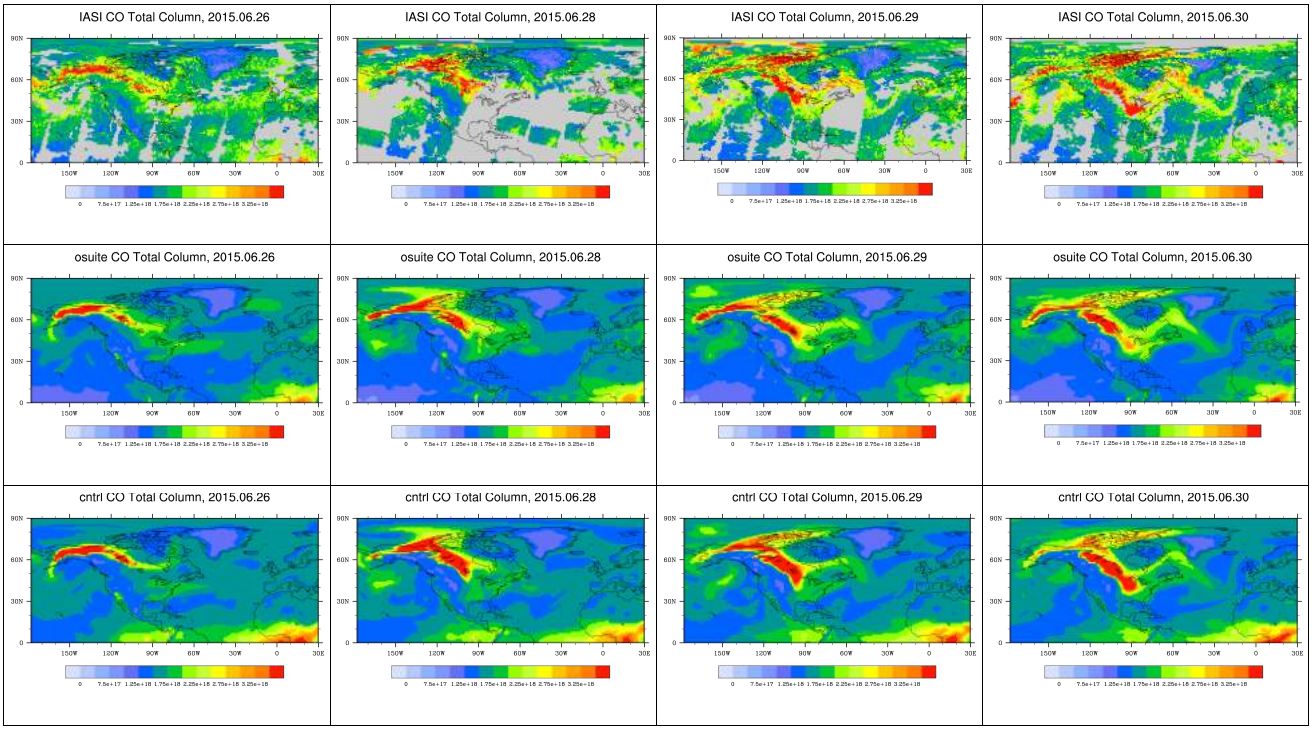


Fig. 2.14.1: CO total columns on 26, 28, 29 and 30 of June 2015 from IASI (top-left), o-suite (top-right) and control run (bottom) over the selected region.

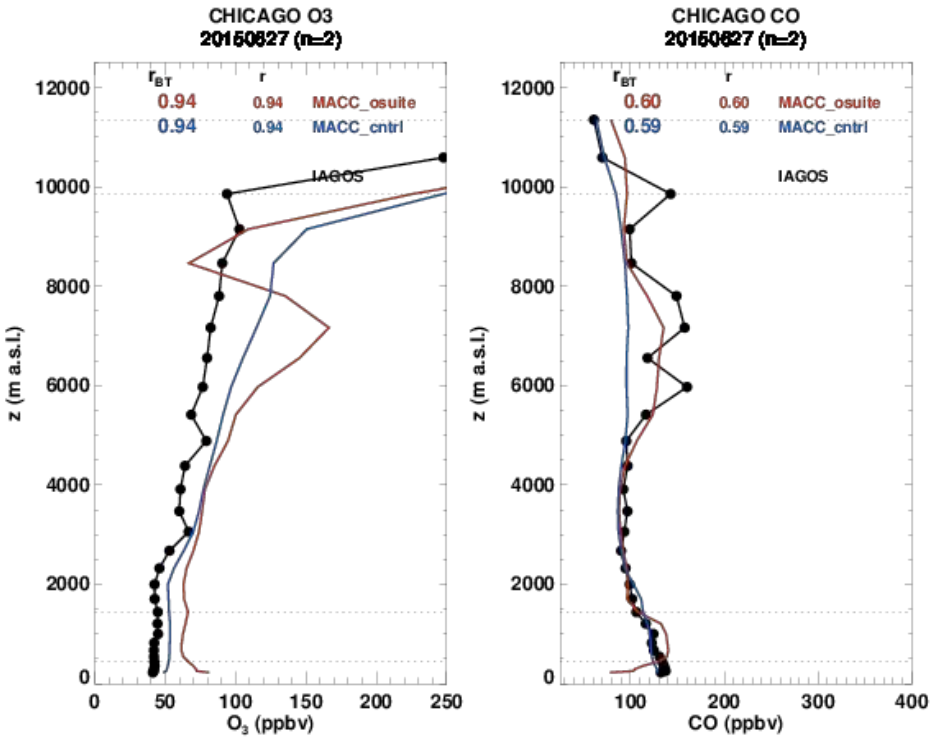


Figure 2.14.2: Evaluation of CO and $O_3$ profile from IAGOS (black) and the two NRT runs over Chicago for 27 June 2015.

## 2.15 Fires in Siberia, July 2012

*Taken from the 2003-2016 CAMS-global reanalysis report [rea2018].*

Summer 2012 was characterized by a large number of fire events in Siberia and high amount of fire emissions transported across Pacific Ocean towards the west coast of North America. Satellite observations show clear increases of CO emissions over the Siberian region during July 2012 (Fig. 2.15.1). IASI data are generally higher compared to MOPITT by about 15%. The CAMS-global reanalysis run reproduces the enhanced CO values, and shows a good agreement with the MOPITT observations with difference of less than 10 %.

The geographical distribution of IASI CO data indicates large emission plumes transported from active fire regions towards the west coast of North America over the Pacific Ocean (Fig. 2.15.2.). The reanalysis run captures the location of the plume and trans-Pacific transport of CO emissions. The reanalysis overestimates CO total columns over the fire regions. In the transport pathway over the ocean, the reanalysis data show an underestimation of the CO plume.

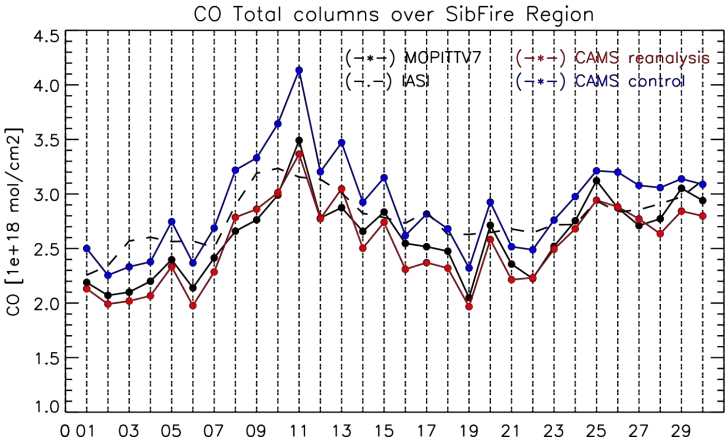


Figure 2.15.1: CO total column from satellite retrievals MOPITT V7 and IASI (black) and reanalysis (red) and control run data (blue) over Siberian region during July 2012.

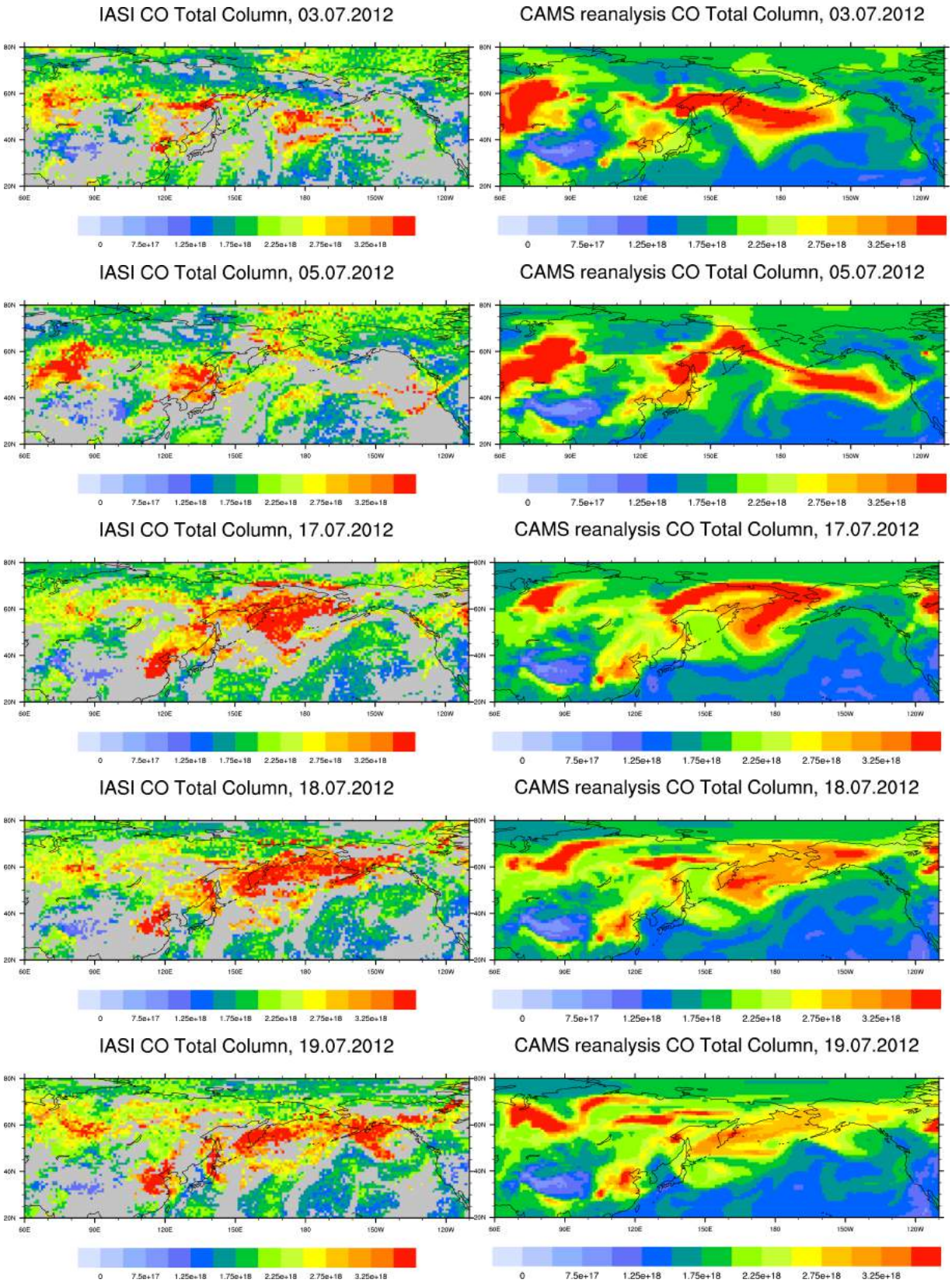


Figure 2.15.2.: CO total column over Siberian region for 03, 05, 17, 18 and 19 July 2012 from IASI (left), and the reanalysis (right).

# 3 Dust storms

## 3.1 Dust over the Arabian and Iberian Peninsulas: late April 2018

*Taken from the March-May 2018 NRT validation report [nrt2018a].*

A dense wall of dust pushed across the Arabian Peninsula in late April 2018. The intensified north-westerly wind caused dust to rise from the Iraq Desert area and move in a south-easterly direction affecting Iraq, Kuwait, Bahrain, Qatar, Kingdom of Saudi Arabia, United Arab Emirates (UAE), and to reach Yemen over the next days achieving an aerosol optical depth (AOD) of up to 7.3 and reducing drastically the visibility to less than 300 m in sites in the Persian Gulf.

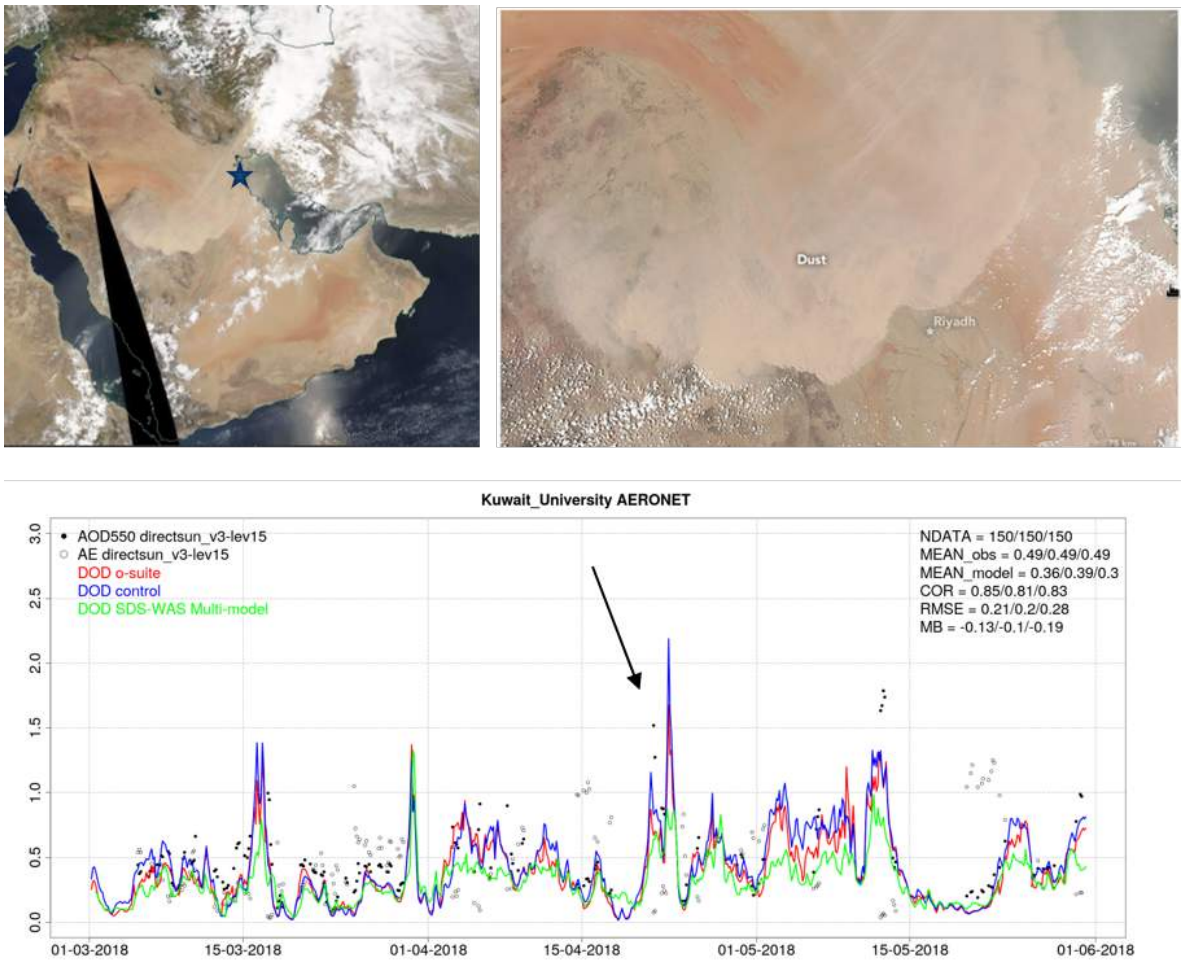


Figure 3.1.1: Upper panels. NASA MODIS/Aqua (right) and Suomi NPP-VIIRS (left) image on 23rd April 2018. LANCE/EOSDIS Rapid Response. Lower panel: Model vs AERONET observations over Kuwait University (its location is indicated in the MODIS/Aqua image). AOD from AERONET (black dot), AOD o-suite (red line), AOD control (blue line), AOD-Nat o-suite (orange line), AOD-Nat control (cyan line). Skill scores per each individual site and model (o-suite/control/SDS-WAS Multi-model) are shown in the upper right corner (NDATA: available 3-hourly values used for the calculations, MEAN observations, MEAN_model, COR, RMSE, MB).

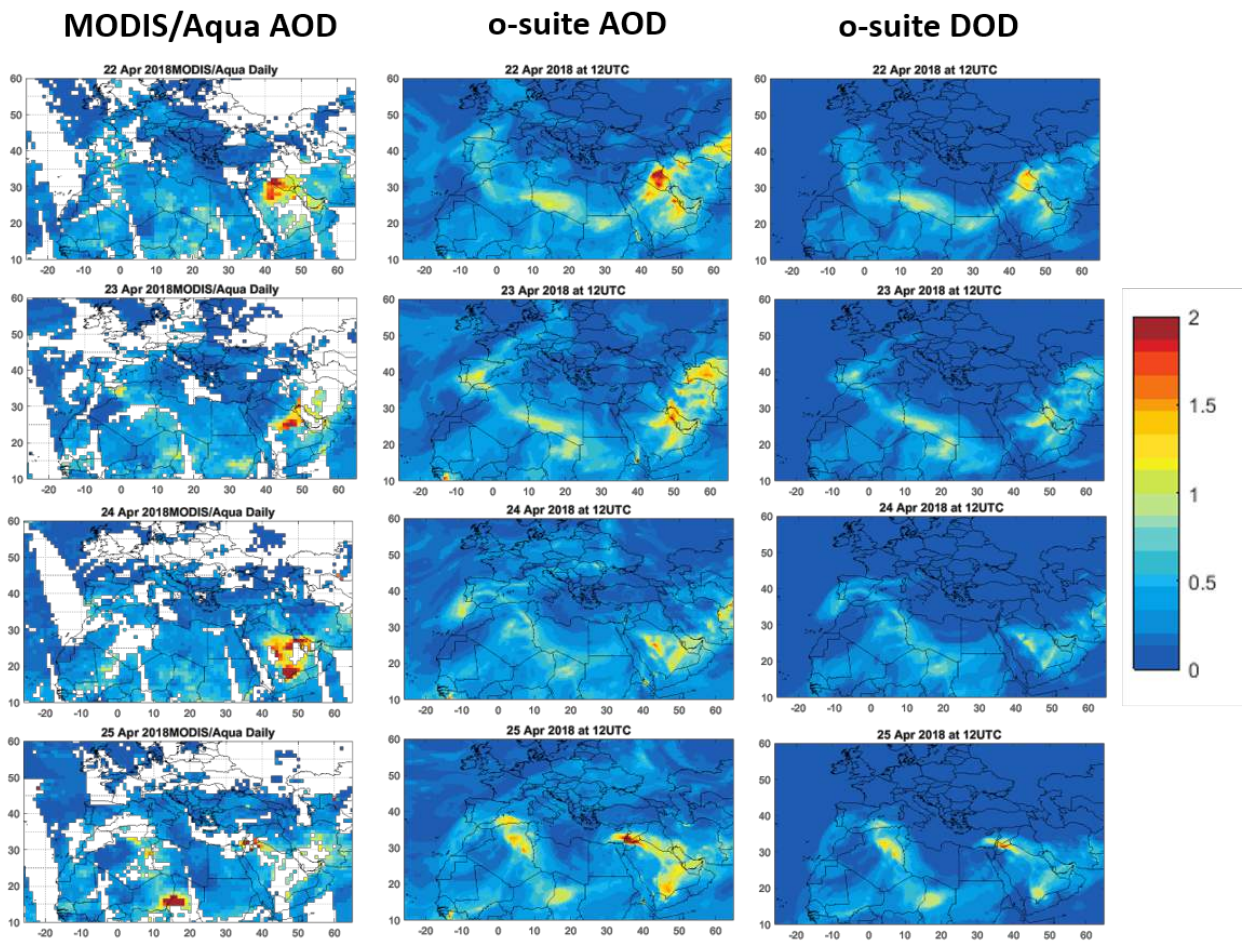


Figure 3.1.2. AOD and DOD at 12UTC from o-suite (central and right column) and AOD from MODIS-Aqua combined Dark Target and Deep Blue aerosol products (left column), from April 22 to April 25, 2018. MODIS-Aqua overpasses are around 12UTC over the study period.

A massive dust storm lashed Riyadh city and its suburbs in the late afternoon on 23rd April, rendering traffic disruptions due to low visibility on the roads as it was reported in different media channels. The large storm stretched roughly 500 km across the Arabian Peninsula. When the Visible Infrared Imaging Radiometer Suite (VIIRS) on Suomi NPP captured this image on April 23, 2018, dust had nearly reached Riyadh, Saudi Arabia's capital and most populous city (see Figure 3.1.1). Large sand storms in this region are often fuelled by strong north-westerly winds known as the Shamal.

The CAMS o-suite AOD can timely reproduce the spatial distribution of the dust plume over the Arabian Peninsula in comparison with AERONET over Kuwait University (see Figure 3.1.1 bottom panel) and MODIS/Aqua (see Figure 3.1.2) despite the fact that the model tends to underestimate the observed maximum values during the whole event. At surface levels, the CAMS systems are also able to reproduce the spatial evolution of the dust transport showing a correspondence with a reduction of the visibility (see Figure 3.1.3).

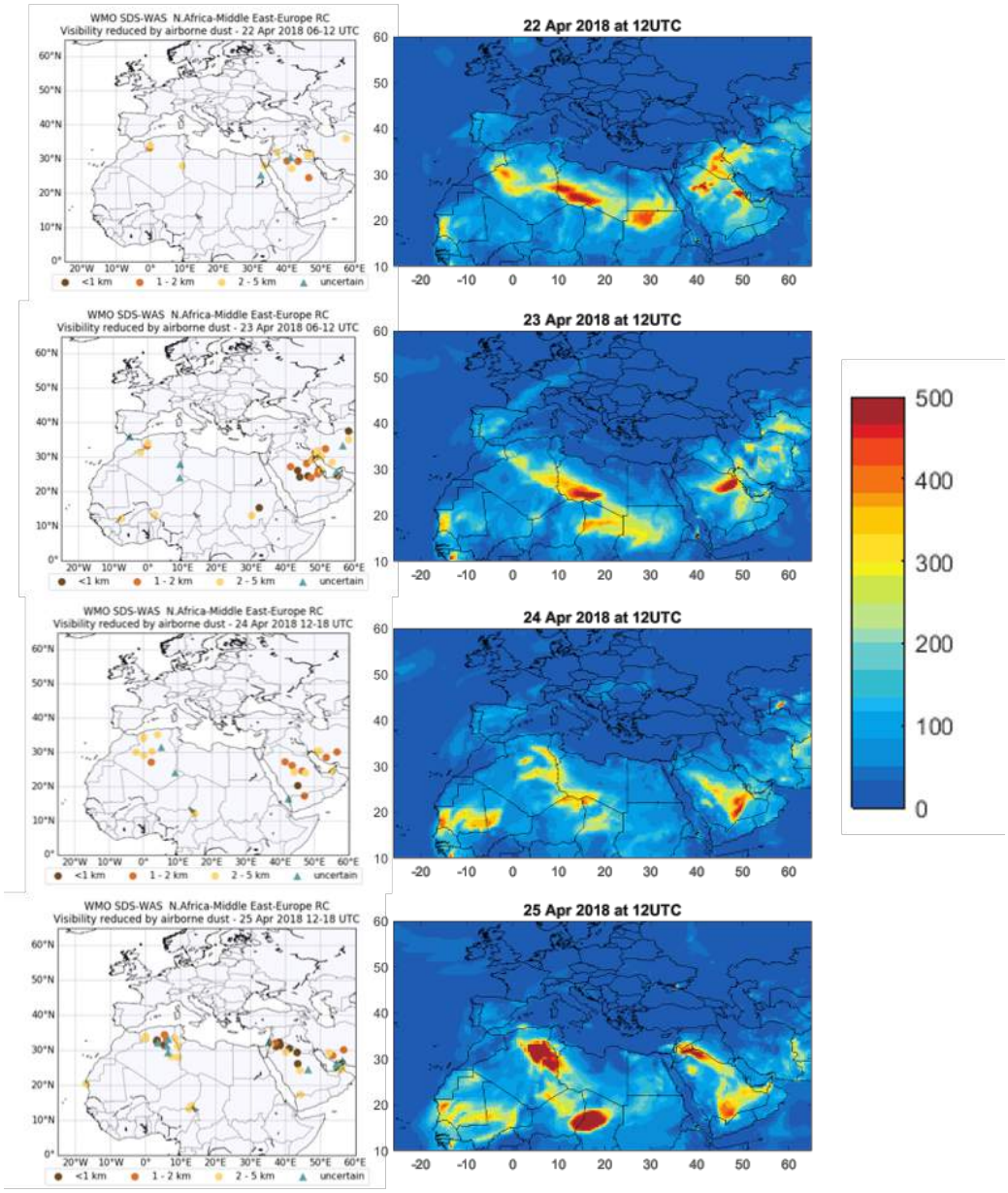


Figure 3.1.3. PM10 (in µg/m$^3$) at 12UTC from o-suite (right column) and visibility (in km) from METAR reports (left column), from April 22 to April 25, 2018.

During the same period, some hot spots of dust were observed in Libya (on 22-23 April) and Algeria (on 25$^{th}$ April). These events affected the Iberian Peninsula giving one week of high AOD (up to 1.2 in Madrid, Figure 3.1.4) and PM10/PM2.5 (up to 60 µg/m$^3$ in Villar Arzobispo and Zorita in Figure 7.4.5). The comparison with the visibility observations (Figure 3.1.3) also shows a reduction of the visibility associated to the dust from 22 to 25 April indicating the ability of the CAMS model to predict the extension and timing of the event. This intrusion over the Iberian Peninsula is well predicted by the CAMS model although it overestimates its magnitude as it is shown in comparison with AERONET and EIONET observations.

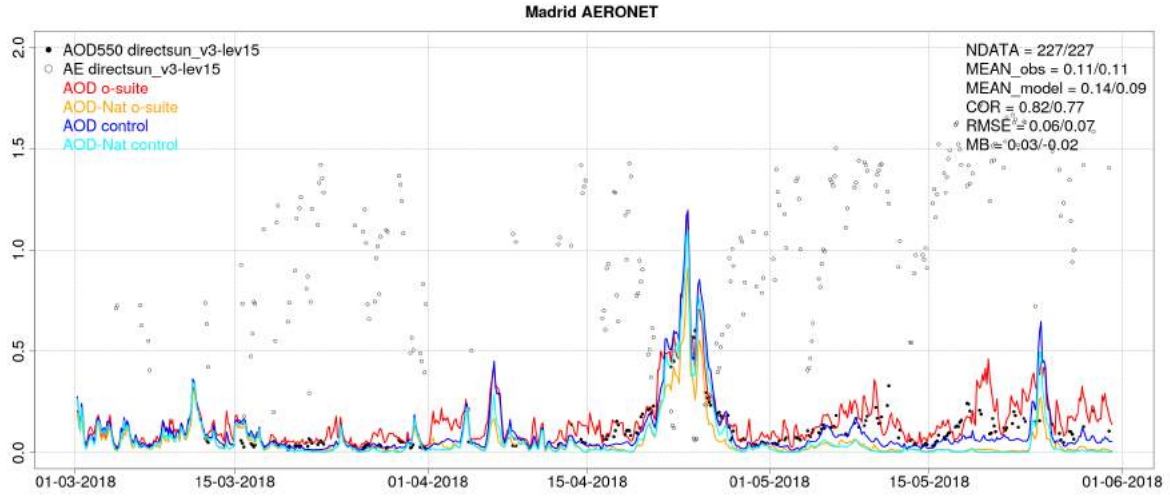


Figure 3.1.4: AOD from AERONET (black dot), AOD o-suite (red line), AOD control (blue line), AOD-Nat o-suite (orange line), AOD-Nat control (cyan line), for the study period over Madrid (Central Spain). AOD-Nat corresponds to the natural aerosol optical depth that includes dust and sea-salt. Skill scores per each individual site and model (o—suite/control) are shown in the upper right corner (NDATA: available 3-hourly values used for the calculations, MEAN observations, MEAN_model, COR, RMSE, MB).

Higher dust concentrations predicted by the CAMS model over this spring season are linked to an increase of the magnitude of the predicted gusts winds that consequently causes an enhancement of the dust emissions over desert dust source regions. Consequently, the transported dust to long-range regions as Europe is increased during this season.

## 3.2 Dust over the Mediterranean: 31 January 2018 – 10 February 2018

*Taken from the DJF 2018 NRT validation report [nrt2018b].*

During the end of January and early February, there was an intense dust activity over the Mediterranean. On 30$^{th}$ January an intense dust outbreak with origin in Algeria affected Southern Iberian Peninsula and Western Mediterranean (see Granada in Figure 3.2.1 and Figure 3.2.2). On 2$^{nd}$ February, a new dust event with origin in Algeria-Tunisia border was affecting Central-Eastern Mediterranean (see Rome Tor Vergata and Athens-NOA in Figure 3.2.1 and Figure 3.2.2) achieving high aerosol concentrations (up to 1.3 in Greece see Athens-NOA on 4$^{th}$ February in Figure 3.2.1). After this later event, the Eastern Mediterranean was again affected by two more consecutive dust event with origin in Libya (see Athens-NOA in Figure 3.2.1 and Figure 3.2.3). This exceptional "dusty" period over the Mediterranean was associated with a strong and permanent pressure high system in the North Atlantic (not shown here) that was inducing African flow towards the Mediterranean.

CAMS AOD o-suite can timely reproduce the spatial distribution of the different dust plumes over the Mediterranean in comparison with AERONET (Figure 3.2.1) and MODIS/Aqua (Figure 3.2.2, Figure 3.2.3). However, a high AOD/DOD ratio is observed over the dust affected areas inducing DOD underestimations, particularly, this ratio is very high during 2-4 February event over Central Mediterranean (see Figure 3.2.3). Non-natural aerosols (mainly organic matter and sulphates) are contributing the main aerosol contributing to the total AOD during the days of the dust event.

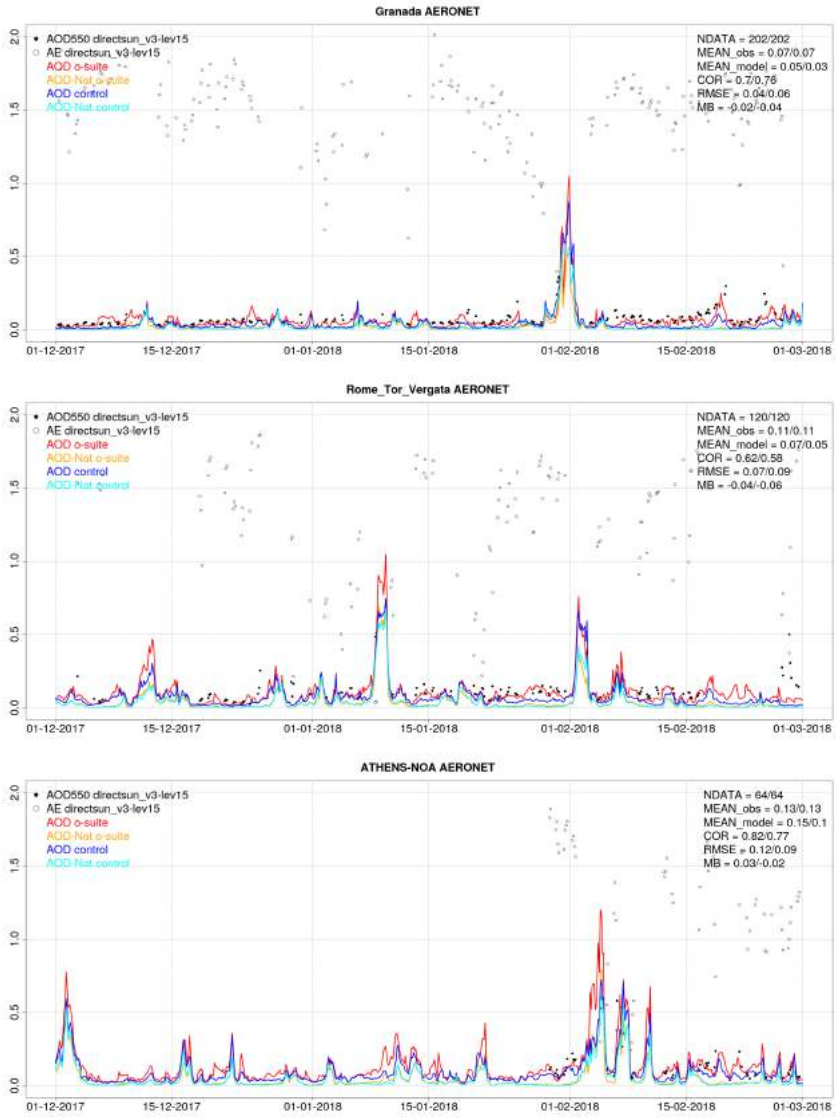


Figure 3.2.1: AOD from AERONET (black dot), AOD o-suite (red line), AOD control (blue line), AOD-Nat o-suite (orange line), AOD-Nat control (cyan line), for the study period over Granada (Spain), Rome Tor Vergata (Italy) and Athens-NOA (Greece). AOD-Nat corresponds to the natural aerosol optical depth that includes dust and sea-salt. Skill scores per each individual site and model (o—suite/control) are shown in the upper right corner (NDATA: available 3-hourly values used for the calculations, MEAN observations, MEAN_model, COR, RMSE, MB).

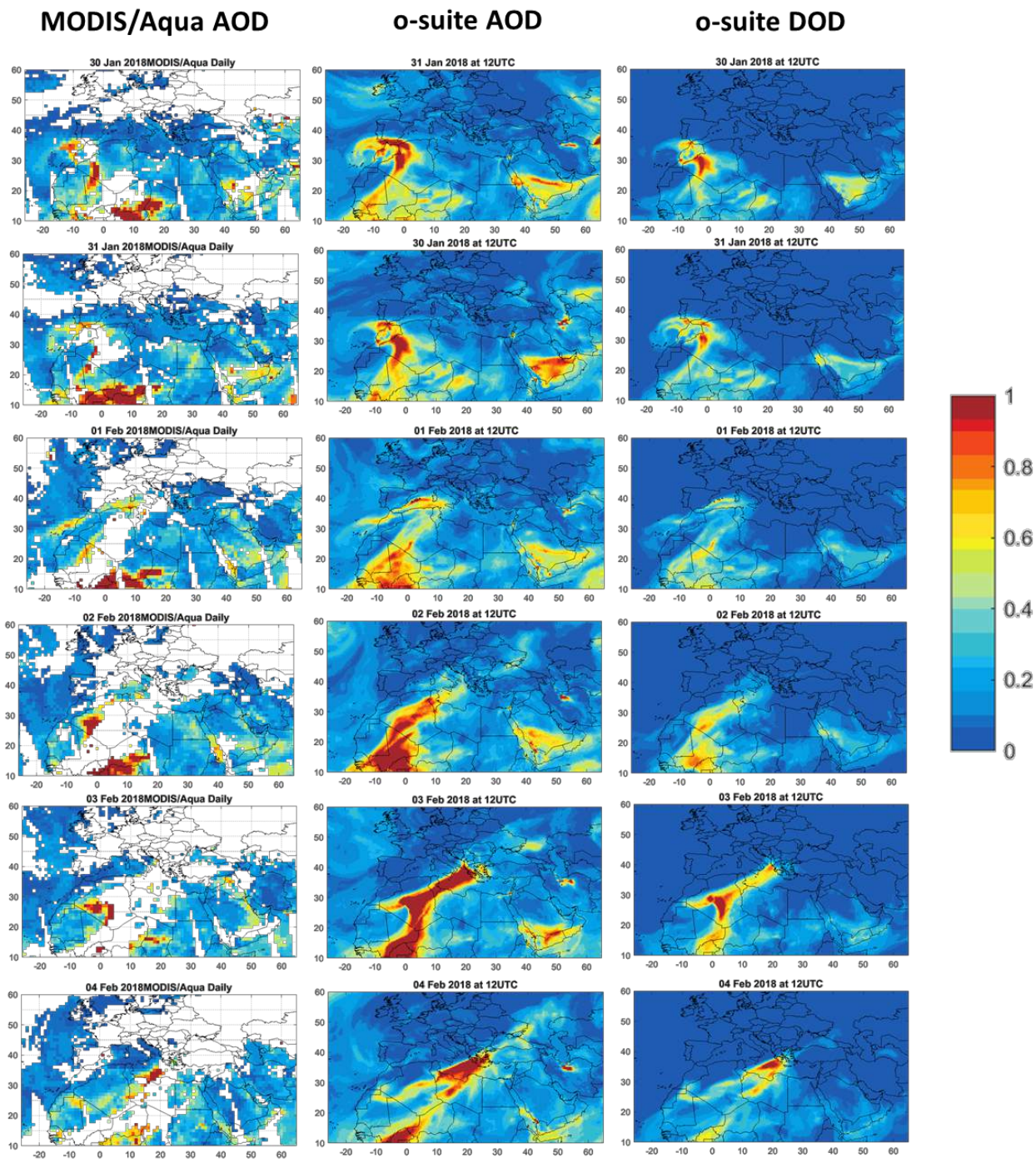


Figure 3.2.2. AOD and DOD at 12UTC from o-suite (central and right column) and AOD from MODIS-Aqua combined Dark Target and Deep Blue aerosol products (left column), from January 30 to February 4, 2018. MODIS-Aqua overpasses are around 12UTC over the study period.

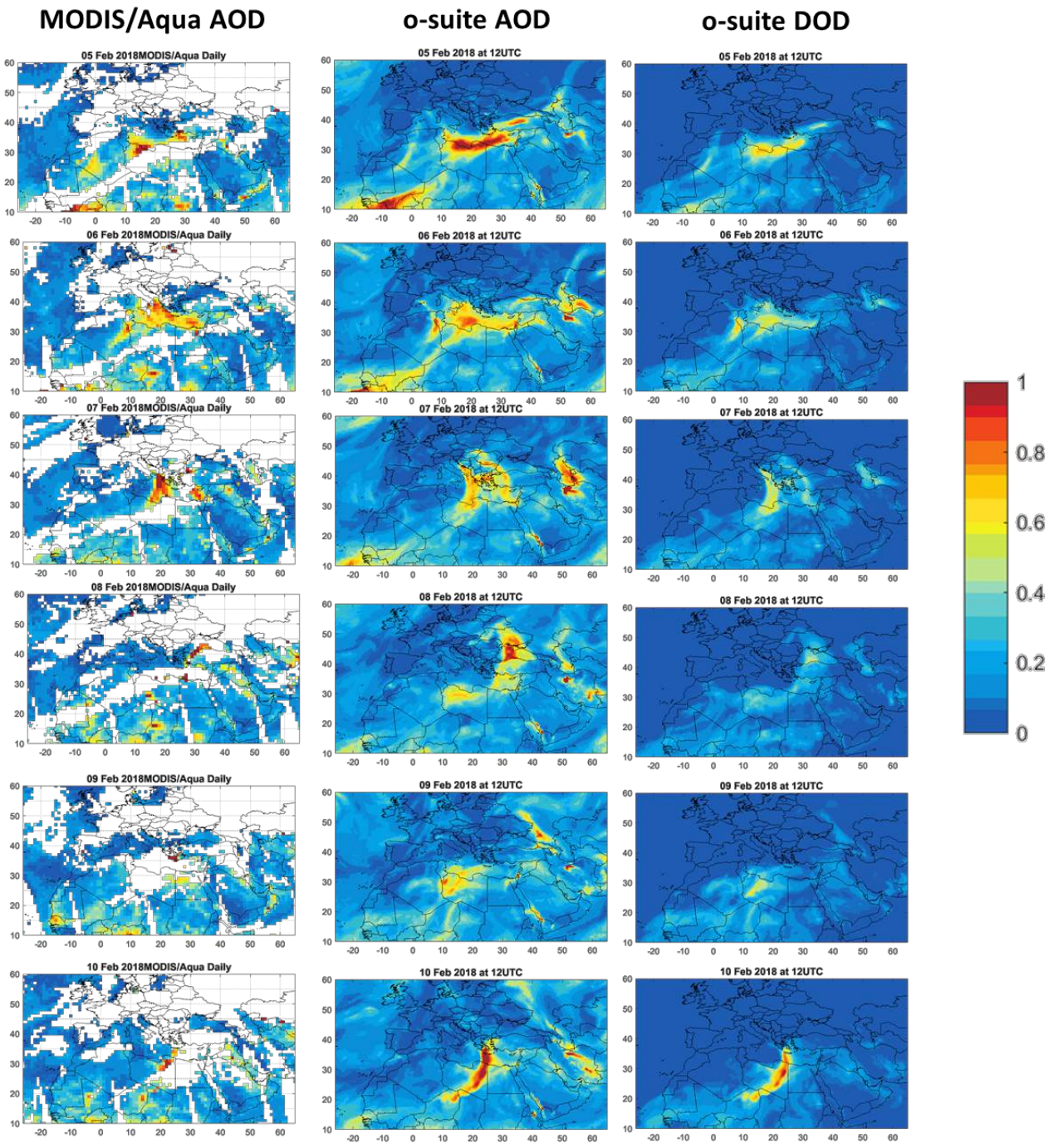


Figure 3.2.3. AOD and DOD at 12UTC from o-suite (central and right column) and AOD from MODIS-Aqua combined Dark Target and Deep Blue aerosol products (left column), for February 5-10, 2018. MODIS-Aqua overpasses are around 12UTC over the study period.

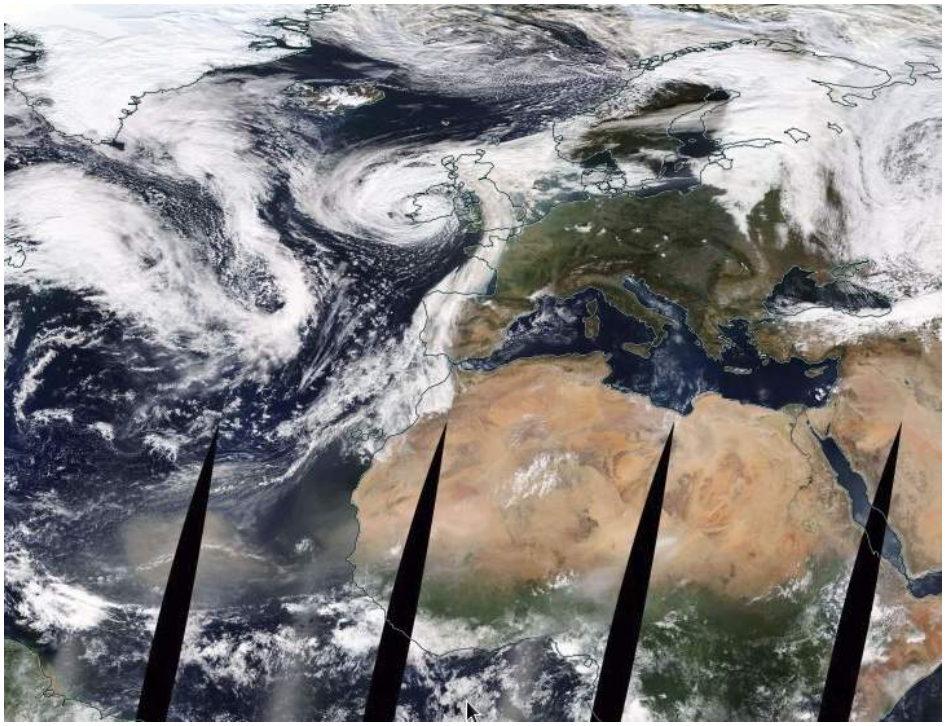

Figure 3.3.1. Daily composite image of MODIS-Aqua for 16th October. Satellite imagery shows high concentrations of airborne Saharan dust over the North Atlantic and a deep low centered over UK.

## 3.3 Dust over the North Atlantic: 13-16 October 2017

*Taken from the SON-2017 NRT validation report [nrt2018c].*

In mid-October 2017, a number of planes were forced to make emergency landings at Heathrow Airport as Storm Ophelia pulled a high concentration of aerosols into the London sky on 16th October. Five planes have reportedly made full emergency landings at the airport amid claims of the smell of smoke filling the cockpit. The rare spectacle was caused by Storm Ophelia pushing warm air (and dusty) from Africa northwards (see Figure 3.3.1). As the air moved north towards Ireland and the UK, it gathered smoke and tiny debris from recent wildfires in Spain and Portugal.

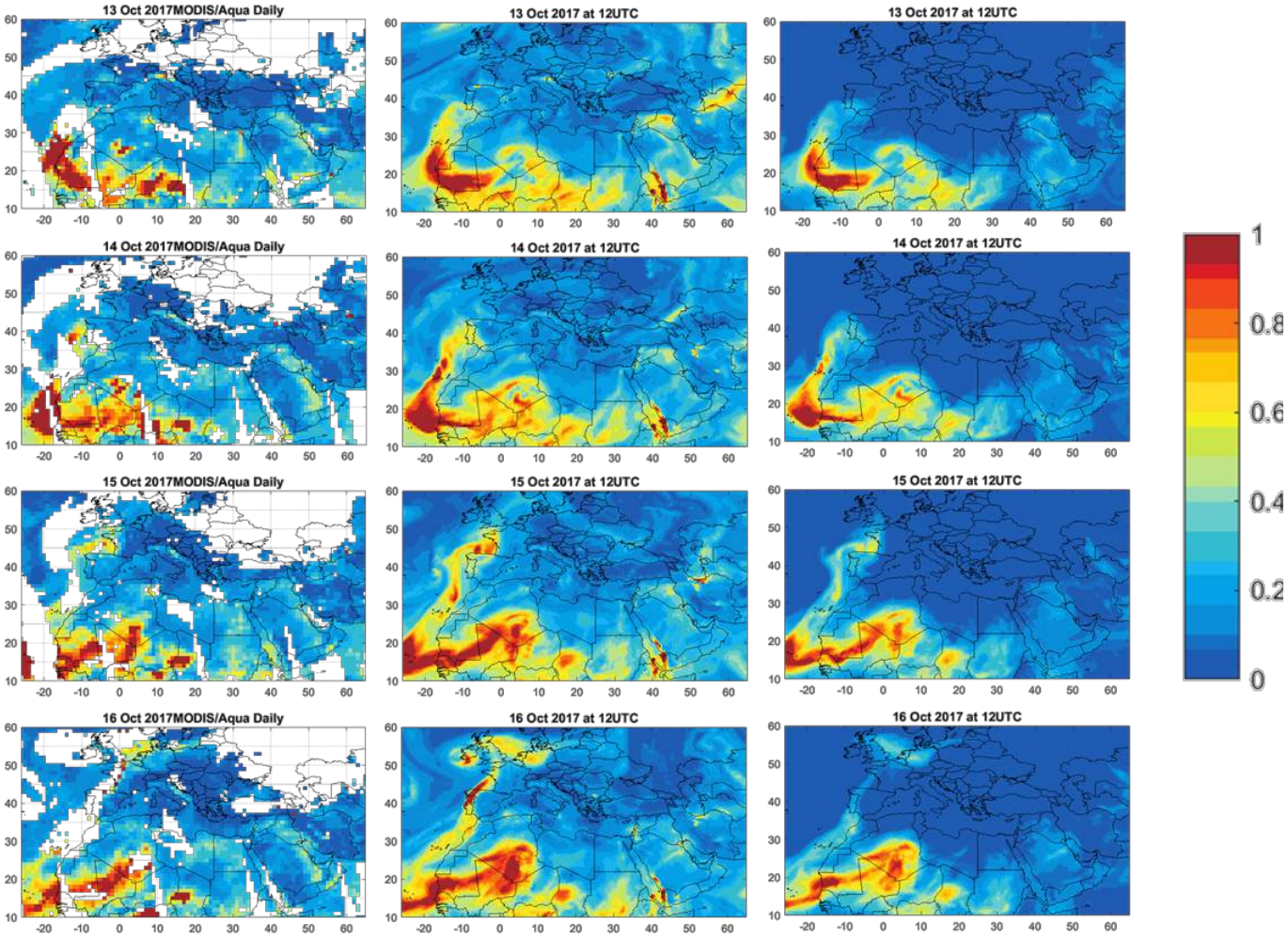


Figure 3.3.2. AOD and DOD at 12UTC from o-suite (central and right column) and AOD from MODIS-Aqua combined Dark Target and Deep Blue aerosol products (left column), for October 12-16, 2017. MODIS-Aqua overpasses are around 12UTC over the study period.

The CAMS o-suite did timely reproduce the spatial distribution of the different dust plumes over the North Atlantic on 12-16 October which affected northwestern Spain on 15 October and the United Kingdom on 16 October as observed by MODIS (Figure 3.3.2). The whole episode is well simulated by CAMS o-suite in the North Atlantic and Europe. We can see how CAMS o-suite tracks fairly well the changes in both shape and size of the dust layer throughout the dusty period and how the AOD levels are enhanced on 15 October in northwestern Spain coinciding with the location of the fires. The magnitude of the event is overestimated by the model as shown the comparison with AERONET observations. Particularly in Coruna (Spain, see Figure 3.3.3), the control experiment predicts an unrealistic AOD peak above 3 that o-suite reduces to up 1.5.

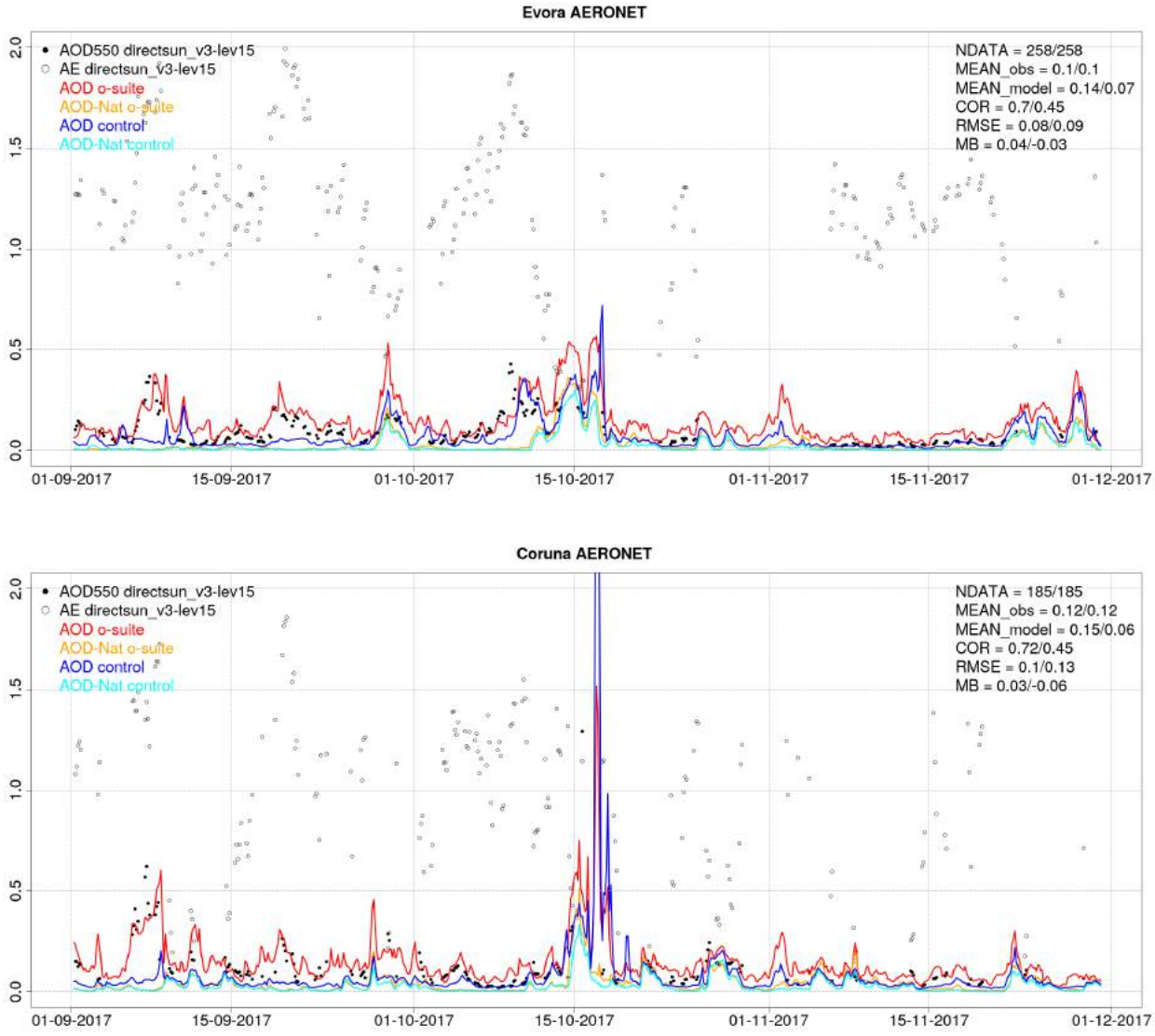


Figure 3.3.3: AOD from AERONET (black dot), AOD o-suite (red line), AOD control (blue line), AOD-Nat o-suite (orange line), AOD-Nat control (cyan line), for the study period over Evora (Portugal) and Coruna (Spain). AOD-Nat corresponds to the natural aerosol optical depth that includes dust and sea-salt. Skill scores per each individual site and model (o-suite/control) are shown in the upper right corner (NDATA: available 3-hourly values used for the calculations, MEAN observations, MEAN_model, COR, RMSE, MB).

## 3.4 Dusty June over the North Atlantic: 25-27 June 2017

*Taken from the JJA-2017 NRT validation report [nrt2017a].*

In late-June 2017, winds lofted thick plumes of dust from northern Africa's deserts high into the air. On June 23, 2017, the Moderate Resolution Imaging Spectroradiometer (MODIS) on NASA's Aqua satellite (see Figure 3.4.1) captured this natural-colour image of a dust plume blowing over the Atlantic Ocean with origin Mauritania-Morocco border on 22$^{nd}$ June. A few days later, winds had

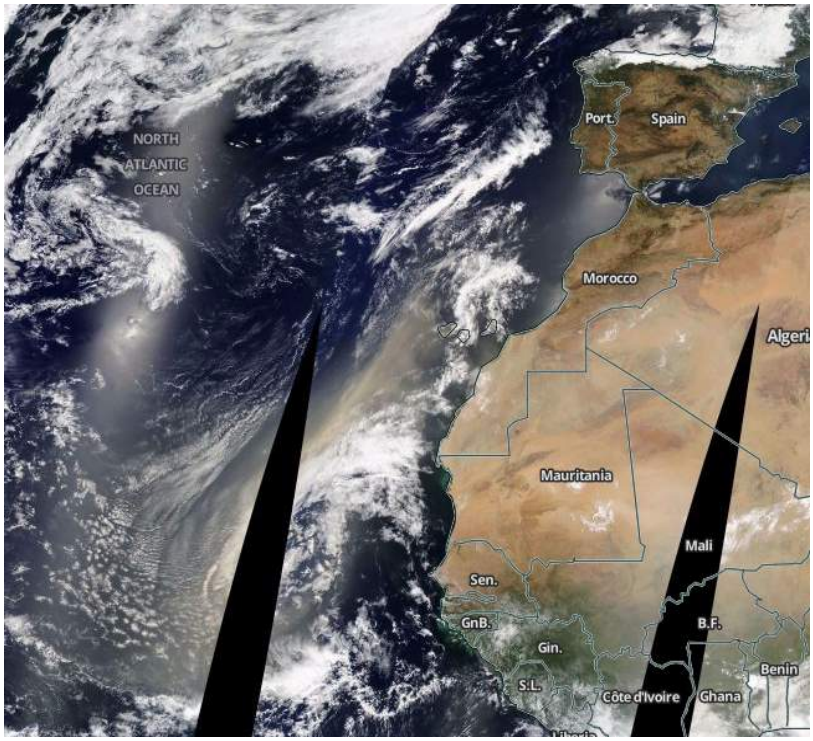


Figure 3.4.1. Daily composite image of MODIS-Aqua for 23rd June. Satellite imagery shows high concentrations of airborne Saharan dust over the North Atlantic.

already swept a plume of dust westward over the Atlantic Ocean reaching the archipelago of Cabo Verde (Cape Verde) and the Canary Islands by June 23 (see Figure 3.4.1). Dust was transported to higher latitudes reaching the Iberian Peninsula from June 24 and Corsica on June 28.

The CAMS o-suite did reproduce the spatial distribution of the different dust plumes over the North Atlantic on 22-24 June and Europe on 24-28 June as observed by MODIS (Fig. 3.4.2). We can see how CAMS o-suite tracks fairly well the changes in both shape and size of the dust layer throughout the dusty period. The whole episode is well simulated by CAMS o-suite and CAMS control in the North Atlantic and Europe. However, the magnitude of the event is underestimated by the model. Better results are obtained from the modelled AOD fields (Fig. 3.4.2). This indicates that the contribution to the total AOD of other non-dust species (in particular organic matter) is higher than expected over desert dust source and transport regions.

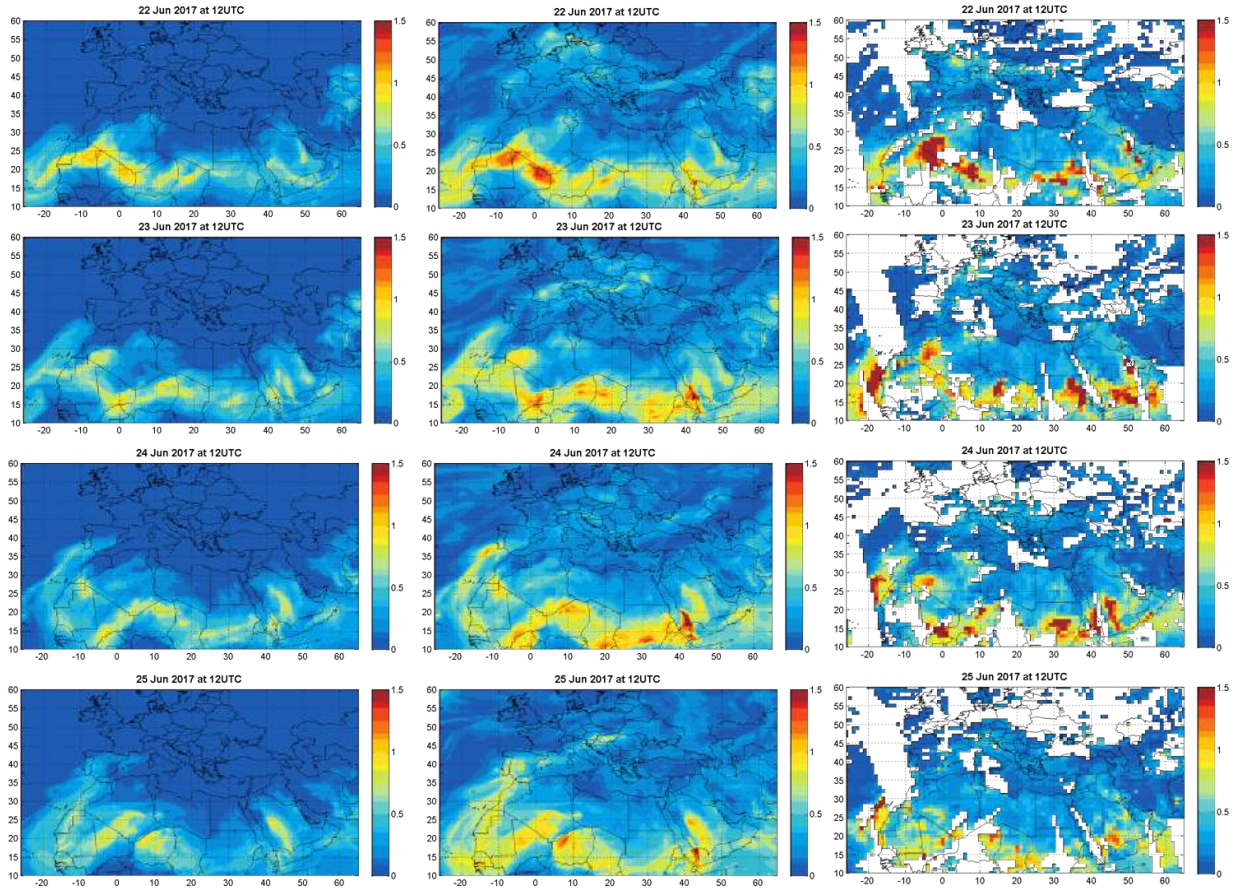


Figure 3.4.2. DOD (left) and AOD (middle) at 12UTC from o-suite and AOD from MODIS-Aqua combined Dark Target and Deep Blue aerosol products (right column), for June 22-25, 2017. MODIS-Aqua overpasses are around 12UTC.

The CAMS o-suite model captures the dust plume over the Iberian Peninsula and the Western Mediterranean although it overestimates the maximum PM10 peak in Iberian Peninsula (see Guadalix de la Sierra in central Iberian Peninsula in Figure 3.4.3) and Western Mediterranean sites (see Hospital Joan March and Venaco in Figure 3.4.3) at 24h forecasts. The dust concentration is decreasing for the longer forecasts (48 and 72h) achieving magnitudes closer to the observations. The predicted magnitude of the peak is strongly overestimated in Guadalix de la Sierra (from 24, 48 and 72h time leads) meanwhile in Hospital Joan March and Venaco is close to the observed peak (from 24, 48 and 72h time leads).

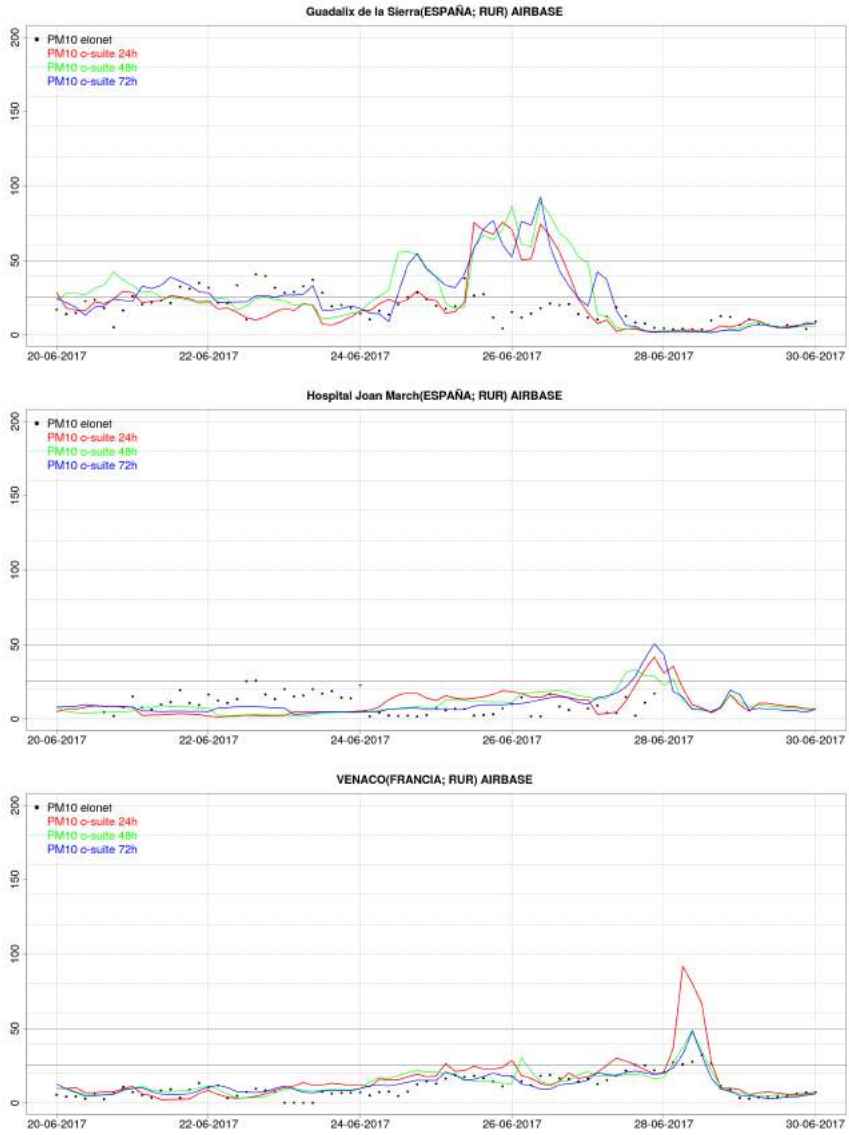


Figure 3.4.3. Observed PM10 from Airbase (black) and modelled PM10 from o-suite at 24h (red), 48h (green) and 72h (blue) time forecasts at Guadalix de la Sierra (Spain-Central Iberian Peninsula), Hospital Joan March (Spain-Balearic Islands) and Venaco (France-Corsica) from 20-30 June 2017.

## 3.5 Dust event over Tropical North Atlantic and Central Mediterranean: 9-12 May 2017

*Taken from the MAM-2017 NRT validation report [nrt2017b].*

A major Saharan dust event affected the Tropical North Atlantic and Central Mediterranean on 9-12 May 2017. Strong winds lofted a huge dust plume from western Africa and carried it toward the northeast into Europe and west toward Cabo Verde Islands. The event reaches far into Eastern Europe and over the Atlantic Ocean (see Figure 3.5.1).

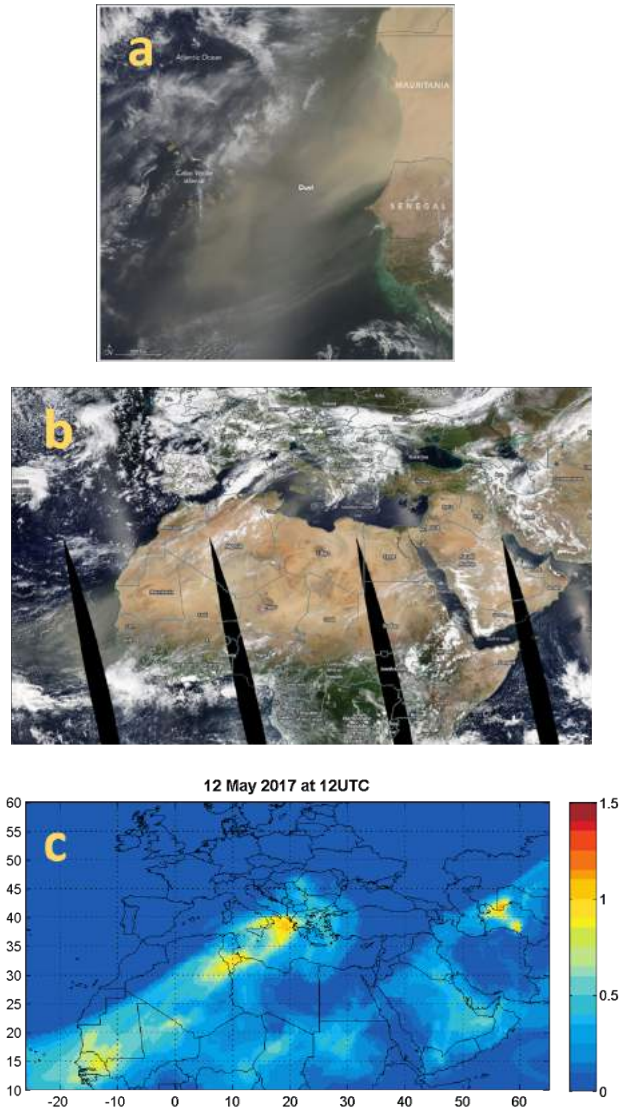


Figure 3.5.1. Strong desert winds in mid-May 2017 lofted a huge dust plume from western Africa and carried it over the Atlantic Ocean and the Mediterranean. The plume stretched southwest to the Cabo Verde (Cape Verde) islands and beyond the Mediterranean. The Moderate Resolution Imaging Spectroradiometer (MODIS) on NASA's Terra satellite acquired this natural-colour image of airborne sand and other aerosols a) at 12:10 Universal Time on May 9, 2017, and b) daily composite on 12th May. Source: NASA Earth Observatory. c) AOD dust forecast from CAMS o-suite for on12th May at 12UTC.

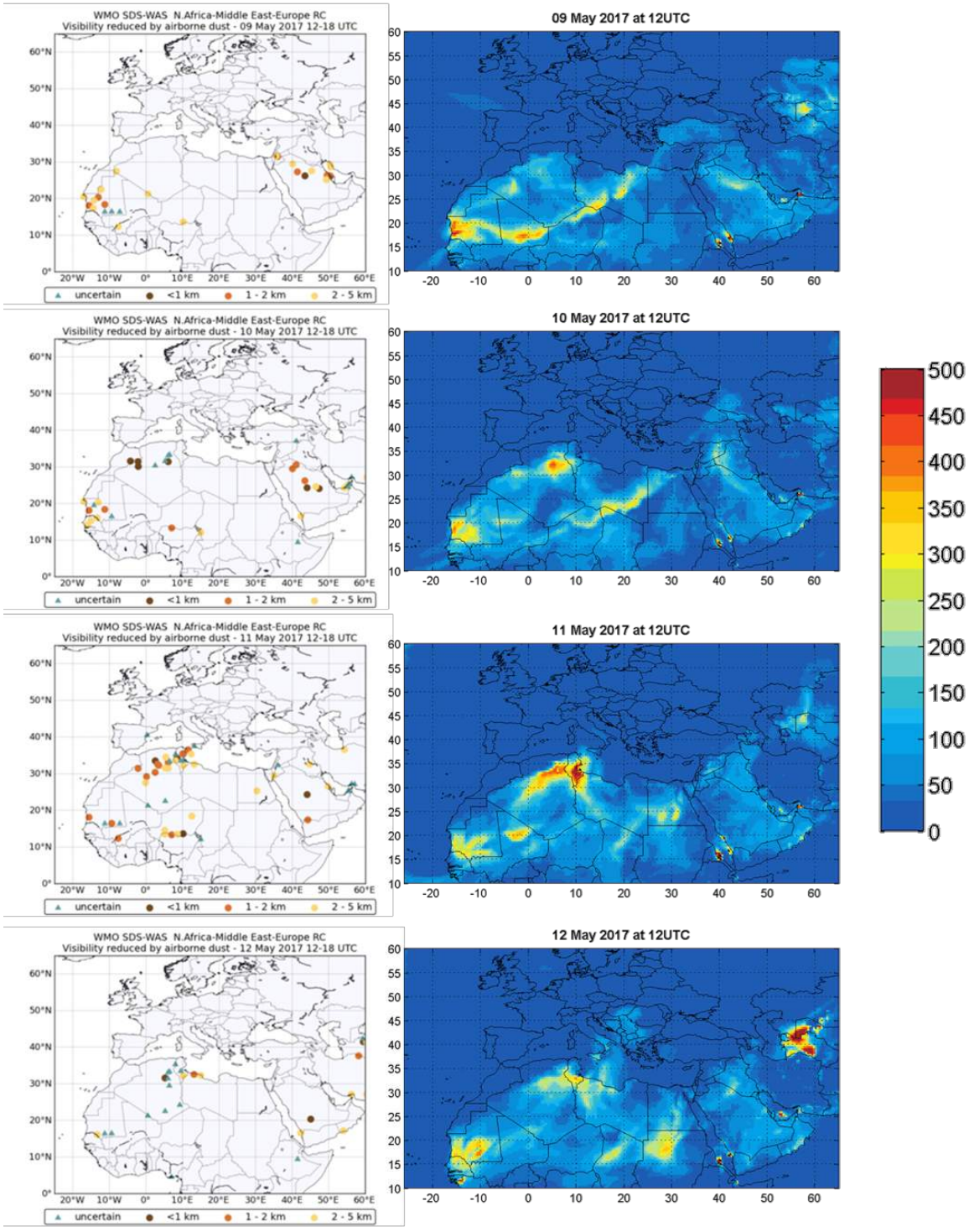


Figure 3.5.2. Visibility from METAR or SYNOP stations from SDS-WAS Regional Center (left column) and PM10 from o-suite during the case analysis from 9-12 May 2017. The maps show cases of visibility reduction by sand or dust to less than 5 km reported in METAR or SYNOP bulletins. More than 1,500 stations are checked every 6 hours. Brownish circles indicate stations where 'sand' or 'dust' has been explicitly reported. Triangles indicate stations where the present weather has been reported as 'haze', meaning that the visibility is reduced by particles of unspecified origin.

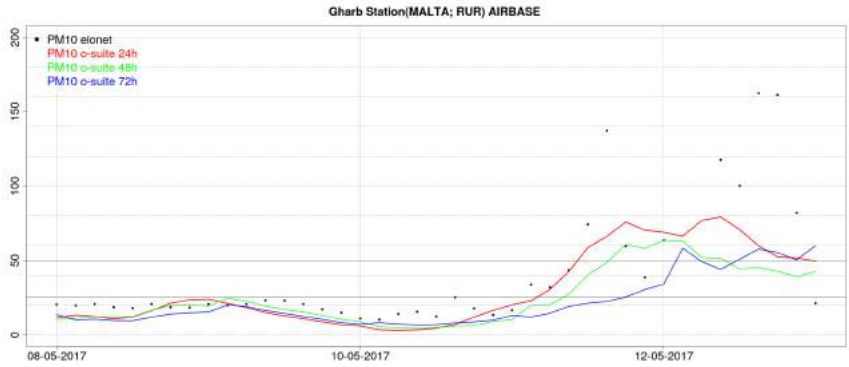


Figure 3.5.3. Observed PM10 from Airbase (black) and modelled PM10 from o-suite at 24h (red), 48h (green) and 72h (blue) time forecasts at Gharb (Malta) from 8-13 May 2017.

High loads of dust affected the entire southern Italy on 11th May, and the event continued the following days affecting Croatia, Bosnia and Herzegovina, Montenegro, Hungary and Serbia. At the same time, large amounts of dust are being pushed over the Atlantic Ocean toward Capo Verde, the Caribbean and South America. The full episode was observed by the AERONET sunphotometers, ground visibility (Figure 3.5.2) and air quality (Figure 3.5.3) stations.

An Atlantic dust outbreak took place on 8-13 May 2017, and from its origin in Mauritania it moved towards the West and in the following days crosses the Atlantic (see Figure 3.5.2). Satellite imagery (see Figure 3.5.1) shows high concentrations of airborne Saharan dust over Mauritania and Senegal (dust AOD up to 1.5). Over Europe, this dust outbreak caused an exceedance of the EU PM10 daily value detected achieving values of above 100 µg/m$^3$ in Malta (see Gharb station in Figure 3.5.3).

The CAMS o-suite model captured quite well the passage of the dust plumes as evidenced by the ground visibility observations (Figure 3.5.2), predicting concentration up to 100 µg/m$^3$ in Senegal and 50 µg/m$^3$ in Italy, Croatia, Bosnia and Herzegovina, Montenegro, Hungary and Serbia. The CAMS o-suite model captures the arrival of the dust plume over the Central Mediterranean site in Malta (see Gharb station in Figure 3.5.3) although it underestimates the maximum PM10 peak and the concentration is decreasing for the longer forecasts (24h, 48 and 72h).

## 3.6 Dust event over Iberian Peninsula and the Mediterranean: 20-27 February 2017

*Taken from the DJF-2017 NRT validation report [nrt2017c].*

Two consecutive dust plumes, that originated in Algeria, moved towards the Iberian Peninsula and the Mediterranean in late February 2017 (see Figure 3.6.1). The full episode was observed by the synoptic visibility (Figure 3.6.2) and air quality (Figure 3.6.3) observations.

The first dust outbreak took place on 20-23 February 2017. After being initiated in Algeria on 20th February it moved towards the east and then the next days crossed the Iberian Peninsula (see Figure 3.6.1, Figure 3.6.2 and Guadalix de la Sierra and Zorita Airbase stations in Figure 3.6.3). Satellite imagery (see Figure 3.6.1) showed high concentrations of airborne Saharan dust over the Alboran Sea, the southern half of the Iberian Peninsula and the Atlantic Ocean of the coast of Portugal on 21st February. The second dust outbreak also started in Algeria on 23rd February and moved west westwards crossing the entire Mediterranean Basin in the next days

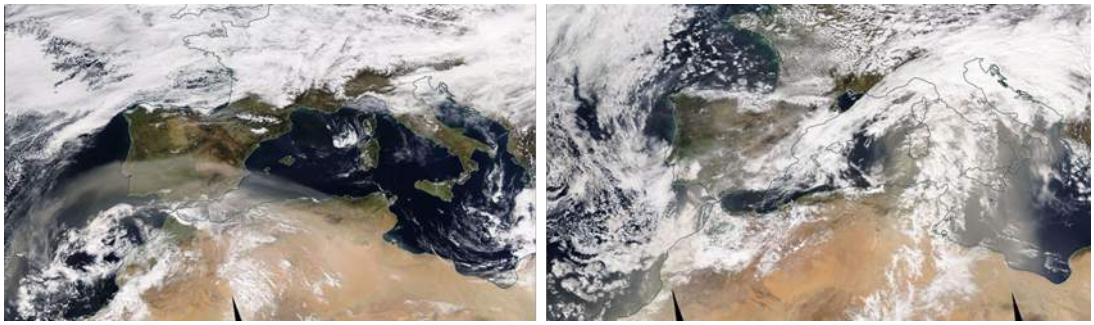

Figure 3.6.1. Daily composite image of MODIS-Aqua for 21st February (left) and MODIS-Terra for 24th February (right). Satellite imagery shows high concentrations of airborne Saharan dust over the Alboran sea, the southern half of the Iberian peninsula and the Atlantic ocean of the coast of Portugal on 21st February and a second dust plume affecting central Mediterranean on 24th February.

(see Figure 3.6.1 and Venaco and Gharb Airbase stations in Figure 3.6.3), reaching Cyprus on 27th February 2017. Over Europe, these dust outbreaks caused an exceedance of the EU PM10 daily value detected achieving values of above 200 μg/m$^3$ in Spain and Italy. The CAMS o-suite model captured quite well the passage of the dust plumes over the ground visibility (Figure 3.6.2) predicting concentration up to 300 μg/m$^3$ in Spain and Italy.

For the first dust event, the CAMS o-suite model captures the arrival of the dust plume over the Spanish sites although it overestimated the maximum PM10 peak in Iberian Peninsula and Western Mediterranean sites at 24h forecasts, the concentration is decreasing for the next time leads (48 and 72h) achieving magnitudes closer to the observations. In the second dust event, the model can predict the arrival of the second dust plume on 24th February over Corsica (see Venaco in Figure 3.6.3) as well as in Malta (see Gharb station in Figure 3.6.3) on 25th February. The predicted magnitude of the peak is strongly overestimated in Corsica (for 24, 48 and 72 leads), but meanwhile in Malta it is close to the observed enhancement (from 24, 48 and 72h time leads).

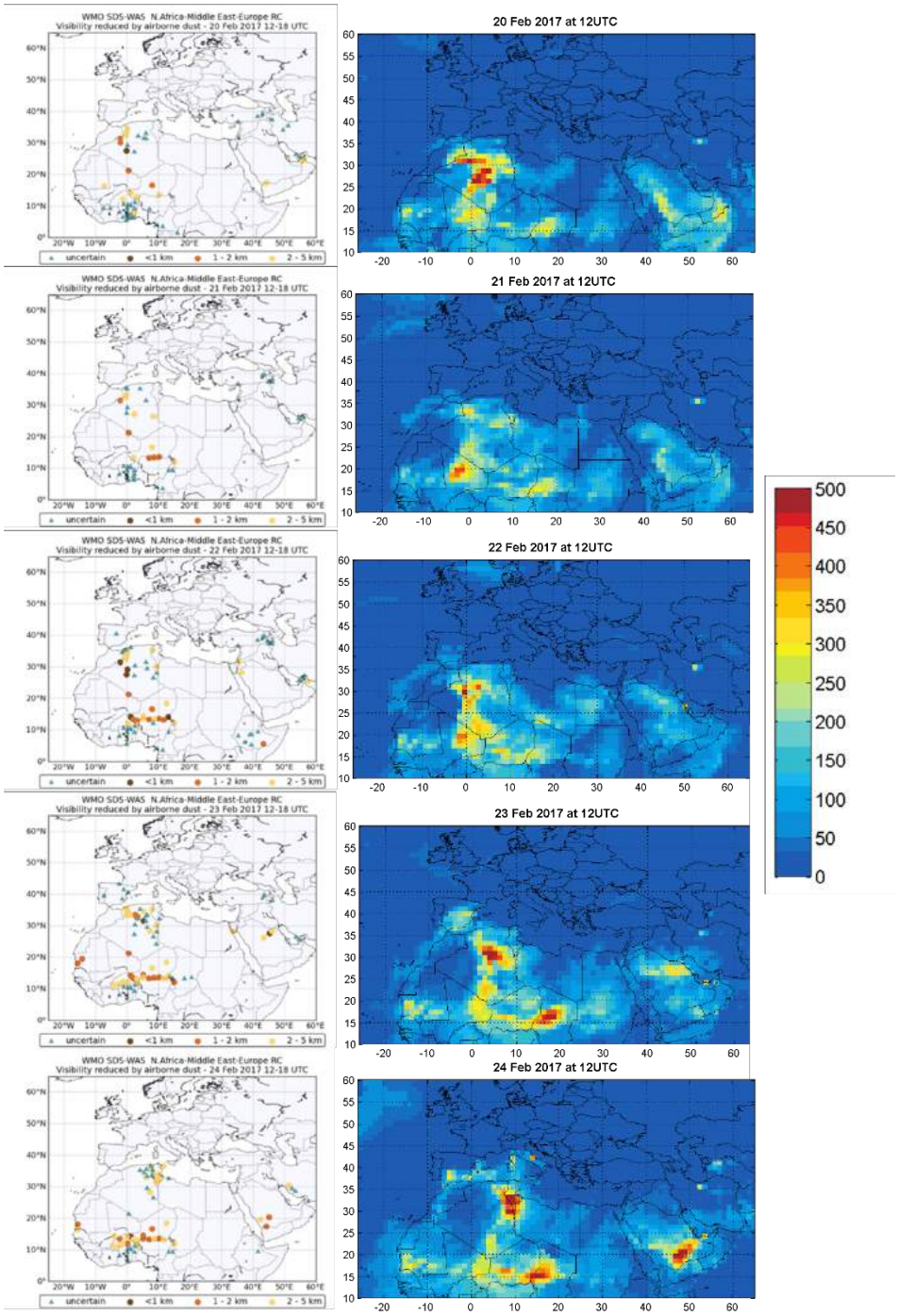


Figure 3.6.2. Visibility from METAR or SYNOP stations downloaded from the SDS-WAS Regional Center (left column) and PM10 from o-suite (right column) during the case analysis from 20-24 February 2017. The maps show cases of visibility reduction by sand or dust to less than 5 km reported in METAR or SYNOP bulletins. More than 1,500 stations are checked every 6 hours. Brownish circles indicate stations where 'sand' or 'dust' has been explicitly reported. Triangles indicate stations where the present weather has been reported as 'haze', meaning that the visibility is reduced by particles of unspecified origin.

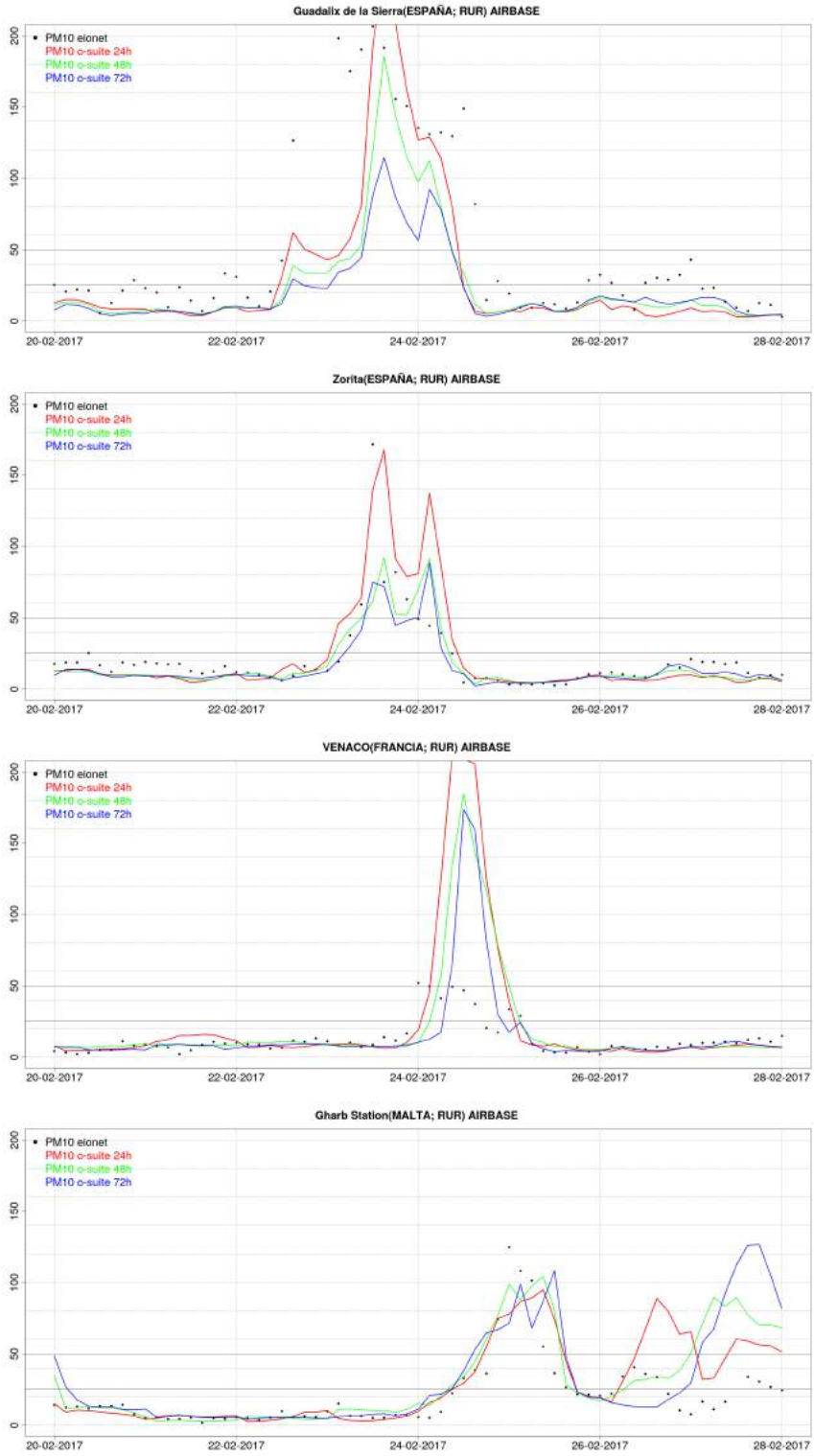


Figure 3.6.3. Observed PM10 from Airbase (black dots) and modelled PM10 from o-suite at 24h (red line), 48h (green line) and 72h (blue line ) time forecasts at Guadalix de la Sierra (Spain-Central Iberian Peninsula), Zorita (Spain-Eastern Iberian Peninsula), Venaco (France-Corsica) and Gharb (Malta) from 20-28 February 2017.

## 3.7 Dust event over Central-Eastern Mediterranean: 7-9 November 2016

*Taken from the SON-2016 NRT validation report [nrt2017d].*

A dust plume that originated in Algeria, moved towards the Central and Eastern Mediterranean on 7-9 November 2016, as detected by the ground visibility stations (see Fig. 3.7.1). The event was associated with the movement of a barometric trough that had caused the formation of clouds.

The full episode was well predicted by the CAMS o-suite as is shown by the comparison of the dust aerosol optical depth (DOD) predicted by CAMS o-suite and observed AOD by MODIS from 6$^{th}$ to 9$^{th}$ November 2016 at 12UTC in Fig. 3.7.2. The model could predicted the arrival and the moment of the maximum peak of the dust plume over the affected AERONET sites in the Mediterranean, although the maximum DOD concentration was underestimated.

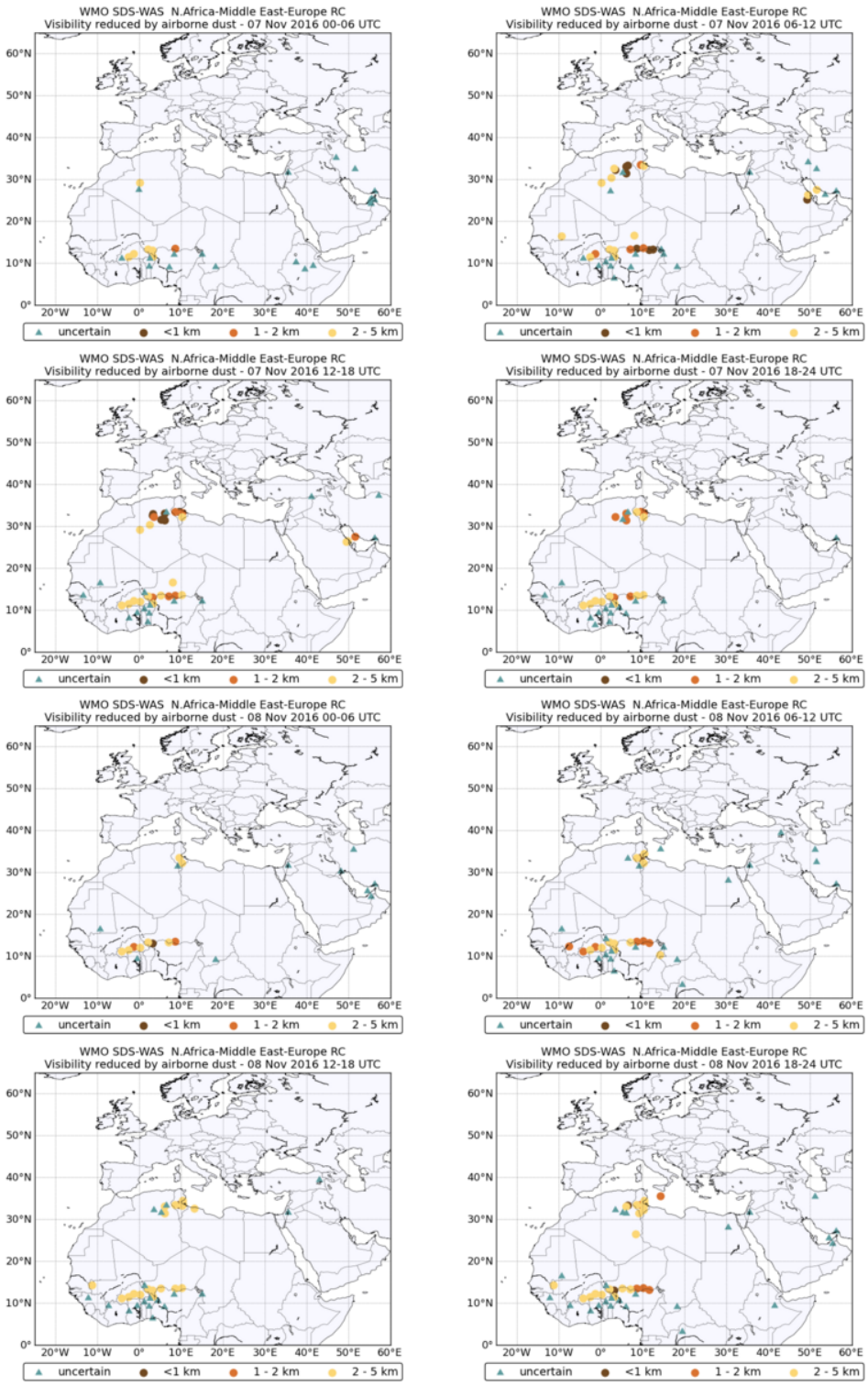


Figure 3.7.1. Visibility from METAR or SYNOP stations from SDS-WAS Regional Center during the case analysis from 7th to 8st November 2016. The maps show cases of visibility reduction by sand or dust to less than 5 km reported in METAR or SYNOP bulletins. More than 1,500 stations are checked every 6 hours. Brownish circles indicate stations where 'sand' or 'dust' has been explicitly reported. Triangles indicate stations where the present weather has been reported as 'haze', meaning that the visibility is reduced by particles of unspecified origin.

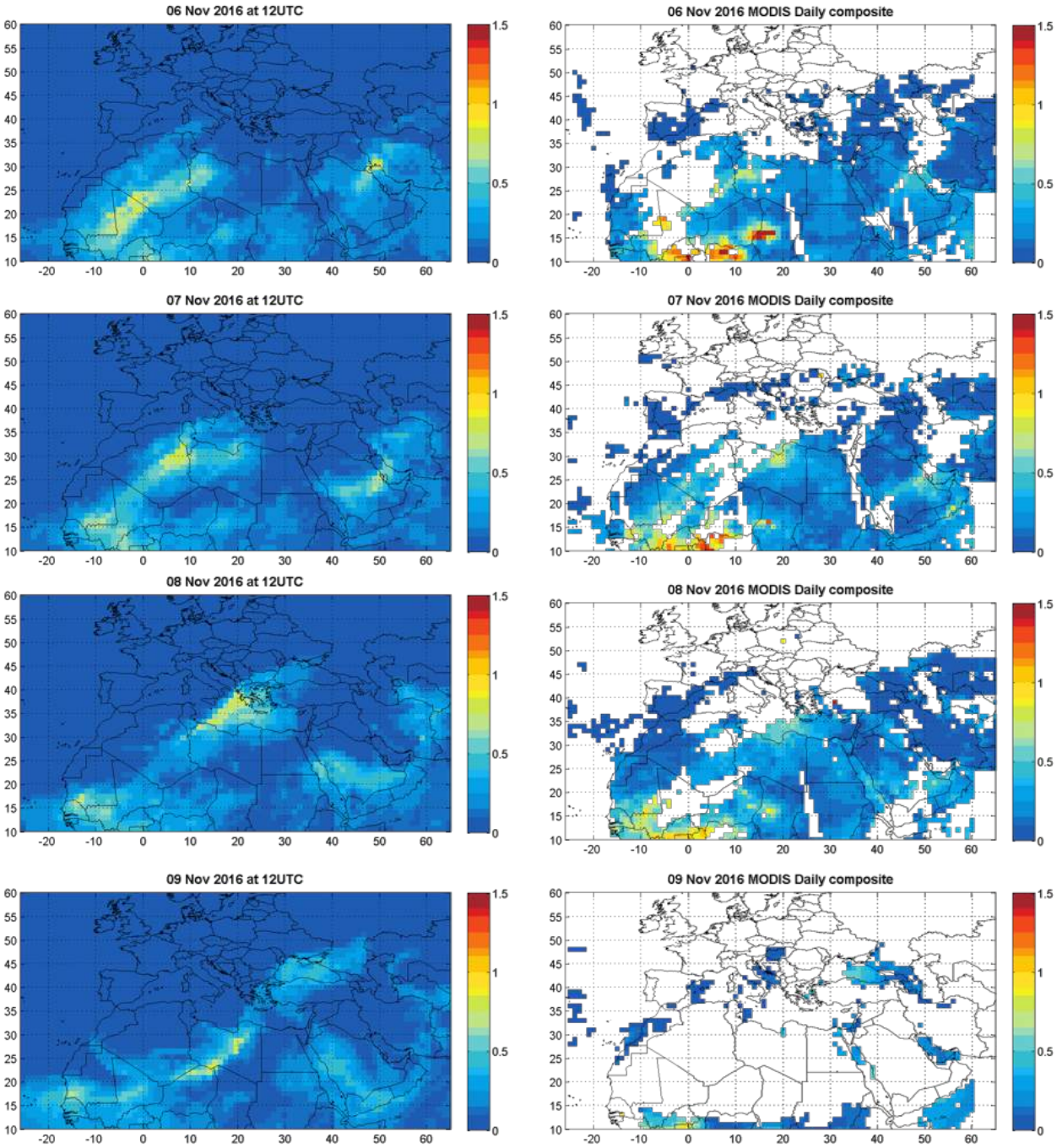


Figure 3.7.2. DOD from o-suite (right column) and AOD from MODIS combined Dark Target and Deep Blue near-real-time aerosol products (left column, MCDAODHD files), for November 6$^{th}$- 9$^{th}$, 2016 at 12UTC.

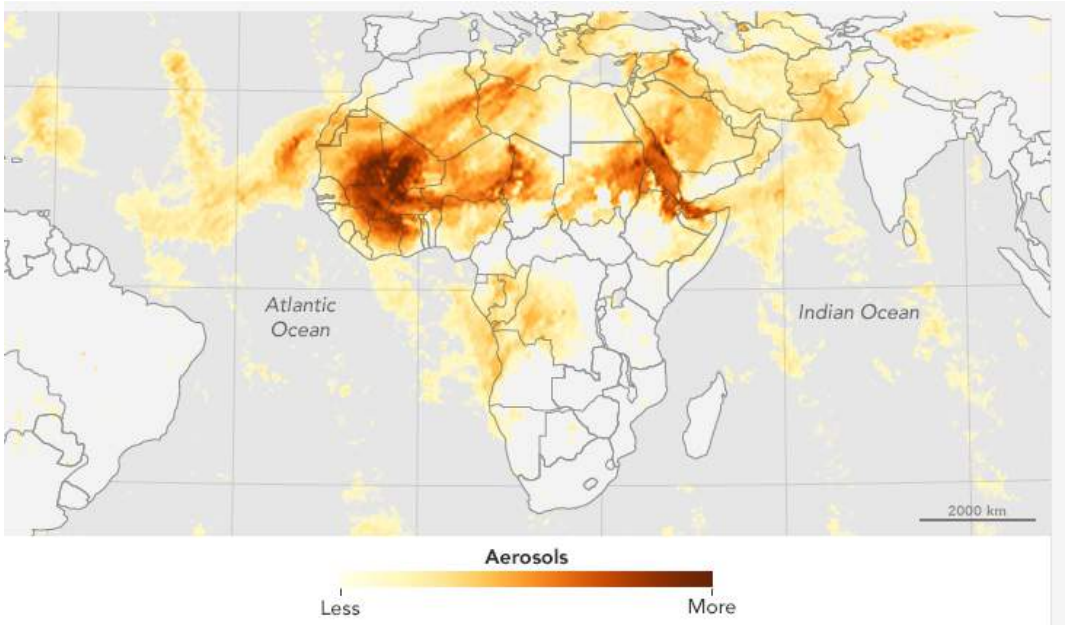


Figure 3.8.1. Aerosol content on June 19, 2016 from the Ozone Mapping Profiler Suite (OMPS) on the Suomi-NPP satellite. High concentrations are represented with shades of deep red; the lowest concentrations are shades of light yellow. The largest, thickest plume appears to stem from the Sahara in western Africa. Source: NASA Ozone Mapping and Profiler Suite.

## 3.8 A dusty period over North Africa, Middle East and Europe: mid-June 2016

*Taken from the JJA-2016 NRT validation report [nrt2016a].*

In mid-June 2016, winds lofted thick plumes of dust from northern Africa's deserts high into the air. On June 19, winds had already swept a plume of dust westward over the Atlantic Ocean and the archipelago of Cabo Verde (Cape Verde) that reached the Canary Islands by June 22. Otherwise, a thinner plume of Saharan dust also spread north toward Europe starting on June 16. This dust outbreak from the Western Sahara was coincident with a plume of dust from Africa's northeast, carried eastward over the Red Sea. Figure 3.8.1 shows the concentration of aerosols on June 19, 2016, produced with data from the Ozone Mapping Profiler Suite (OMPS) on the Suomi-NPP satellite.

Dust aerosol optical depth (DOD) from CAMS has been compared with AOD from MODIS to evaluate the skill of CAMS to track the spatiotemporal evolution of the different dust plumes analysed (Figure 3.8.1). The near-real-time MODIS aerosol product available through the NASA's EOSDIS system (MCDAODHD files), is used for this purpose. It is a level 3 gridded product specifically designed for quantitative applications including data assimilation and model validation. DOD simulated by CAMS o-suite and observed AOD by MODIS from 16$^{th}$ to 22$^{nd}$ June 2016 at 12UTC is shown in Figure 3.8.2. Moreover, DOD values from CAMS o-suite have been compared with those from CAMS control. Multi-Median model generated from the models participating in the WMO SDS-WAS NAMEE Regional Node (http://sds-was.aemet.es/) and AERONET AOD in four AERONET stations strategically located along the path of the different dust plumes.

The CAMS o-suite did timely reproduce the spatial distribution of the different dust plumes over the North Atlantic on 19-21 June, affecting Europe on 17-19 June and the Red Sea on 17-20 June as observed by MODIS (Figure 3.8.2). We can see how CAMS o-suite tracks fairly well the changes in both shape and size of the dust layer throughout the dusty period. The whole episode is well simulated by CAMS o-suite and CAMS control, in the North Atlantic (Dakar and Santa Cruz de Tenerife in Figure 3.8.3) and Europe (see IMAA Potenza in Figure 3.8.3). In the Kaust Campus AERONET site, all the models underestimate the maximum AOD peak observed on June 18$^{th}$ (see Figure 3.8.3). The dust plume affecting the Red Sea has its origin in the Tokar Delta on June 15$^{th}$ and out over the Red Sea and toward the Arabian Peninsula the next days arriving at the AERONET Kaust Campus (in Saudi Arabia) on June 18$^{th}$ (see Figure 3.8.3). The wind gusts that caused the dust outbreak on June 15 were due to a cold front moving south-east. The front was related to a cyclone centred near the Persian Gulf, and it caused turbulent mixing of air and a series of associated haboobs that any of the models can reproduce.

Since weather records have a good spatial and temporal coverage, horizontal visibility observations included in meteorological reports can be used as an alternative way to monitor dust events. Visibility is mainly affected at ground by the presence of aerosols and water in the atmosphere. On surface level, o-suite can track the reduction of visibility of the study period (see Figure 3.8.4) localising the origin of the event over Northern Algeria and the Tokar Delta on June 17$^{th}$ and in Mauritania and Mali on June 19-20.

Visibility records also show an intense dust event with origin in Iraq on June 16 moving southwards crossing the Persian Gulf the next days. This dust outbreak is reproduced by CAMS o-suite (see Figure 3.8.2 and see Figure 3.8.4) but, its intensity is underestimated as it is partly shown in the AOD comparison with MODIS (see Figure 3.8.2).

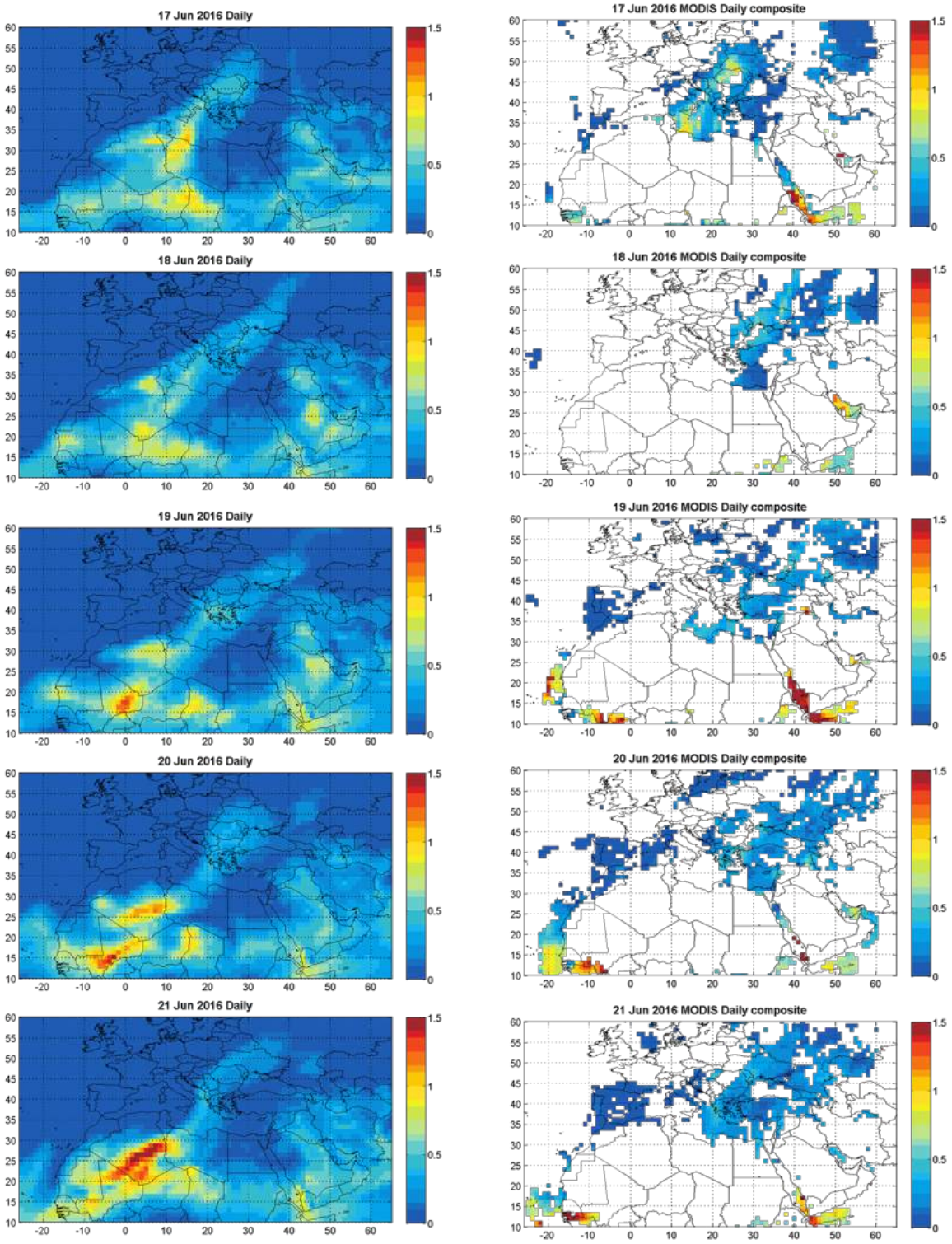


Figure 3.8.2. DOD from o-suite (right column) and AOD from MODIS combined Dark Target and Deep Blue aerosol products (left column), for June 17th- 21st, 2016 at 12UTC.

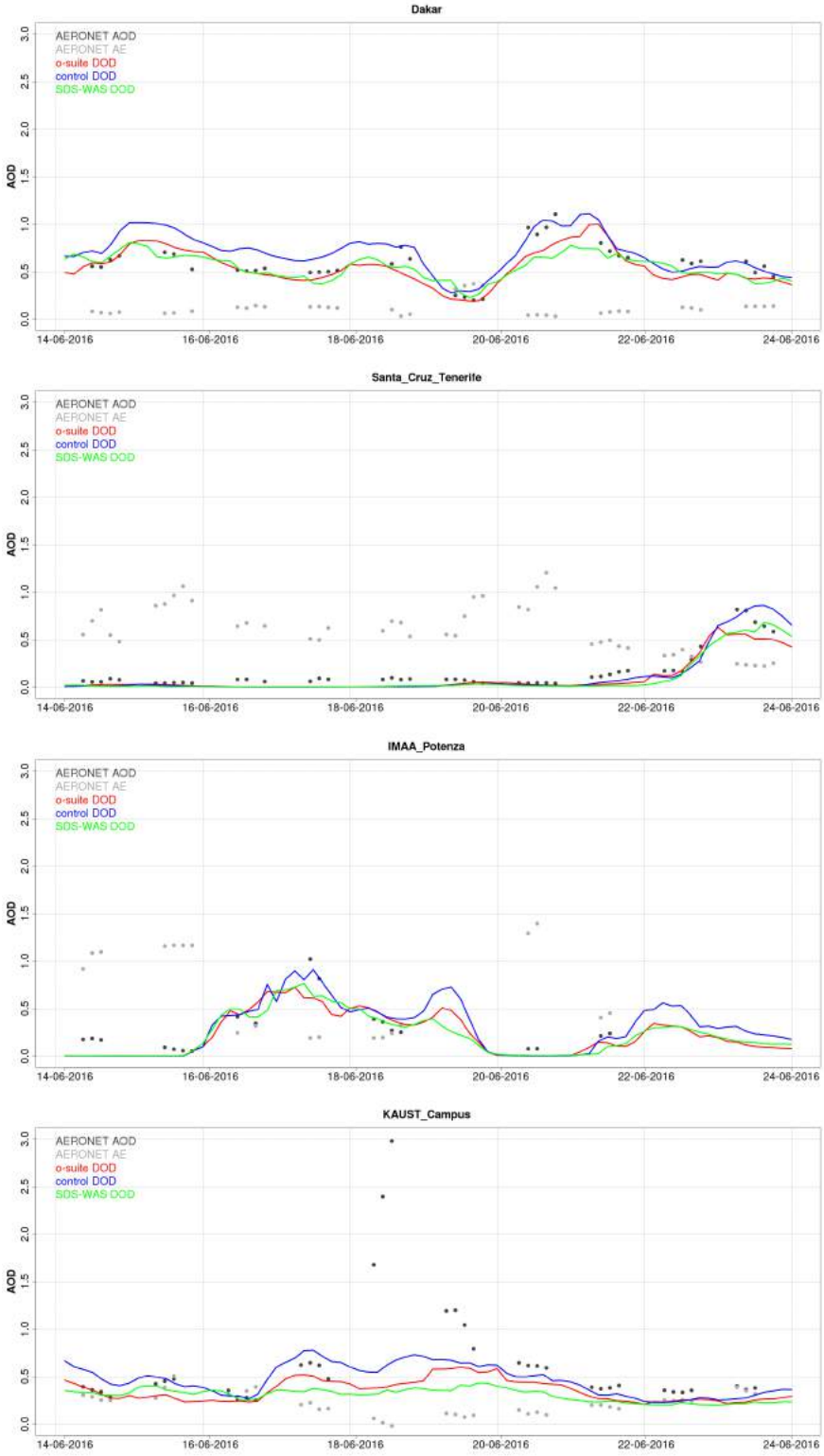


Figure 3.8.3. AOD at 550 nm from AERONET (black), DOD at 550 nm from the o-suite (blue), DOD at 550 nm from the control run (red), and DOD at 550 nm from SDS-WAS Multi-model Median (green) at Ben Salem (Tunisia) and Etna (Italy) AERONET sites during the case analysis from 5$^{th}$ to 18$^{th}$ May 2016.

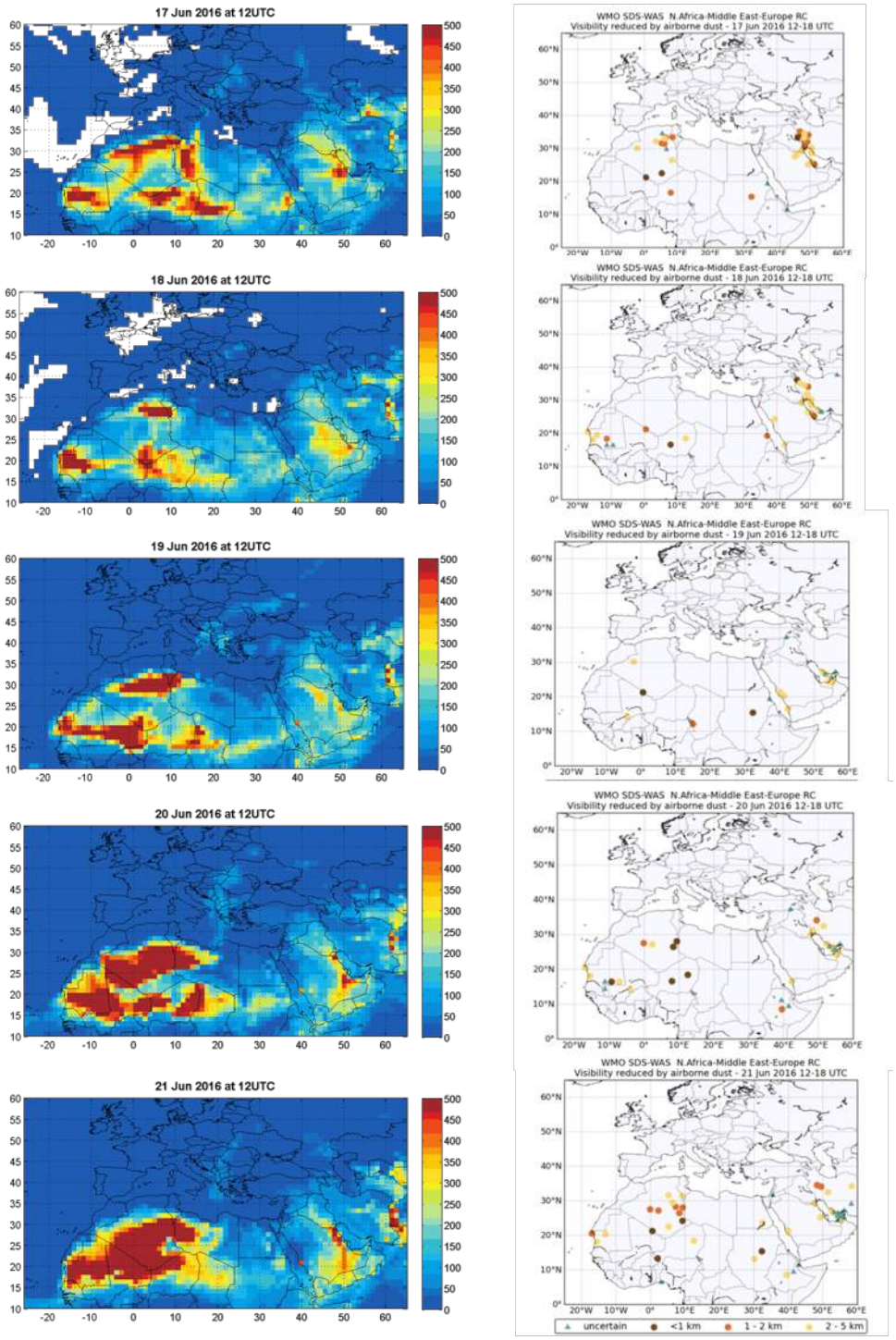


Figure 3.8.4. Dust surface concentration o-suite (right column) and visibility (left column) from METAR or SYNOP stations from SDS-WAS Regional Center during the case analysis from 17th to 21st June 2016. The maps show cases of visibility reduction by sand or dust to less than 5 km reported in METAR or SYNOP bulletins. More than 1,500 stations are checked every 6 hours. Brownish circles indicate stations where 'sand' or 'dust' has been explicitly reported. Triangles indicate stations where the present weather has been reported as 'haze', meaning that the visibility is reduced by particles of unspecified origin.

## 3.9 A dust event over the Western Mediterranean in May 2016

*Taken from the MAM-2016 NRT validation report [nrt2016b].*

The selected dust event corresponds to the period from May 9th to 13th, 2016. Around the 9th of May, a layer of dust moved from Algeria covering the area around the Central Mediterranean and moving later eastwards Eastern Mediterranean.

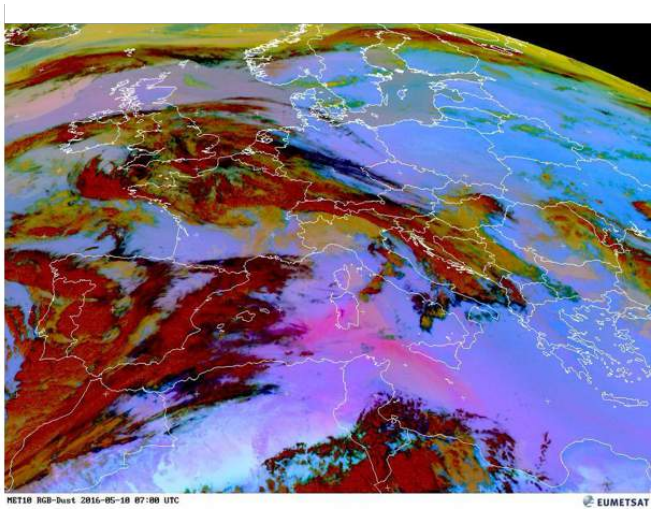


Figure 3.9.1. MSG/SEVIRI RGB Dust image (red is clouds and pink is dust), 10 May 7:00 UTC.

Three-hourly dust aerosol optical depth (DOD) from CAMS o-suite (Benedetti et al., 2009; Morcrette et al., 2009) has been compared with AOD from MODIS in order to evaluate the skill of CAMS o-suite to mimic the spatio-temporal evolution of the dust plume (Figure 3.9.1). The near-real-time MODIS aerosol product available through the NASA's EOSDIS system (MCDAODHD files), is used for this purpose. DOD simulated by the CAMS o-suite and observed AOD by MODIS from 9th to 13th May 2016 at 12UTC is shown in Figure 3.9.2. Moreover, DOD values from CAMS o-suite have been compared with those from CAMS control, Multi-Median model and AERONET AOD (Level 1.5) in four AERONET stations strategically located along the path of the dust plume over at Tizi-Ouzou (Algeria), Ben Salem (Tunisia) and Etna (Italy). Results are shown in Figure 3.9.3. Finally, visibility from METAR or SYNOP stations processed by the SDS-WAS NAMEE Regional Node is used to qualitatively evaluate the modelled CAMS surface concentrations.

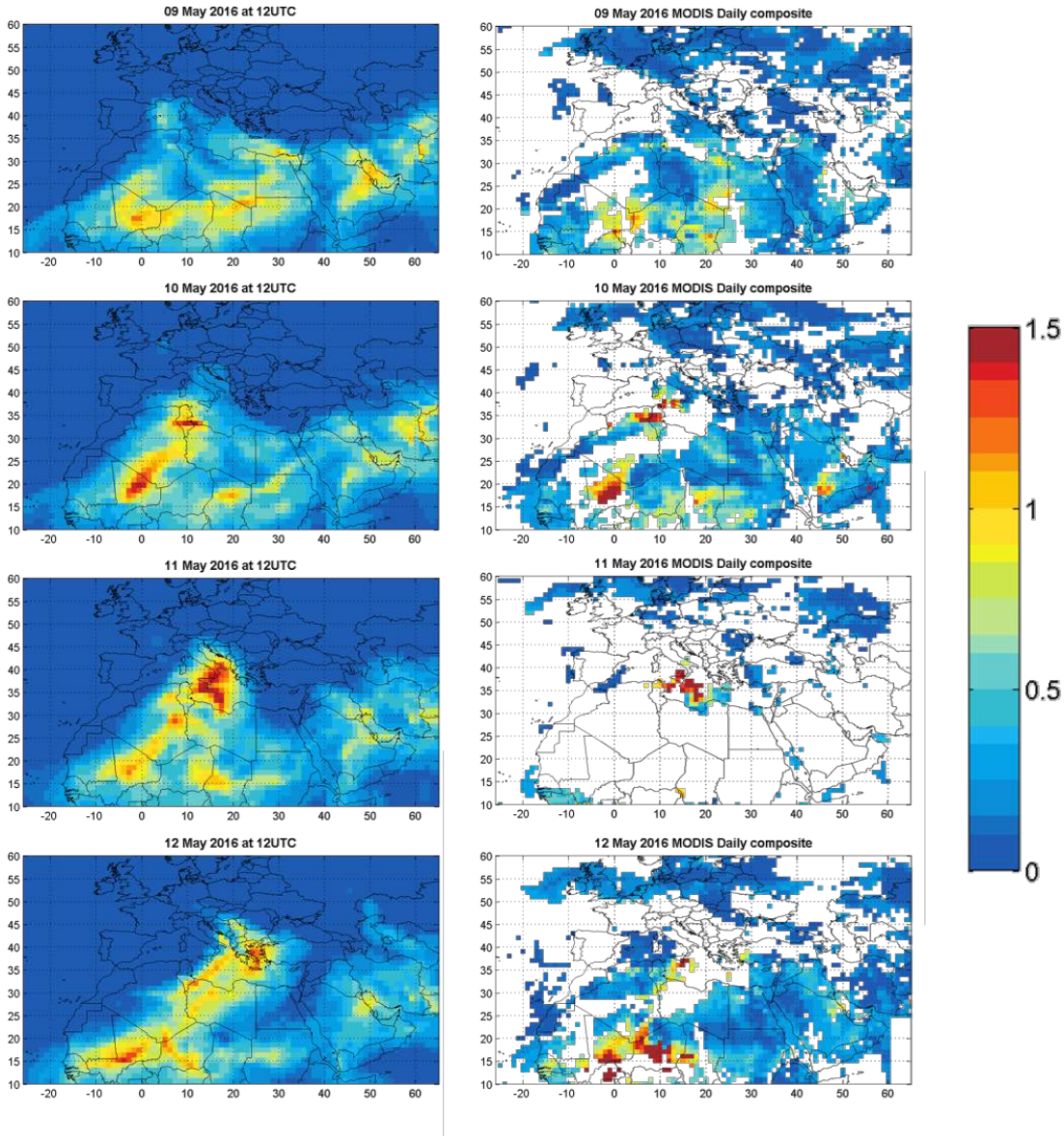


Figure 3.9.2. AOD from MODIS combined product form Dark Target and Deep Blue (left column), and DOD from o-suite (right column), for January 16th-20th, 2016 at 12UTC.

Dust mobilization is confined over Algeria on the 9th of May, caused by a low pressure over North Africa. Low AOD and high AE are observed over Tunisia (see Ben Salem in Figure 4.2.3) on May 8th. The next days, dust is blown over Central Mediterranean affecting Tunisia and Italy from 10 to 12 May (see Figure 3.9.2). The Ben Salem and Etna AERONET sites show consecutively an increase in AOD (AOD up to 2.5 in Ben Salem) associated to a sharp decrease of AE associated with the arrival of the dust plume.

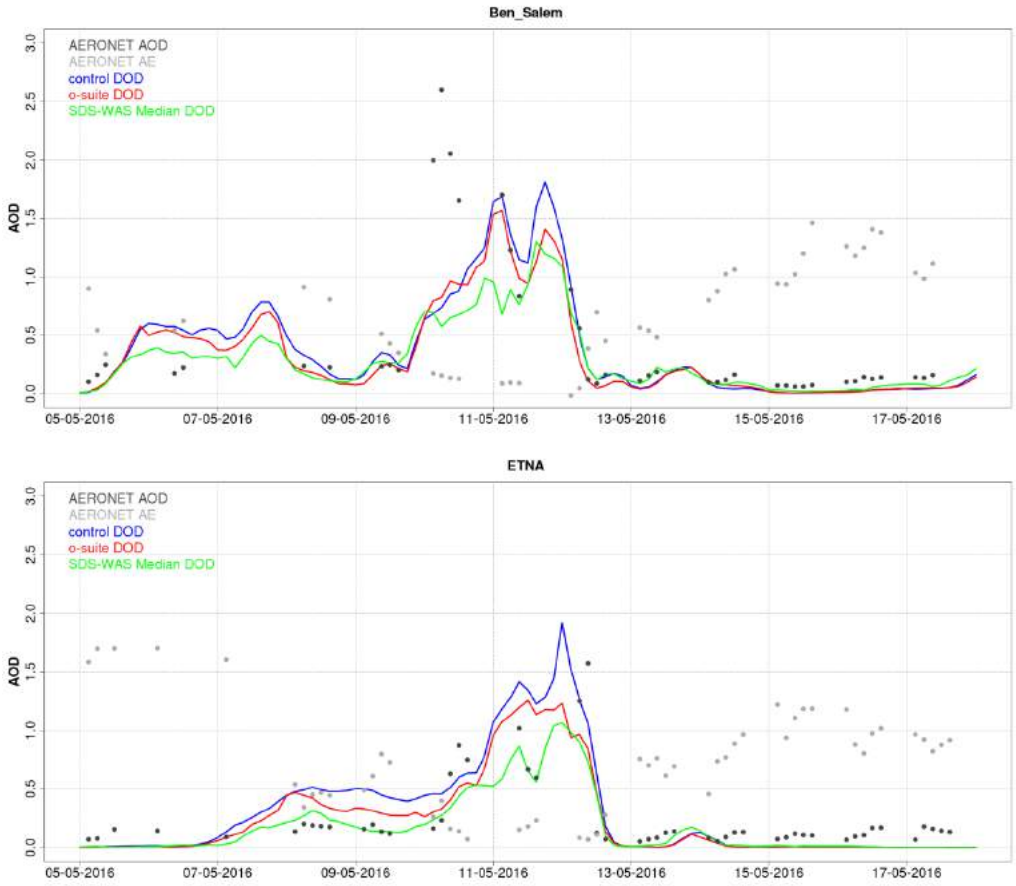


Figure 3.9.3 AOD at 550 nm from AERONET (black), DOD at 550 nm from the o-suite (blue), DOD at 550 nm from the control run (red), and DOD at 550 nm from SDS-WAS Multi-model Median (green) at Ben Salem (Tunisia) and Etna (Italy) AERONET sites during the case analysis from 5th to 18th May 2016.

The o-suite is able to timely reproduce the spatial distribution of the dust plume as observed by MODIS (Figure 3.9.2) over the Mediterranean. We can see how CAMS o-suite tracks fairly well the changes in both shape and size of the dust layer throughout the episode. The whole episode is well simulated by CAMS o-suite and CAMS control, although in Ben Salem none of the models could reproduce the AOD peak observed on May 10th (see Figure 3.9.3). The observed peak can be associated with cloud contamination because dense clouds were present during all the event (see a long cumulus line over Central Mediterranean in Figure 3.9.1).

Since weather records have an excellent spatial and temporal coverage, horizontal visibility observations included in meteorological reports can be used as an alternative way to monitor dust events. Visibility is mainly affected at the ground by the presence of aerosols and water in the atmosphere. At the surface level, the o-suite is able to track the reduction of visibility related to this event (see Figure 3.9.4), localizing the origin of the event over Algeria on May 9th, with the dust moving northwards to Tunisia on May 10th, crossing the Mediterranean and reaching Italy on May 11th and Greece and Turkey on May 12th.

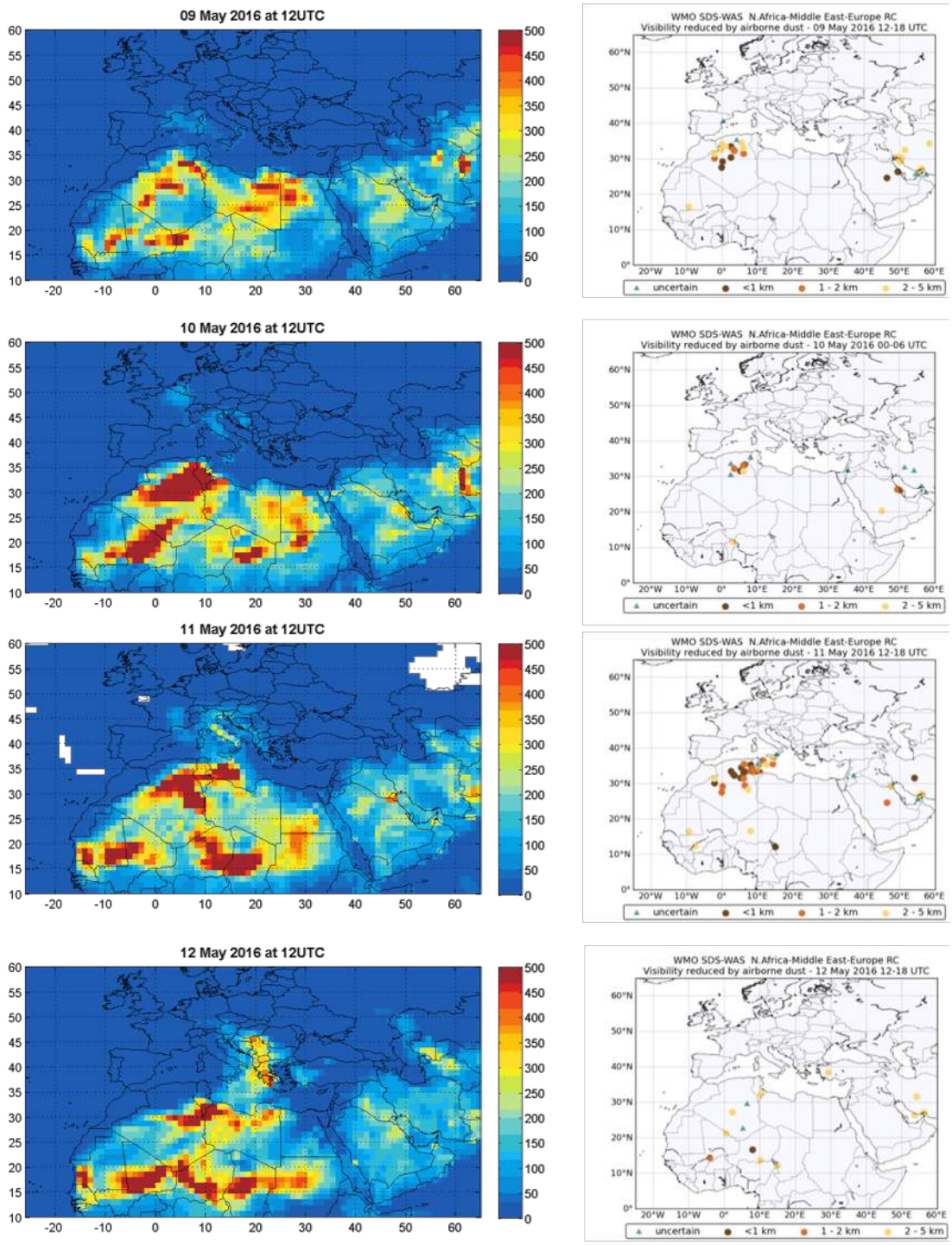


Figure 3.9.4. Dust surface concentration o-suite (left column) and visibility (right column) from METAR or SYNOP stations from SDS-WAS Regional Center from 10th to 12th May 2016. The maps show cases of horizontal visibility reduction by sand or dust to less than 5 km reported in METAR or SYNOP bulletins. More than 1,500 stations are checked every 6 hours. Brownish circles indicate stations where 'sand' or 'dust' has been explicitly reported. Triangles indicate stations where the present weather has been reported as 'haze', meaning that the visibility is reduced by particles of unspecified origin.

## 1.1 A dust event over Eastern Mediterranean-Middle East in January 2016

*Taken from the DJF-2016 NRT validation report [nrt2016c].*

Around 17 January 2016, a strong dust plume originated from Libya and moved eastwards affecting part of the Eastern Mediterranean and Middle East. Three-hourly dust aerosol optical depth (DOD) from the o-suite has been compared with AOD from MODIS (level 3 gridded product) to evaluate the skill of the o-suite to track the spatio-temporal evolution of the dust plume (Figure 3.10.1). DOD simulated by the o-suite and observed AOD from MODIS from 16th to 20th January 2016 at 12UTC is shown in Figure 3.11.2. Moreover, DOD values from the o-suite, the control and from the Multi-Median model generated from the models participating in the WMO SDS-WAS NAMEE Regional Node (http://sds-was.aemet.es/) have been compared with observations from AERONET AOD (Level 1.5) at two stations strategically located along the path of the dust plume over the Cairo EMA (Egypt) and Sede Boker (Israel). Results are shown in Figure 3.10.3.

Both the o-suite and control experiment captured quite well the passage of the dust plume on AERONET stations, as well as the SDS-WAS Multi-Median model. The AOD spatiotemporal evolution given by the o-suite closely resembles the MODIS retrievals. Still the CAMS models underestimate the maximum observed AOD over Lybia and Egypt (maximum DOD ~ 1 for o-suite and maximum AOD up to 1.5 for MODIS).

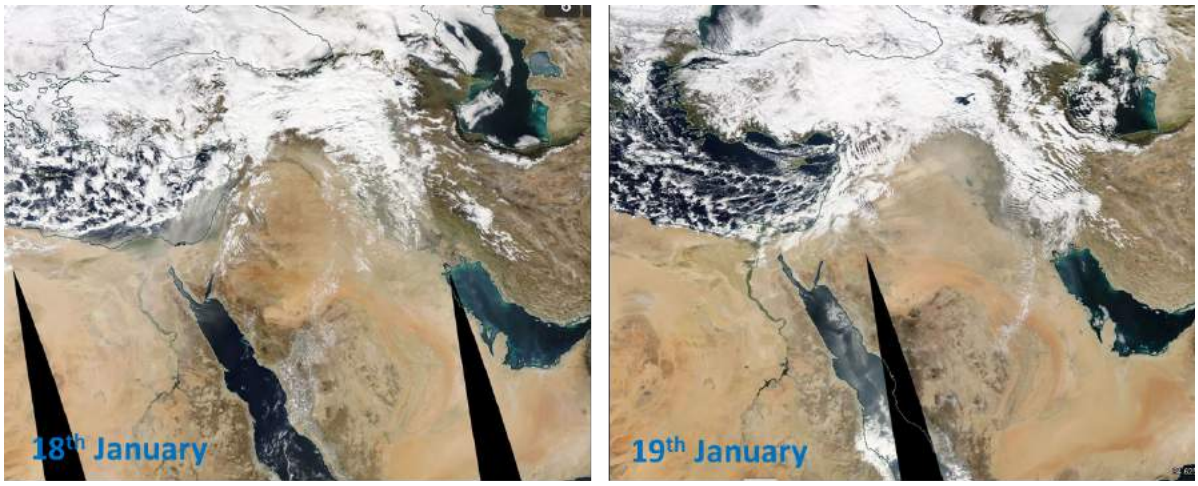


Figure 3.10.1. MODIS-Aqua image, daily composite for 18 and 19 January 1016 (overpass between 9-12 UTC), showing a large dust plume moving in eastward direction over Egypt and other countries in the Middle East.

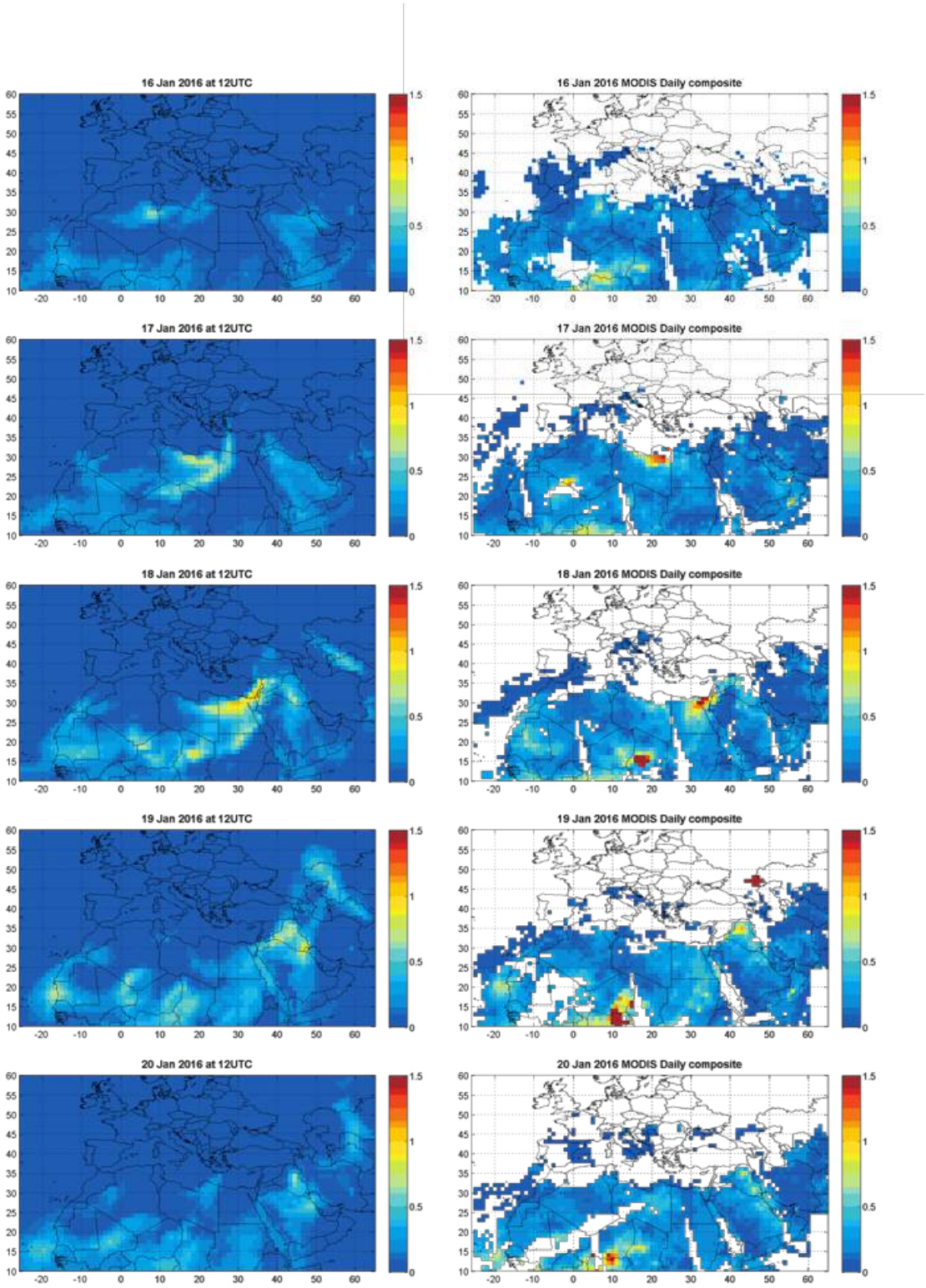


Figure 3.10.2. DOD from o-suite (right column) and AOD from MODIS (left column), for January 16th-20th, 2016 at 12UTC.

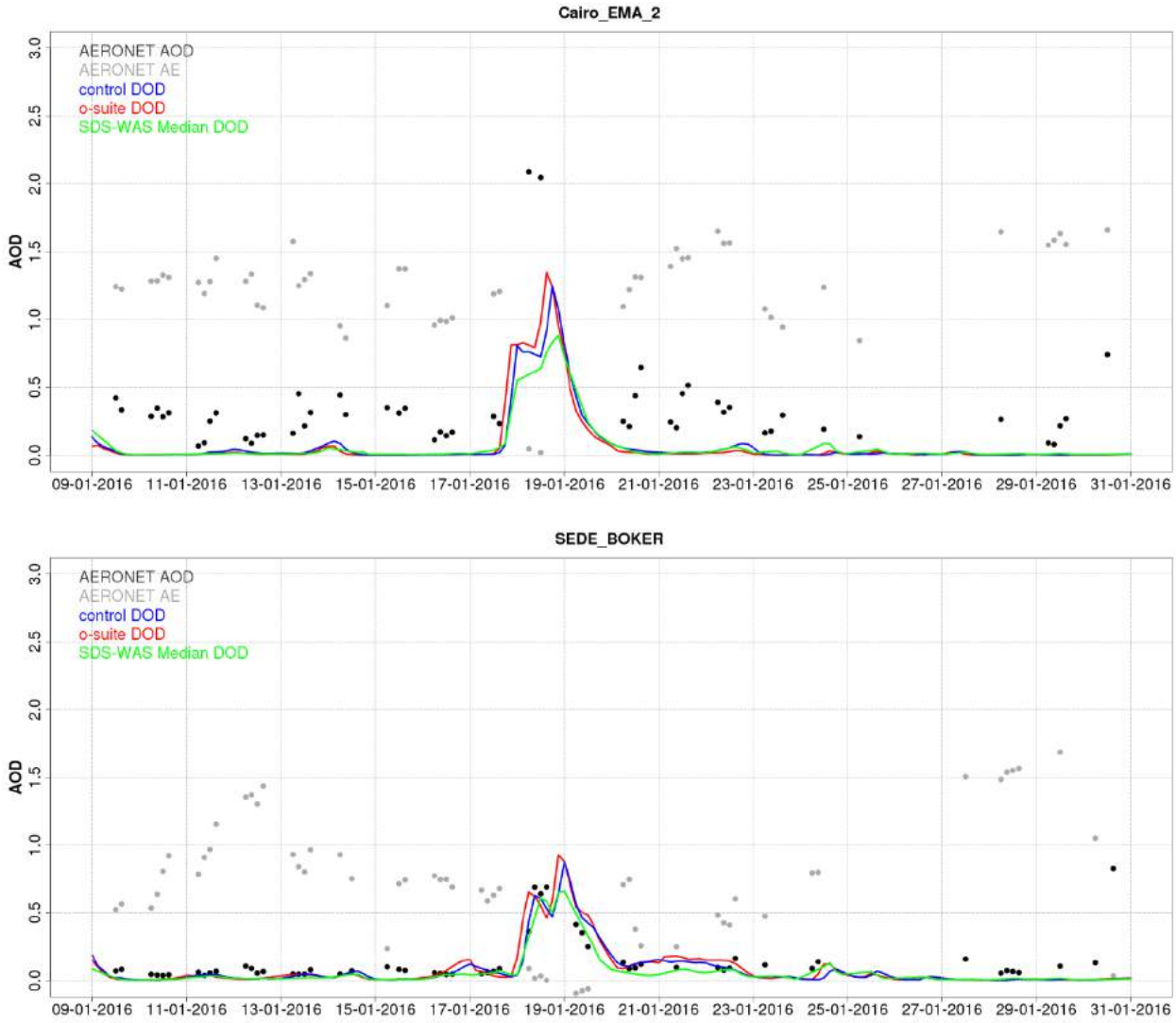


Figure 3.10.3. AOD at 550 nm from AERONET (black), DOD at 550 nm from the o-suite (blue), DOD at 550 nm from the control run (red), DOD at 550 nm from SDS-WAS Multi-model Median (green) at Cairo EMA and Sede Boker AERONET sites during the case analysis from 9th to 31th January 2016.

## 3.10 A dust event over Canary Islands in November 2015

*Taken from the SON-2016 NRT validation report [nrt2016d].*

A dust event was selected in the period around 13 November, when a high layer of dust moved from north-western Africa covering the area around the Canary Islands. Three-hourly dust aerosol optical depth (DOD) from CAMS o-suite has been compared with AOD from MODIS in order to evaluate the skill of CAMS o-suite to track the spatio-temporal evolution of the dust plume (Figure 3.11.1). The near-real-time MODIS aerosol product available through the NASA's EOSDIS system (MCDAODHD files), is used for this purpose. It is a level 3 gridded product specifically designed for quantitative applications including data assimilation and model validation. DOD simulated by CAMS o-suite and observed AOD by MODIS from 11th to 15th November 2015 at 12UTC is shown in Figure 3.11.2. Moreover, DOD values from CAMS o-suite have been compared with those from CAMS

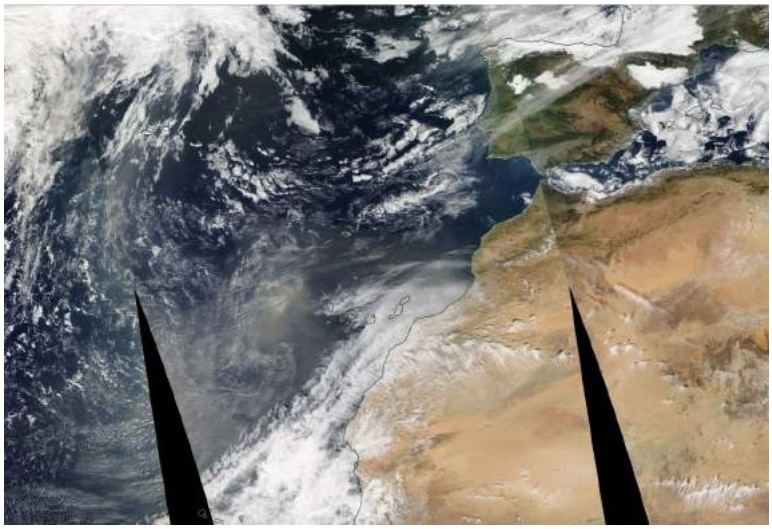

Figure 3.11.1. MODIS-Aqua image, 13 November 14:35 UTC.

control, the Multi-Median model generated from the models participating in the WMO SDS-WAS NAMEE Regional Node (http://sds-was.aemet.es/), MODIS AOD, and AERONET AOD (Level 1.5) in four AERONET stations strategically located along the path of the dust plume over the Canary Islands (Santa Cruz de Tenerife and Izana sites) and North Western Africa (Capo Verde and Oujda-Morocco sites). Results are shown in Figure 3.11.3.

Dust mobilization is confined over Mauritania on 9th November, and is caused by an anticyclone over Iberian Peninsula. Over Morocco (see Oujda in Figure 3.11.3), low AOD and high AE are observed during all the study period. The next days, dust is blown over sub-Tropical Atlantic region affecting Canary Islands from 11 to 16 November (see Figure 3.11.2). The two AERONET sites at Tenerife (Santa Cruz de Tenerife and Izana; see Figure 3.11.3) show consecutively an increase in aerosol optical depth (AOD up to 0.5 in Santa Cruz de Tenerife) associated to a sharp decrease of the Ångstrom Exponent (AE) caused by the arrival of the dust plume. In Santa Cruz de Tenerife some isolated values with AOD ~ 2, probably are associated to cloud contamination. Dense clouds were present during the whole period of the event, evidenced by a long cumulus line over the Islands in Figure 3.11.1.

The o-suite is able to reproduce the timing and spatial distribution of the dust plume as observed by MODIS (Figure 3.11.2) over the ocean, although the spatial extent of the dust layer is limited. We can see how CAMS o-suite tracks fairly well the changes in the shape and size of the dust layer throughout the episode. CAMS o-suite, CAMS control and SDS-WAS Multi-Median models show a clear overestimation on the onset of the dust event in both the Santa Cruz de Tenerife and Izana stations. At Izana station, which is at 2,400 m a.s.l., CAMS o-suite, CAMS control and SDS-WAS Multi-Median show a slight overestimation. This is explained by the fact that during this episode the dust layer was confined to altitudes below 4 km a.s.l. over Canary Islands, as confirmed by CALIPSO observations. The whole episode is well simulated by CAMS o-suite and CAMS control, although in Santa Cruz de Tenerife and Izana stations (see Figure 3.11.3) on 11nd-16th November CAMS o-suite better reproduces the AOD peak than CAMS control.

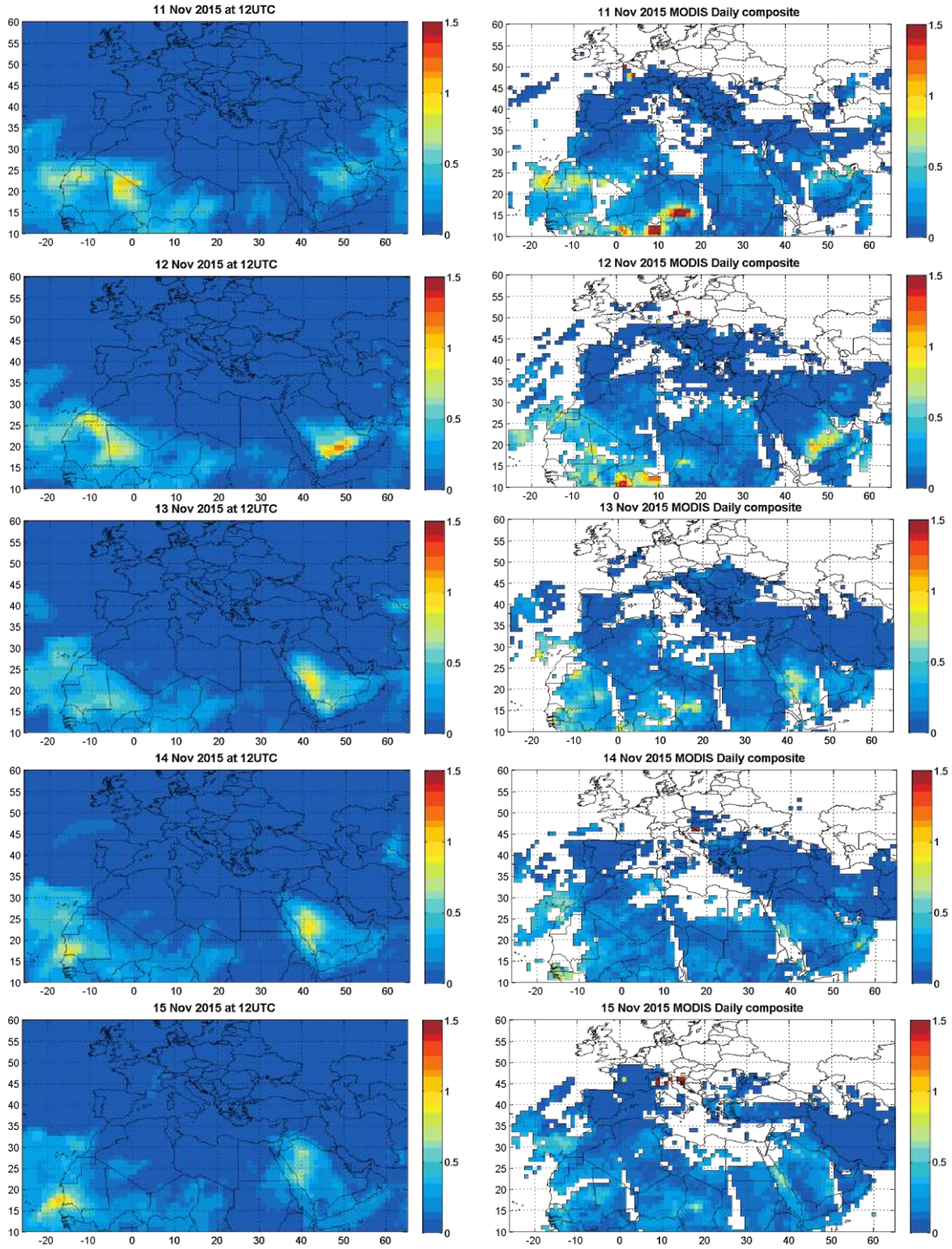


Figure 3.11.2. DOD from o-suite (right column) and AOD from MODIS (left column), for November 11th-15th, 2015 at 12UTC.

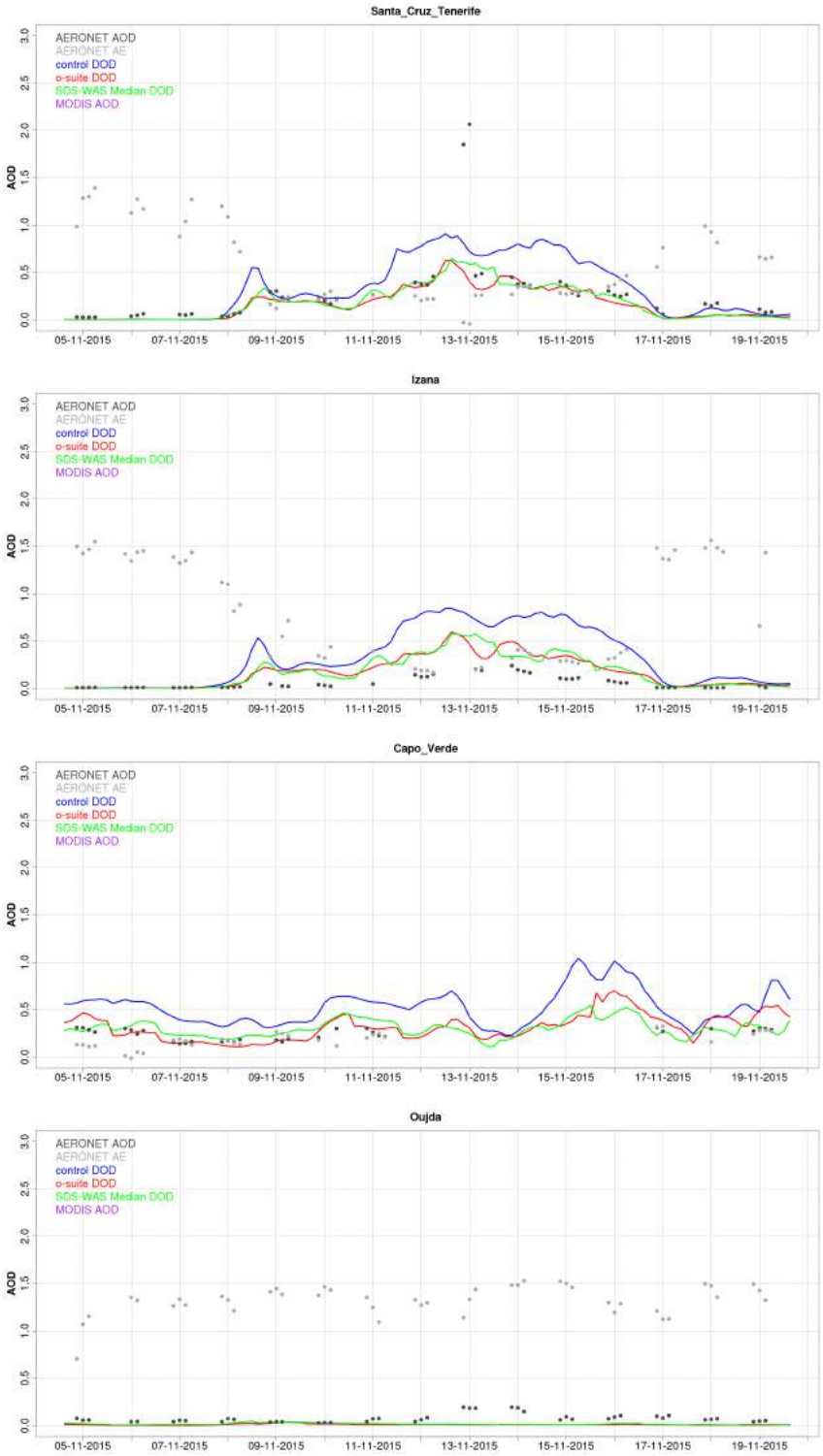


Figure 3.11.3. AOD at 550 nm from AERONET (black), DOD at 550 nm from the o-suite (blue), DOD at 550 nm from the control run (red), AOD retrieved from MODIS-AQUA (purple triangles) and DOD at 550 nm from SDS-WAS Multi-model Median (green) at Santa Cruz de Tenerife, Izana, Capo Verde and Oujda AERONET sites during the case analysis from 5$^{th}$ to 20$^{th}$ November 2015.

## 3.11 A dust event over the Middle East on September 2015

*Taken from the JJA-2015 NRT validation report [nrt2015a].*

A large dust storm hit the western regions of the Middle East on September 2015, and resulted in the hospitalization of hundreds of people and public health warnings, as was reported by the media. A surface level low pressure centre kicked off the dust storm in northern Iraq on September 6. On September 7 (Figure 3.12.3, top image), an intense dust plume swept Syria, the Mafraq region of Jordan, and part of Turkey's Mediterranean coast. On September 8 (Figure 3.12.1) dust had affected Lebanon, Israel, Jordan, Cyprus, and the Palestinian Territories. On September 9 the dust plume moved southwest and spread over northeastern Egypt and the Gulf of Suez. This was a rather unusual direction for the dust plume to travel.

The influx of dust triggered a rash of canceled flights, closed ports, and suspension of daily activities for many people. In several countries, authorities warned elderly and young children to stay indoors. The number of people visiting hospitals with respiratory problems increased significantly, and several fatalities were attributed to dust.

While satellites observed the dust from above, ground-based air quality sensors recorded remarkable amounts of particulate matter. In Jerusalem, pollution levels were 173 times higher than standard, according to media reports.

Three-hourly dust aerosol optical depth (DOD) from the o-suite has been compared with AOD from MODIS in order to evaluate the skill to predict the spatio-temporal evolution of the dust plume. The Sede Boker AERONET station in southern Israel showed a dramatic increase in aerosol optical depth (AOD > 3.5 on September 8, see Figure 3.12.2).

DOD values from the o-suite have been compared with those from the control experiment, Multi-Median model generated from the models participating in the WMO SDS-WAS NAMEE Regional Node (http://sds-was.aemet.es/), MODIS AOD, and AERONET AOD (Level 1.5) in four AERONET stations strategically located along the path of the dust plume over the Eastern Mediterranean, Israel (Sede Boker and Eilat) and Egypt (Cairo EMA). Results are shown in Figure 3.12.2.

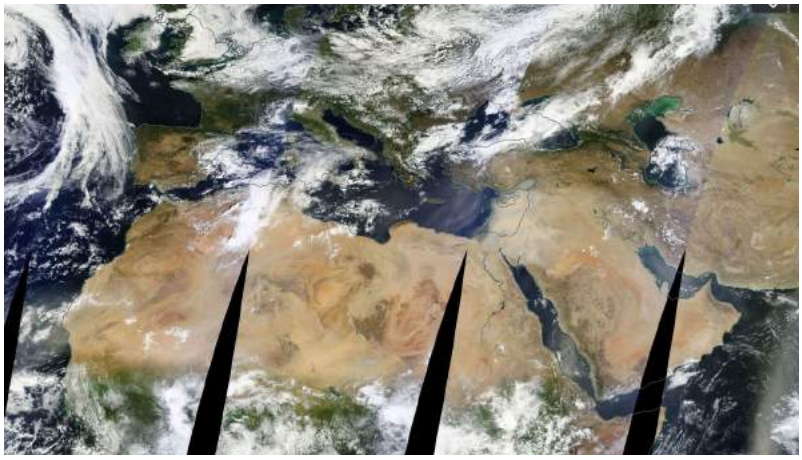

Figure 3.12.1. Daily composite Aqua-MODIS, September 8th 2015.

The westwards movement of the dust plume is well tracked by the models matching the increase of DOD/AOD and the corresponding decrease of Angstrom exponent values (below 0.5) when the dust plume overpasses each AERONET station. Although the whole episode is well captured by the o-suite and control, they tend to strongly underestimate dust loads (Figure 3.12.3) on 8th September. During the maximum dust load (AOD > 3.5), the o-suite produces higher AOD values than control, although underestimating strongly the observed values (maximum AOD values up to 1). Simulated AOD values from models fit well background values from AERONET before the dust event, except in Cairo where urban pollution is clearly observed with relatively high AERONET AOD background values.

DOD simulated by the o-suite and AOD observed by MODIS, from 6th to 10th September 2015 at 12UTC, is shown in Figure 3.12.3. AOD data from MODIS confirmed that the o-suite was able to reproduce the timing and the spatial distribution of the dust plume over Syria, parts of Lebanon, Israel, Turkey, Cyprus and Egypt. The comparison with the daily AOD MODIS Deep Blue Product shows how the o-suite reproduces well the high values over Syria (AOD > 1) which corresponds to dust emissions associated with this event on 7th September 2015. However, the models strongly underestimated the very high AOD values (by up to a factor of 3) observed by MODIS. Besides this specific episode, we can see that the o-suite reproduced quite well some high dust areas observed by MODIS Deep Blue (Figure 3.12.3) over Mauritania-Senegal, northern Algeria and Libya on September 7-10.

All models underestimated significantly the episode. The two ingredients needed for a sand and dust storm are an availability of dust or sand particles at the surface and enough sustained wind to get those particles moving. In the current event, the dust outbreak was driven by mesoscale convective phenomena associated with a low pressure system which is difficult to resolve by global models. Moreover, based on Ginoux et al. (2012), the dust sources in the current event in Syria are associated with a large agricultural region northeast of Raqqa that is known as a particularly abundant dust source. In addition, there are several salt flats along the Syria-Iraq border that contribute dust. These desert dust sources was not well described by the model.

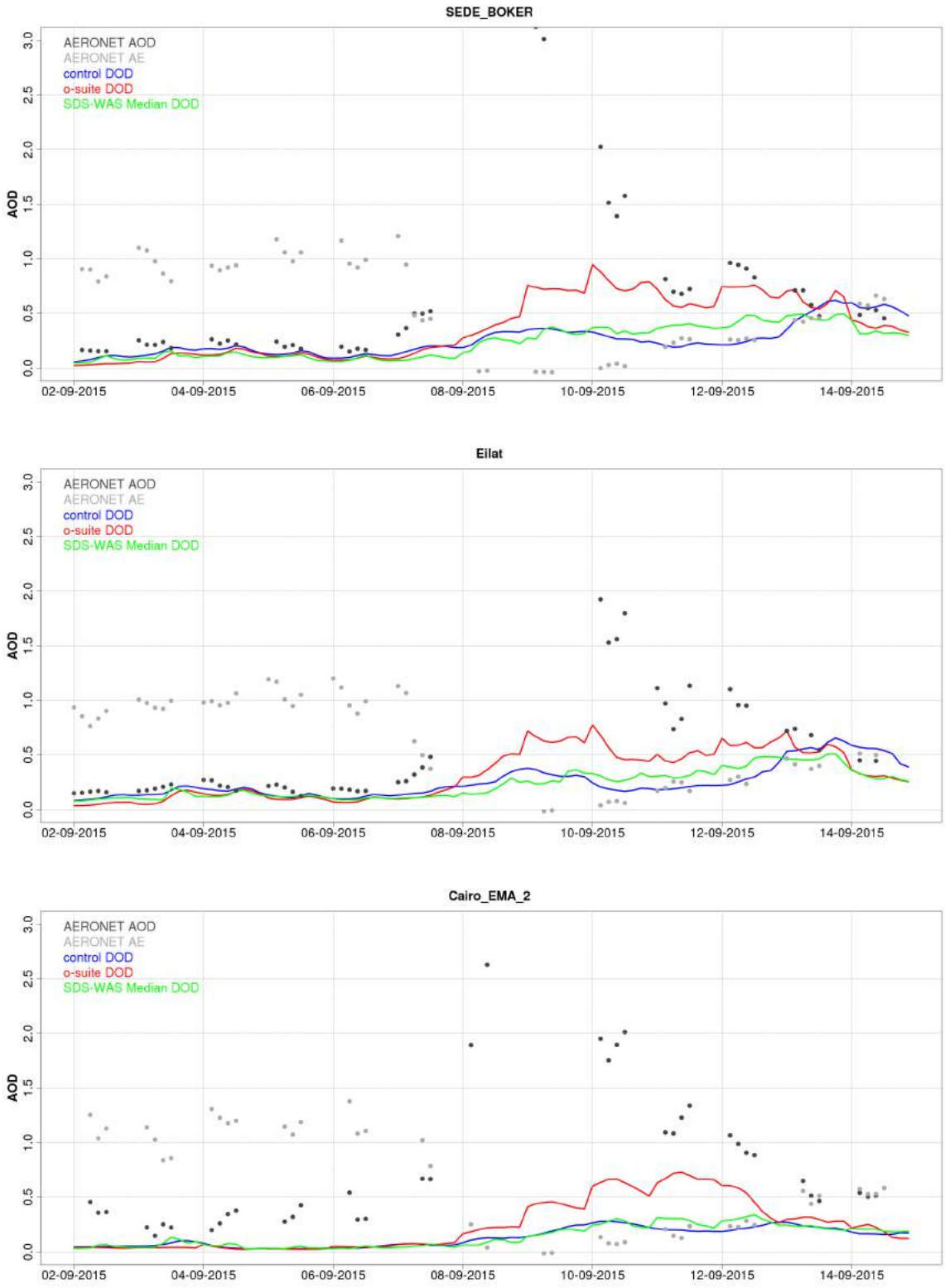


Figure 3.12.2. AOD at 550 nm (black) and Angstrom exponent (grey) from AERONET, DOD at 550 nm from o-suite (red), DOD at 550 nm from control (blue) and DOD at 550 nm from SDS-WAS Multi-model Median (green) at Sede Boker and Eliat (Israel), and Cairo EMA (Egypt) AERONET sites from 2nd to 15th September 2015.

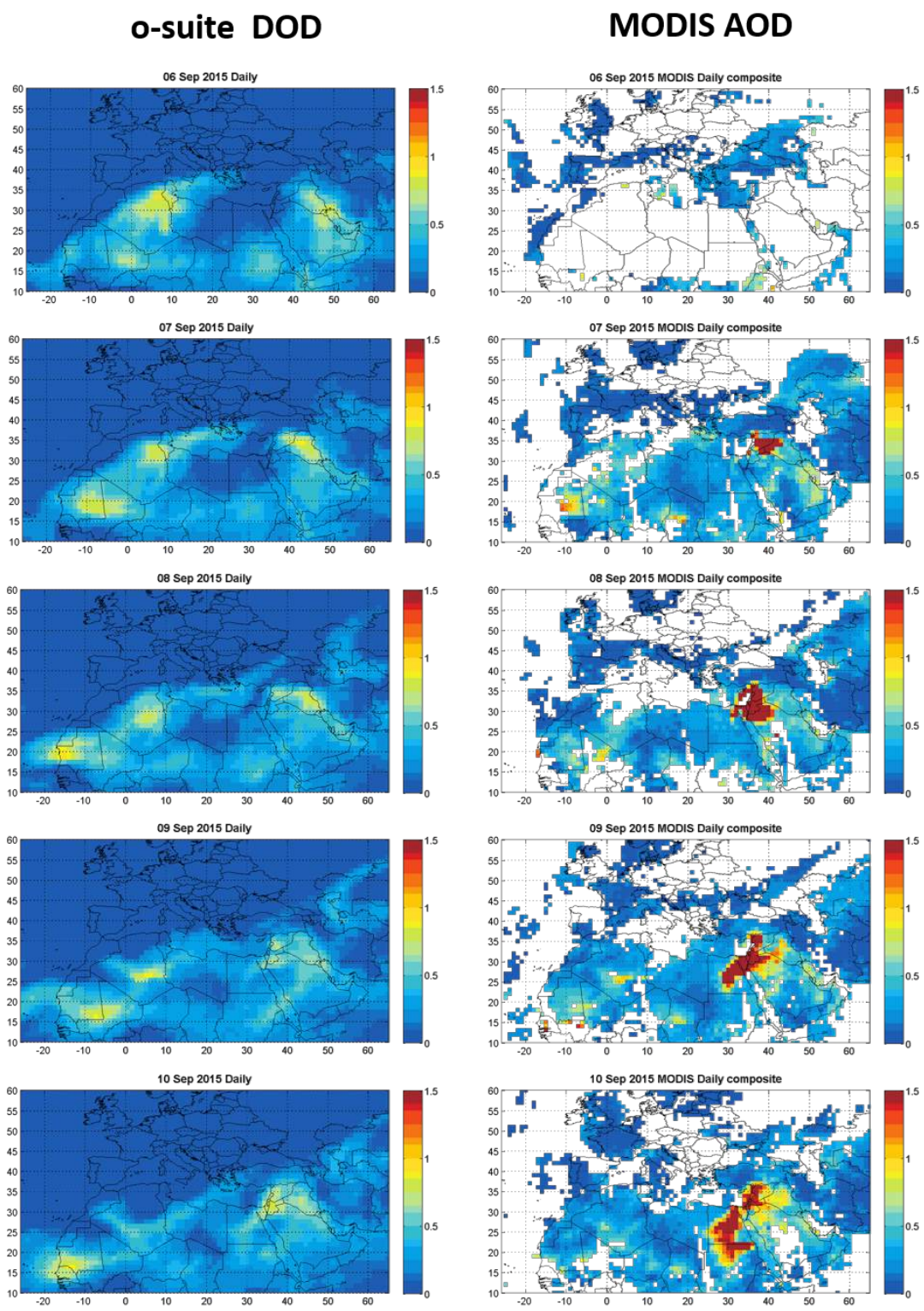


Figure 3.12.3. Daily DOD from o-suite (left column) and daily AOD from MODIS composite of dark target and Deep Blue products (right column) for October 6th-10th, 2015. White areas indicate no data.

# 4 Greenhouse gas events

## 4.1 Synoptic event observed at Amsterdam Island, June 2016

*Taken from the SON-2016 NRT validation report [nrt2017d].*

Figure 4.1.1 shows an example of a synoptic event at Amsterdam Island which occurred in June 2016. During this season we observed sometimes an increase of the observed trace gases, like Radon, $CO_2$, $CH_4$, CO, black carbon. Such events cannot be explained by local emissions and are due to a rapid advection (2-3 days) of pollutants from southern Africa (Figure 4.1.2). This example demonstrates the capacity of the model to simulate this transport over the Indian Ocean, since both the amplitude and timing of the $CH_4$ spike is perfectly reproduced. For $CO_2$, the model underestimates the increase of concentrations and fails to reproduce the daily variation, indicating that the biospheric surface flux should be improved.

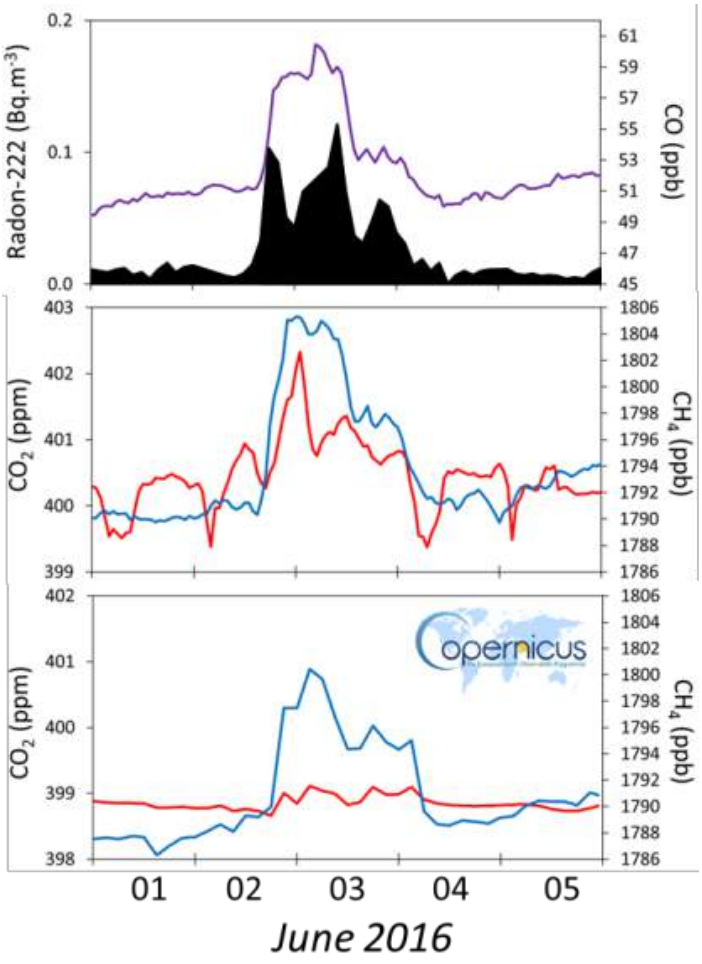


Figure 4.1.1: Short term variabilities of trace gases at Amsterdam Island during a radonic storm (01-05 June 2016) originating from Southern Africa. The above figure shows mole fractions of Radon-222 (black) and CO (purple. The middle figure shows mole fractions of $CO_2$ (red) and $CH_4$ (blue). The bottom figure shows simulations of $CO_2$ (red) and $CH_4$ (blue).

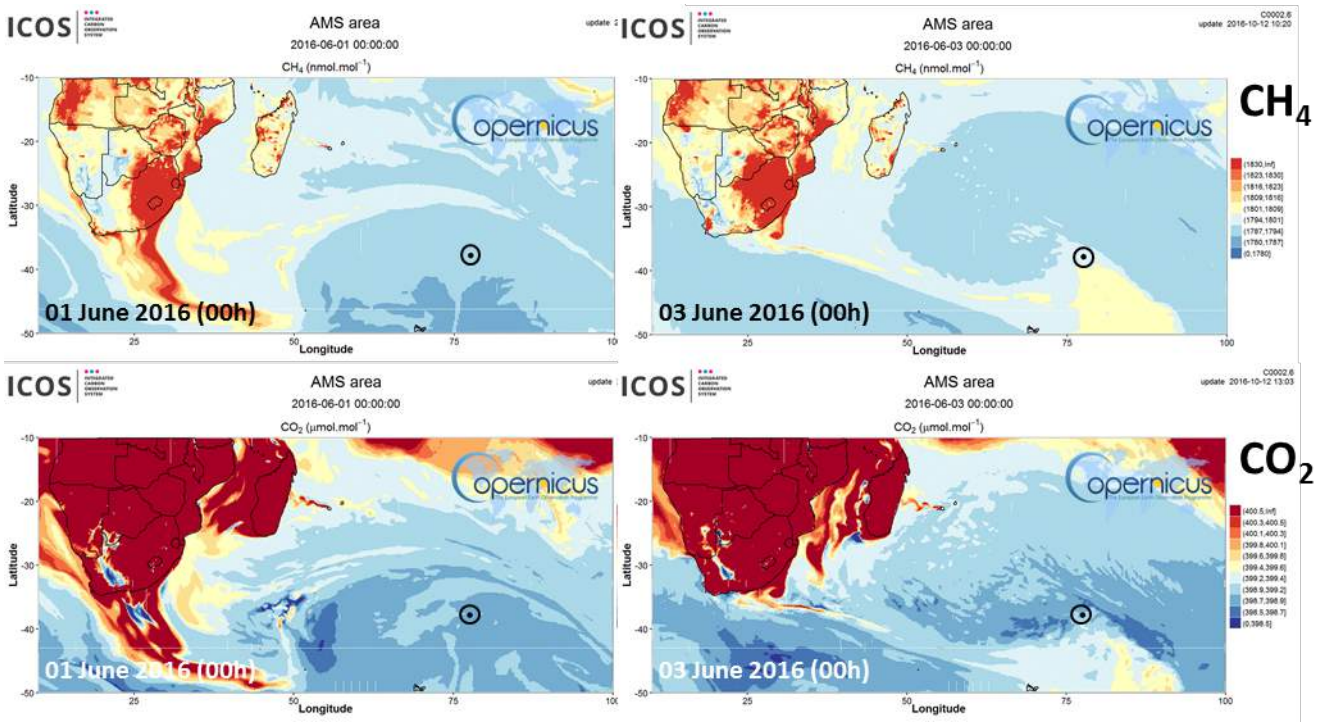


Figure 4.1.2: Simulated distribution of $CH_4$ (above) above and $CO_2$ (below) mole fractions at the surface level on 1st (left) and 3rd (right) June 2016. The black circle indicates the position of Amsterdam Island.

# 5 Ozone layer

## 5.1 Ozone depletion above the Arctic and Northern Europe, Jan-Feb. 2016

*Taken from the DJF-2016 NRT validation report [nrt2016c].*

An ozone depletion event developed over the Arctic during December 2015 - February 2016 and reached Northern Europe in February. The meteorological conditions leading to this event are described by Braathen (2016). Figure 5.1.1 is copied from this WMO report. It shows, for four dates in the first half of the considered period and on the 40.5 hPa isobaric level, the BASCOE analyses of $HNO_3$, HCl and $ClO+2Cl_2O_2$ , based on Aura-MLS observations.

Figure 5.1.2 shows the corresponding ozone analyses by the CAMS o-suite, at the same level as well as in total column. The o-suite analyses show lowered ozone abundances in the Arctic polar vortex in January. Due to the weaker winter polar vortex in the Northern Hemisphere, there are important differences between ozone depletion episodes in the Arctic and in the Antarctic (Solomon et al., 2014). Yet the lower ozone abundance is due to the same processes in both cases: dynamical (downdraft and isolation of ozone-poor air masses in the vortex) and chemical (i.e. catalytic destruction of ozone by chlorine once the vortex is exposed to sunlight and $Cl_2O_2$ is photolyzed into ClO).

The quantitative attribution of ozone depletion to each process requires satellite observations of ozone chlorine compounds and dedicated model runs (see e.g. Strahan et al., 2013; Hommel et al., 2014). Here we address two more basic questions:

- How well do the o-suite analyses of ozone represent the event observed in January and February 2016?
- Did this event reach European stations in the middle northern latitudes and can the o-suite analyses be used in such an assessment?

Figure 5.1.3 shows eight individual balloon soundings above Ny-Alesund, which is one of the northernmost stations used in this report (79°N). These soundings, which were also used for the averaged Arctic profiles shown in fig. 3.6.2, show that the abundance and vertical distribution provided by the CAMS o-suite agree very well with the ozone soundings. The only disagreements are ozone overestimations by the o-suite in the upper part (10-60 hPa) of the first sounding shown (2016/01/20) and in the lowermost stratosphere (~130 hPa) in the three last soundings (2016/02/10, 2016/02/13, 2016/02/21).

This underestimation of ozone depletion in the leftmost plot of Figure 5.1.3 (2016/01/20, 10-60 hPa) is confirmed by the time series of profiles retrieved from the ground-based Microwave Radiometer (MWR) at the same station, with positive biases reaching ~1 ppmv (Figure 5.1.4) i.e. 30 to 40% in the height range 25-30 km (see figure 3.6.3).

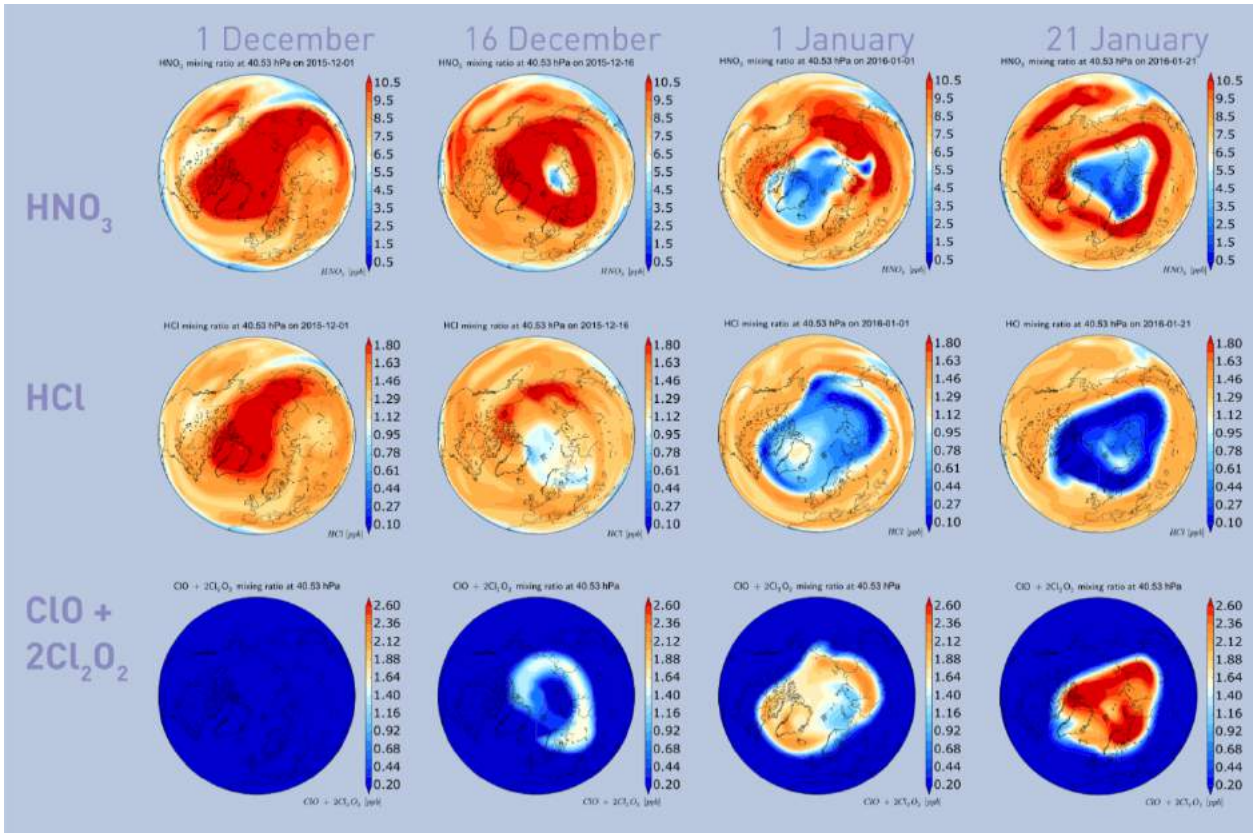


Figure 5.1.1: Results from BASCOE at the level of 40.5 hPa. The upper row shows the mixing ratio of nitric acid, the second row shows the mixing ratio of hydrochloric acid, and the third row shows the sum of chlorine monoxide and its dimer ($ClO + 2Cl_2O_2$). All three rows show the temporal development from 1 December to 21 January with intermediate frames shown for 16 December and 1 January. Copied from figure 8 in Braathen (2016).

During the first days of February, Arctic air masses with depleted ozone and enhanced amounts of chlorine oxides reached as far south as the NDACC station of Bern (47°N). Figure 5.1.5 shows that the agreement between the o-suite and MWR observations is excellent, including during the ozone depletion episode which is clearly associated with elevated chlorine amounts in the BASCOE analyses.

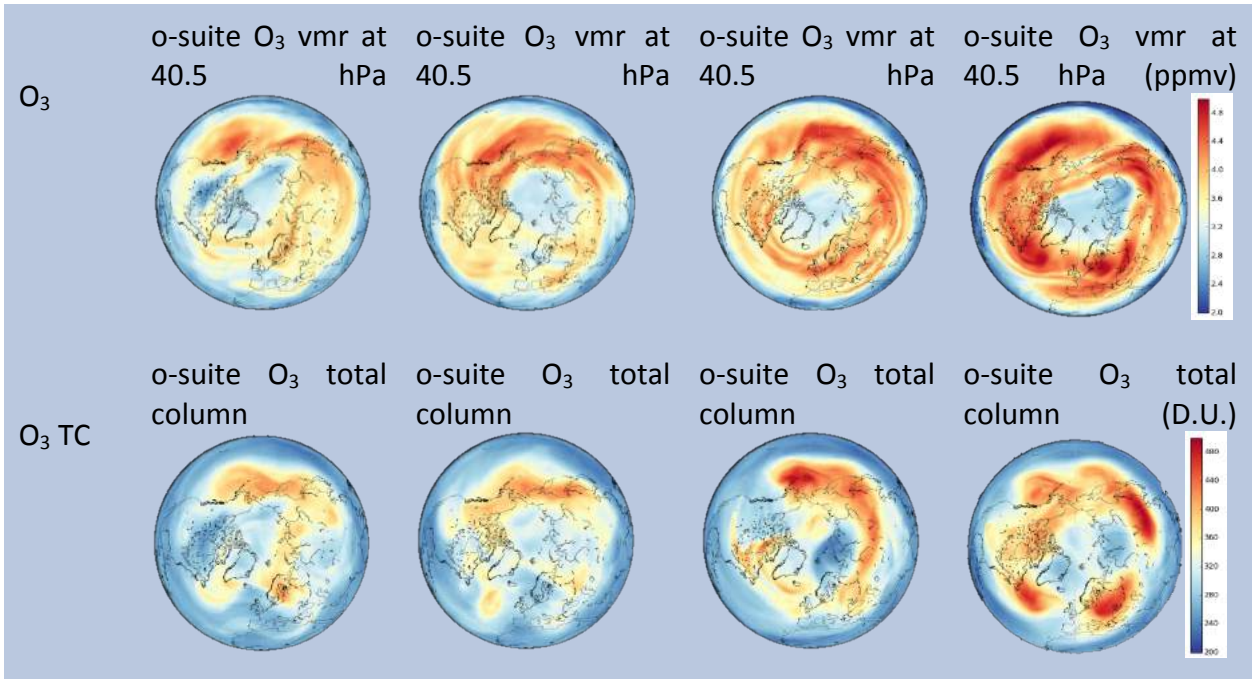


Figure 5.1.2: Results from the CAMS o-suite, on the same dates as the previous figure. The upper row shows the analyses of ozone mixing ratio at 40.5 hPa and the lower row shows the total column of ozone.

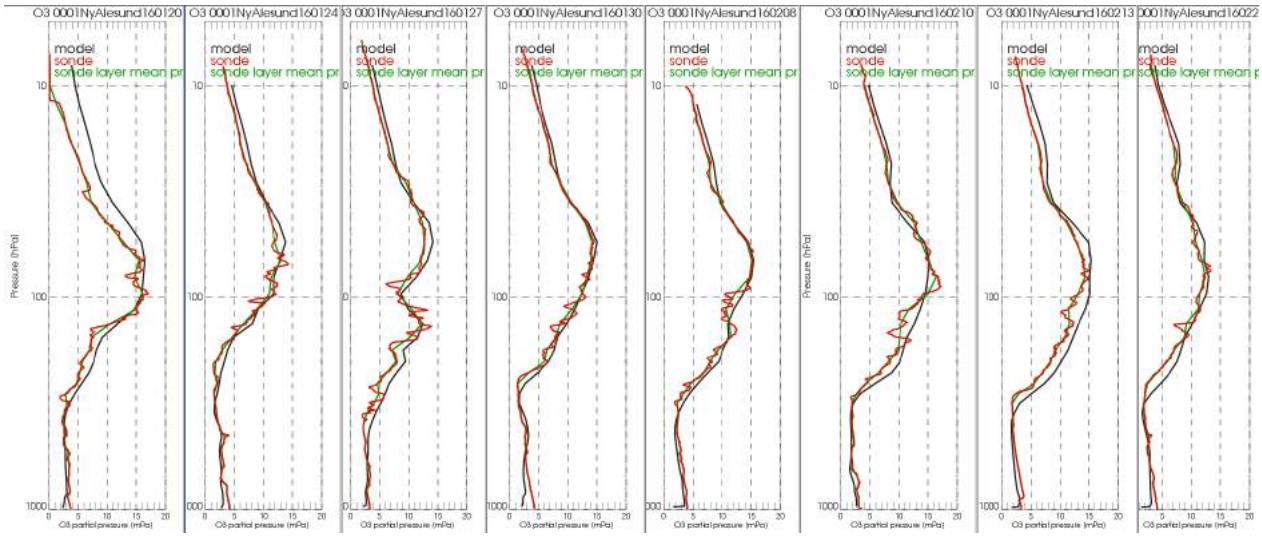


Figure 5.1.3: Eight individual ozone soundings above Ny-Alesund from 2016/01/20 until 2016/02/21. Note the non-standard color scheme: black lines, o-suite analyses; red lines, sonde observations; green lines, sonde observations smoothed to allow quantitative comparison with the o-suite.

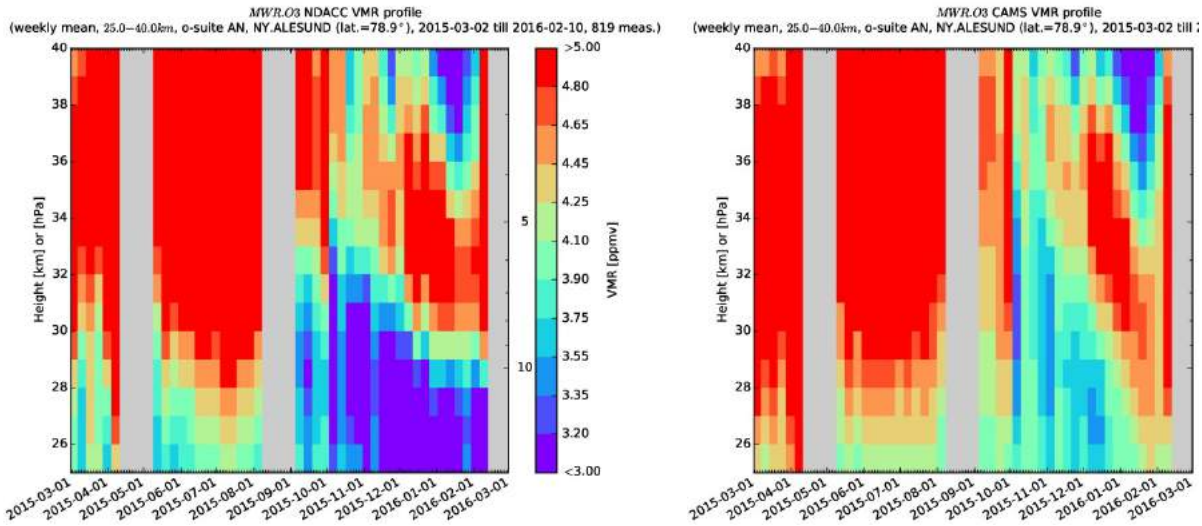


Figure 5.1.4: Ozone volume mixing ratio above Ny-Alesund as a function of time and height: NDACC MWR observations (left) versus o-suite analyses (right)

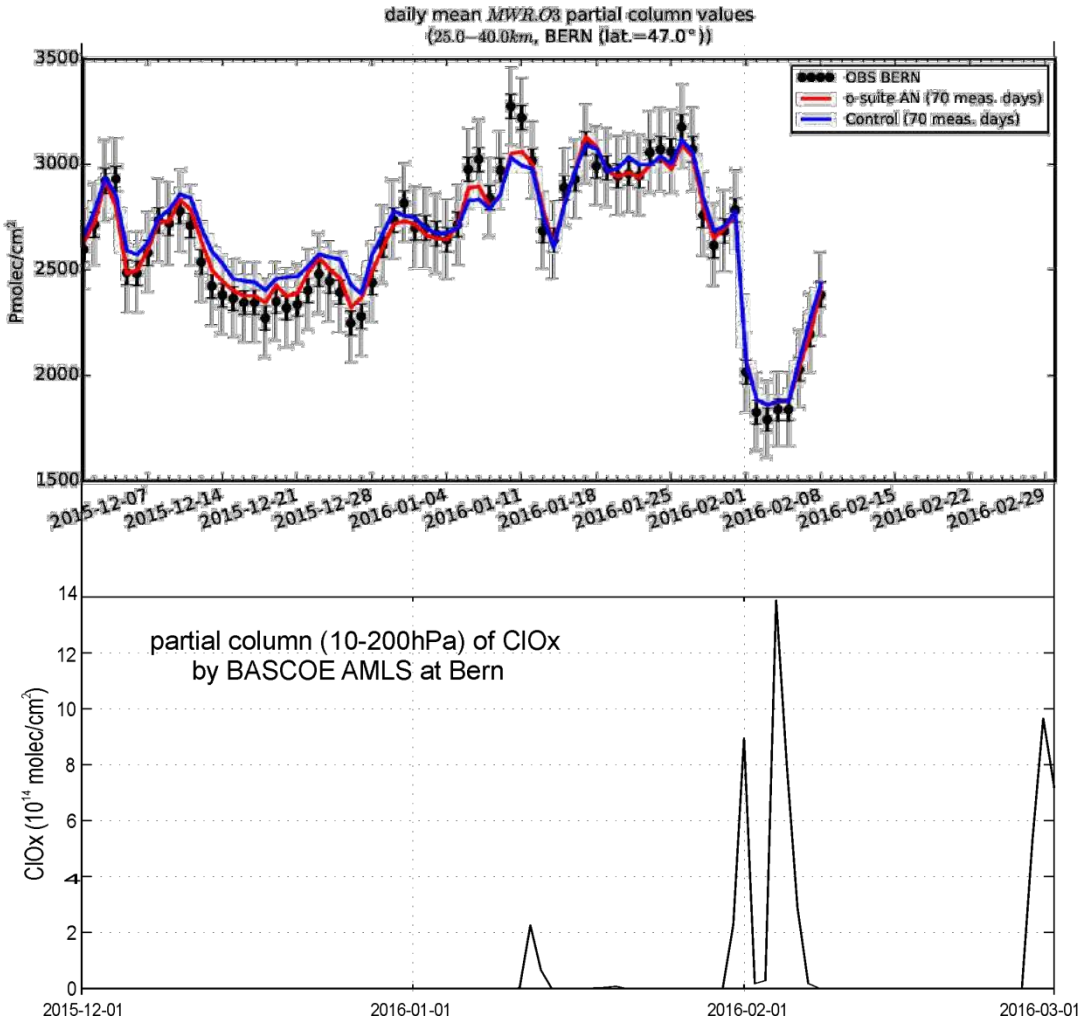

Figure 5.1.5: Time series) above Bern (Switzerland) of the ozone partial column (25-40km; red line shows o-suite analyses, symbols show the MWR observations) and of $ClO+2*Cl_2O_2$ partial column (10-200 hPa; BASCOE analyses of Aura-MLS observations of ClO).

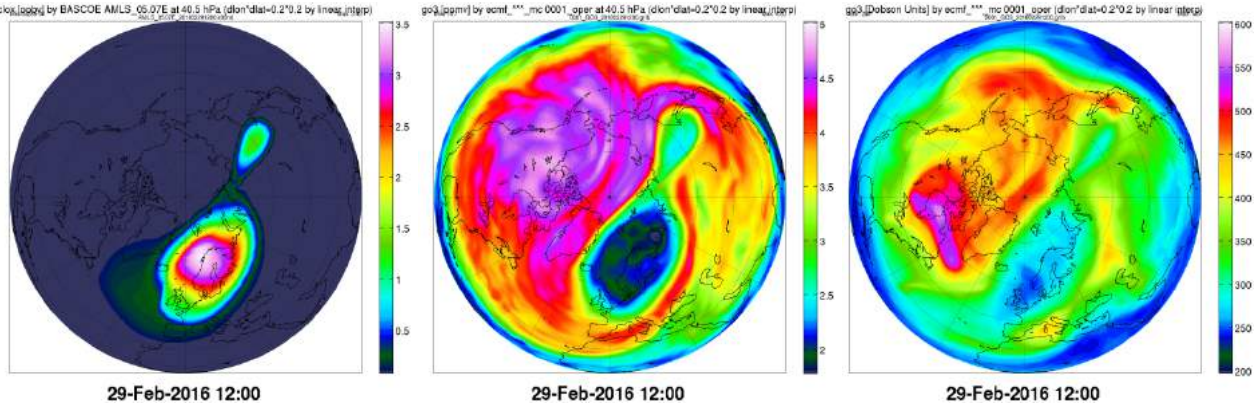


Figure 5.1.6: BASCOE analysis of $ClO_X$ at 40.5 hPa (left), CAMS o-suite analysis of ozone at 40.5 hPa (middle) and CAMS o-suite analysis of ozone total column (right), on 29 February 2016. The ozone depletion event clearly covers Northern Europe.

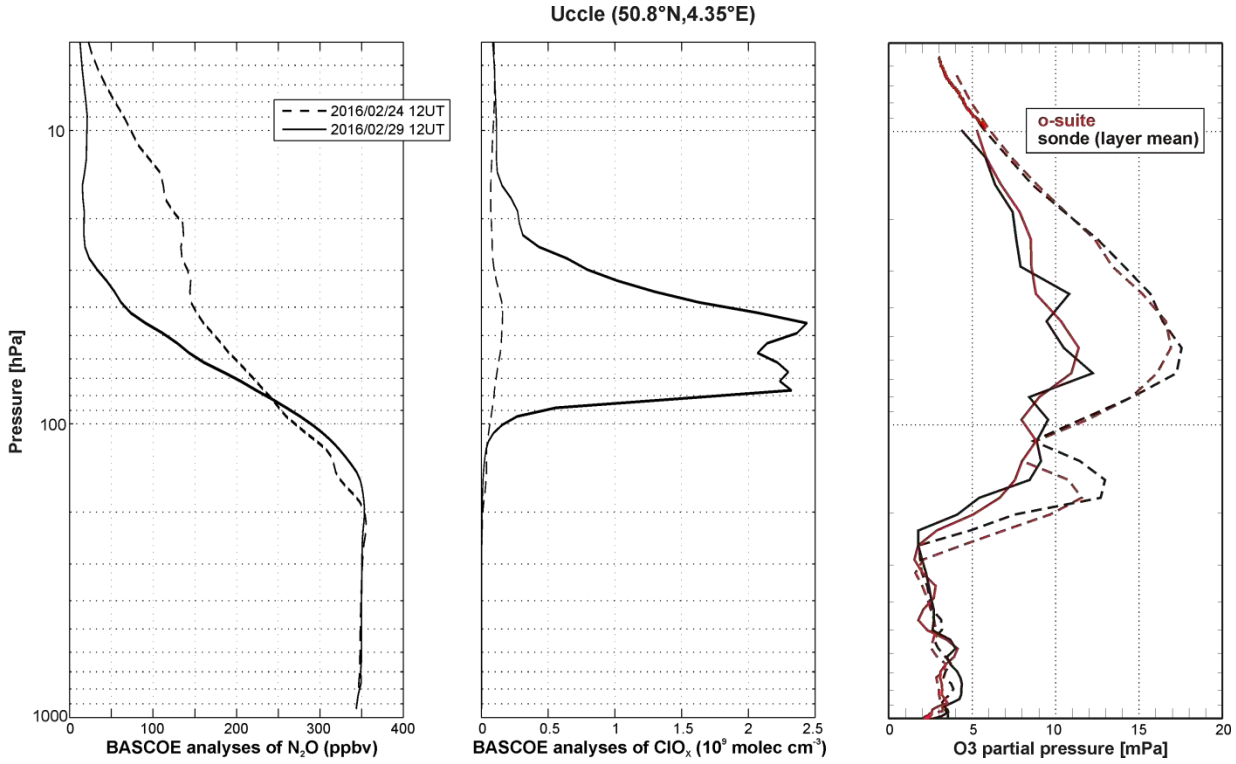


Figure 5.1.7: Vertical profiles above Uccle on 2016/02/24 (dashed lines) and 2016/02/29 (solid lines): BASCOE analyses of $N_2O$ (left plot) and $ClO_X$ (middle plot); ozone partial pressure (right plot) in the o-suite analyses (red lines) and as observed by ozonesondes (black lines)

On 29 February 2016, the last day studied in this report, the Arctic vortex reached the European mid-latitudes again, which could be seen even on a map of total column ozone (Figure 5.1.6). An ozone sonde was launched from Uccle on that day. It shows significantly lower values than 5 days earlier, both profiles agreeing very well with the corresponding o-suite analyses (Figure 5.1.7). The correlation with vortex air masses can be verified with the BASCOE analyses of the tracer $N_2O$ and of active chlorine $ClO_X$ which are shown on the same figure.

To summarize, during this depletion episode the o-suite analyses overestimated stratospheric ozone above Ny-Alesund as observed by ozone sondes and Microwave Radiometers but according to ozone sondes this disagreement became much less severe after 20 January. The comparison with OMPS-LP in the Arctic latitude band (Figure 3.6.5) confirms this assessment with a bias varying quickly, from 10% until 1 February to 2-6% afterwards. Above the Northern European stations of Bern and Uccle the biases were much smaller - even when the polar vortex reached these latitudes. From a seasonally averaged point of view (DJF 2015-2016), the relative bias between MWR instruments and the o-suite reached 14.5% above Ny-Alesund but only 0.7% above Bern.

# 6 CAMS-regional case studies

## 6.1 African dust, March-April 2018

*This work has not been published elsewhere.*

During March and April 2018 several African dust transport events occurred over the Mediterranean region. Of particular interest is the dust transport event over Crete (Greece) on 22 March 2018, which resulted in a record-breaking observation of **PM10 concentrations of 6340 μg/m$^3$ at the Finokalia ground-based station** (Solomos et al., 2018). Figure 6.1.1 presents the prevailing synoptic conditions (mslp; blue contours, vertical velocity at 850 hPa; color shaded, wind arrows at 850 hPa) and dust mass mixing ratios at 850 hPa during the period from 06Z 21 March 2018 to 00Z 23 March 2018. A low-pressure system is seen over the Gulf of Sirte at 18Z 21 March 2018 initiating the southerly flow towards the island of Crete, while the ascending motion on the east side of the cyclone resulted in the dust uplift into the lower troposphere. The regional ensemble and its individual members are found capable of reproducing the enhanced PM10 concentrations in the lower troposphere (1000m) as it is depicted from Figure 6.1.2.

Finally, the enhanced PM10 concentrations observed at Thessaloniki (Greece) in the urban background station of Malakopi, during March 2018, are investigated with the aid of CAMS-global and regional modeling systems. The time series of the observed PM10 concentrations at Thessaloniki exhibit several peaks, which are mainly attributed to dust outbreaks, as the CAMS-global PM10 and dust time series suggest. The regional ensemble is closer to PM10 observations, and in general captures the observed peaks with a relatively good temporal correlation (~ 0.5 derived from hourly values). The CAMS-global underestimates the urban background levels of the station and the amplitude of PM10 diurnal variability, but represents quite well the air pollution events.

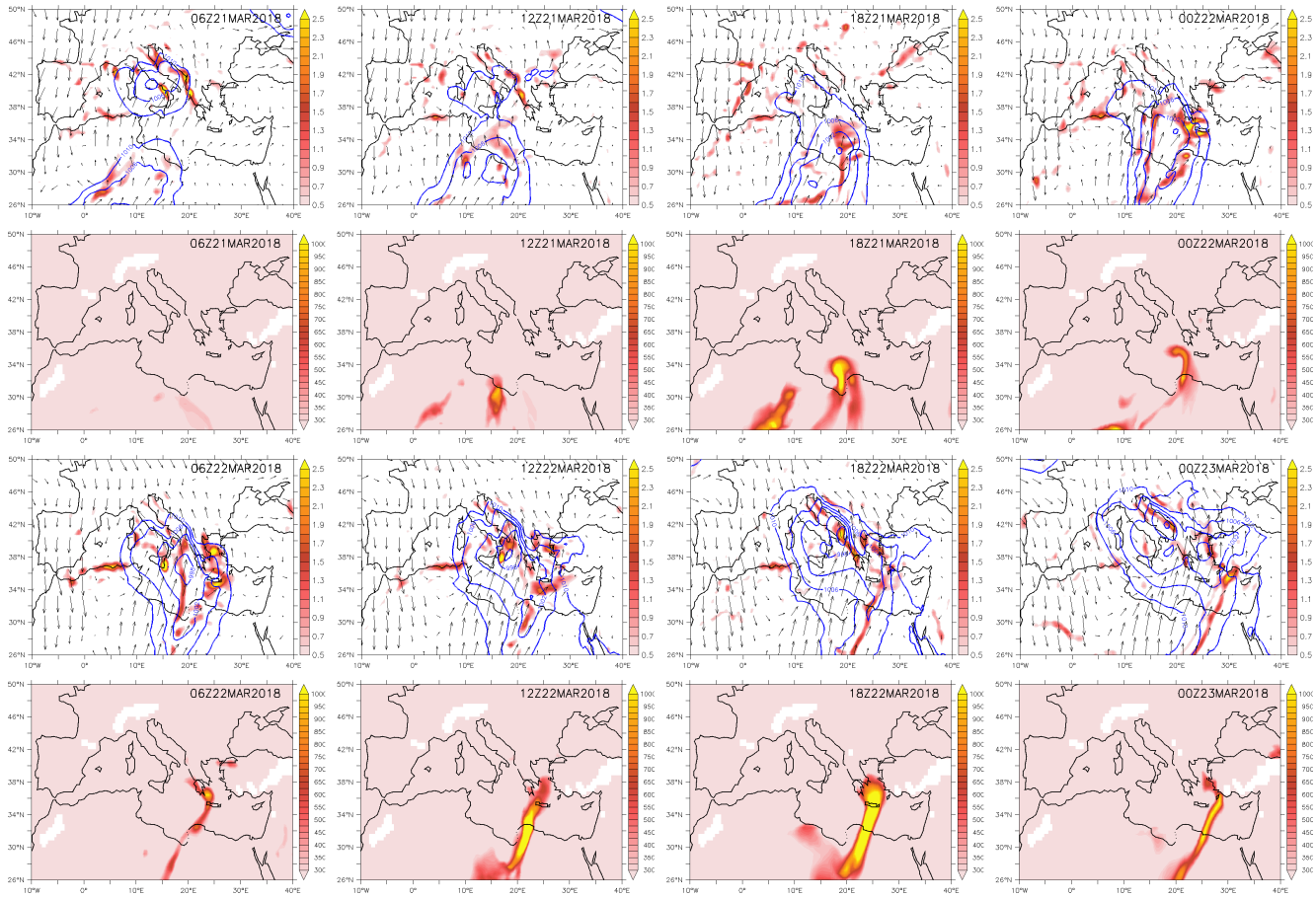


Figure 6.1.1. Rows 1 & 3: MSLP (blue contour; hPa), vertical velocity (color shaded; -Pa/s) and wind arrows at 850 hPa for the time period from 06Z 21 March 2018 to 00Z 23 March 2018. Rows 2 & 4: Dust mass mixing ratio (color shaded; g/kg) at 850 hPa for the time period from 06Z 21 March 2018 to 00Z 23 March 2018.

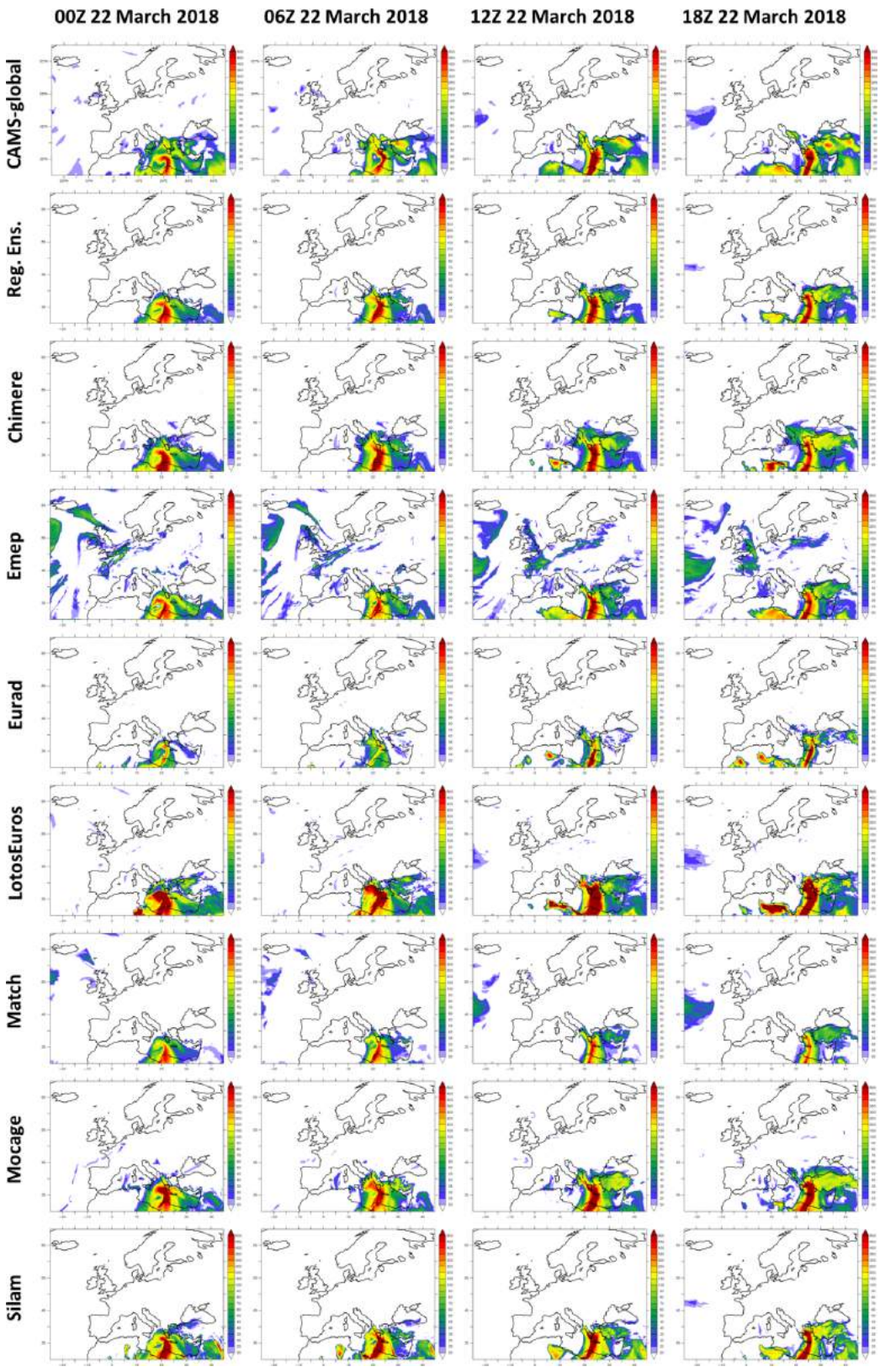


Figure 6.1.2. PM10 mixing ratio at 1000m for CAMS-global, regional ensemble and the seven ensemble members.

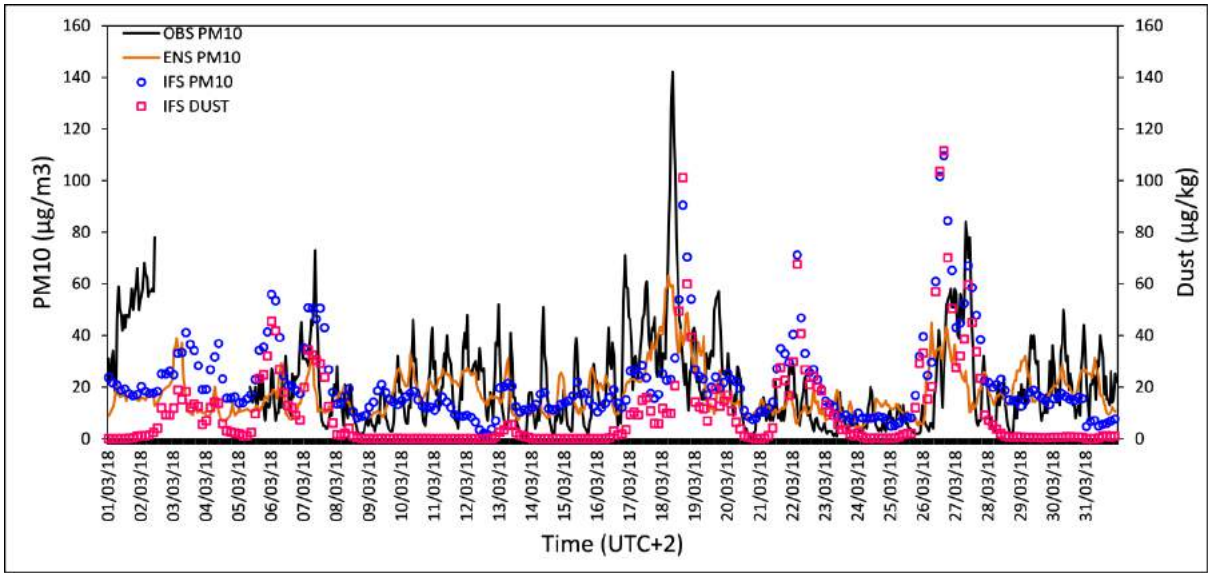


Figure 6.1.3. March 2018 time series of observed (black line, hourly) PM10 mixing ratio, CAMS-global (blue circles, 3-hourly) and regional ensemble (orange line, hourly) PM10 mixing ratio, and CAMS-global (pink squares, 3-hourly) dust mass mixing ratio at Thessaloniki (Malakopi station), Greece.

## 6.2 African dust and Iberian smoke, October 2017

*Taken from the SON-2017 CAMS-regional validation report [reg2018a].*

In response to the red sky reported over several parts of the UK on 16 October 2017, the transport of African dust and Iberian smoke, related to the passage of the Ophelia hurricane, in the CAMS-global and regional models is explored. The prevailing synoptic conditions for the time period 00Z 13 Oct 2017 to 18Z 18 Jan 2017 are presented in Figure 6.2.1 for CAMS-global, depicting the formation/evolution of Ophelia with the aid of MSL-pressure and wind speed/direction fields.

As the system moved northward from the Azores towards the UK (Figure 6.2.1), African dust was dragged and picked up in the troposphere over the UK (06Z 16 October 2017) as can been seen in both CAMS global and regional ensemble PM10 fields at 2000m (Figure 6.2.2). Both systems reproduce the transport of PM10 along the west European coasts, however CAMS-global shows higher PM10 than the ENSEMBLE.

In order to decompose the contribution of African dust and Iberian biomass burning in PM10 loadings dust, CO, $NO_x$, $SO_2$, $C_2H_6$, organic matter and black carbon fields at 800 hPa are presented in Figure 6.2.3, indicating that smoke from the fires in Portugal and Spain is lifted up in the troposphere and passes over the UK from 06Z 16 October 2017 onwards through the southeast part of Ophelia cyclone. The above mentioned condition is also confirmed by the latitude-pressure cross sections at $0^o$ E of CAMS-global dust, CO, organic matter and black carbon (Figure 6.2.4), depicting high dust loadings over London up to 600 hPa at 06Z 16 October 2017, while onwards rising plumes of smoke products are gradually seen up to the upper troposphere at 06Z and 18Z 17 October 2017.

Figure 6.2.1. CAMS-global mean sea-level pressure (in hPa; contours), wind speed (in m/s; color shaded) and wind direction (vectors) at 1000 hPa, during the period 00Z 13 Oct 2017 to 18Z 18 Jan 2017 (6 hours interval).

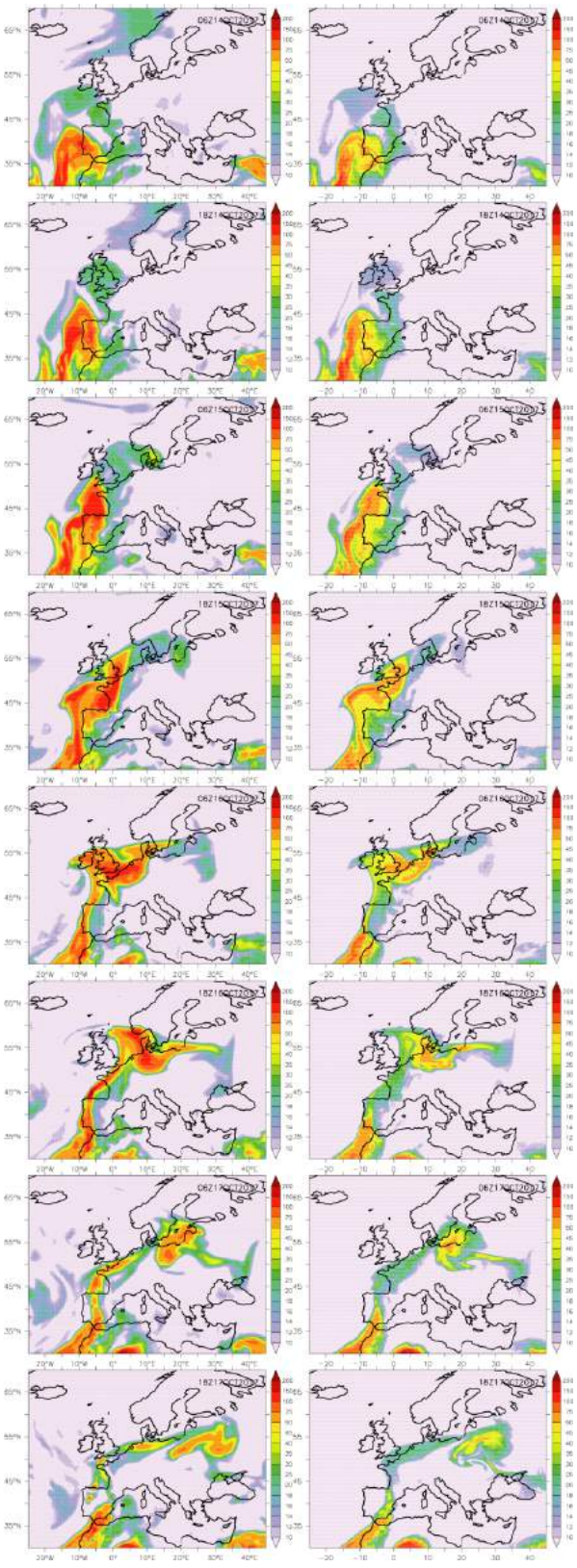

Figure 6.2.2. CAMS-global (left) and regional ENSEMBLE (right) PM10 concentrations (ug/$m^3$) at 2000m over the time period 06Z 14 Oct 2017 to 18Z 17 Oct 2017 (12 hour interval).

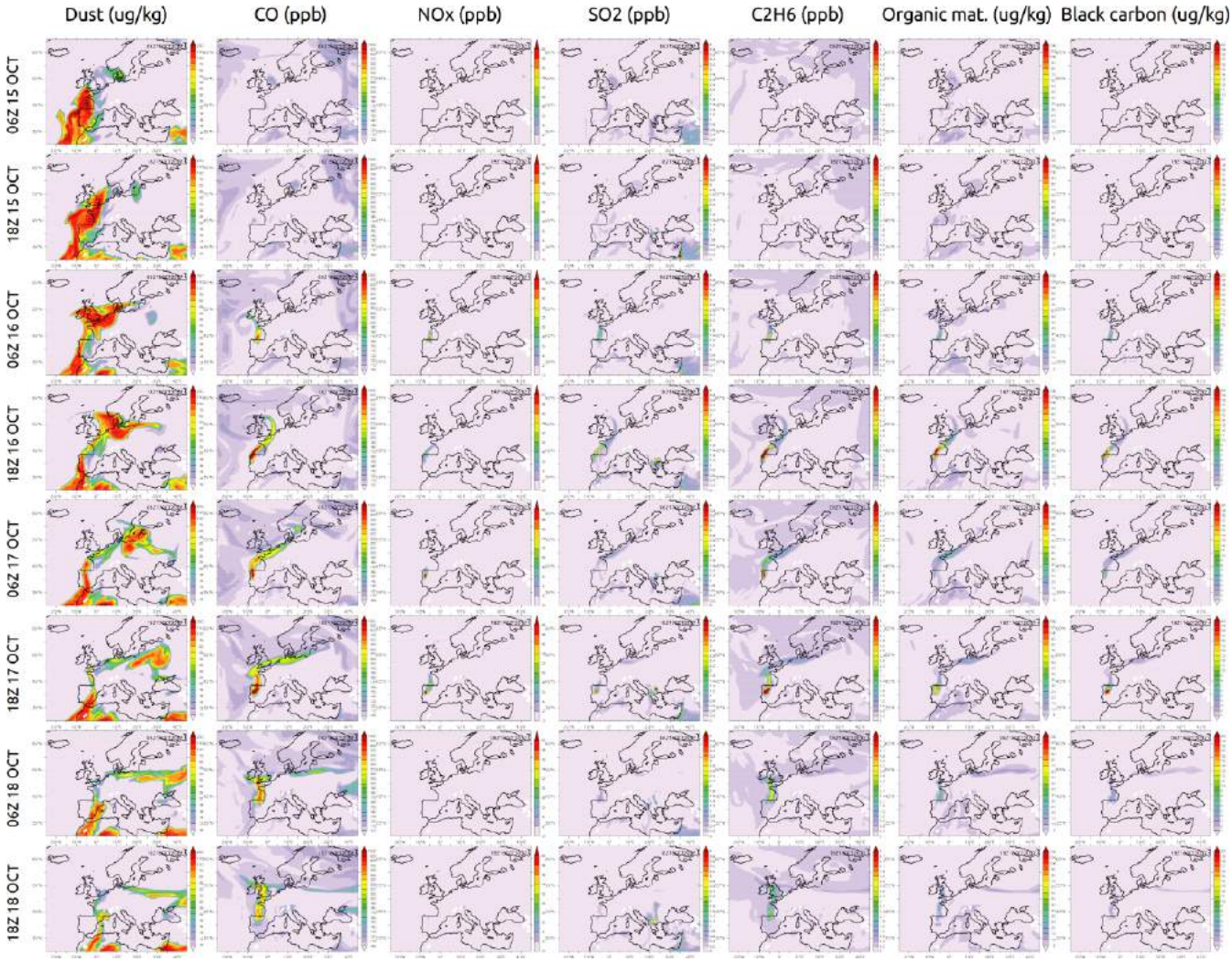


Figure 6.2.3. CAMS-global dust (ug/kg), CO (ppb), NOx (ppb), $SO_2$ (ppb), C2H6 (ppb), organic matter (ug/kg) and black carbon (ug/kg) fields at 800 hPa over the time period 06Z 15 Oct 2017 to 18Z 18 Oct 2017 (12 hour interval).

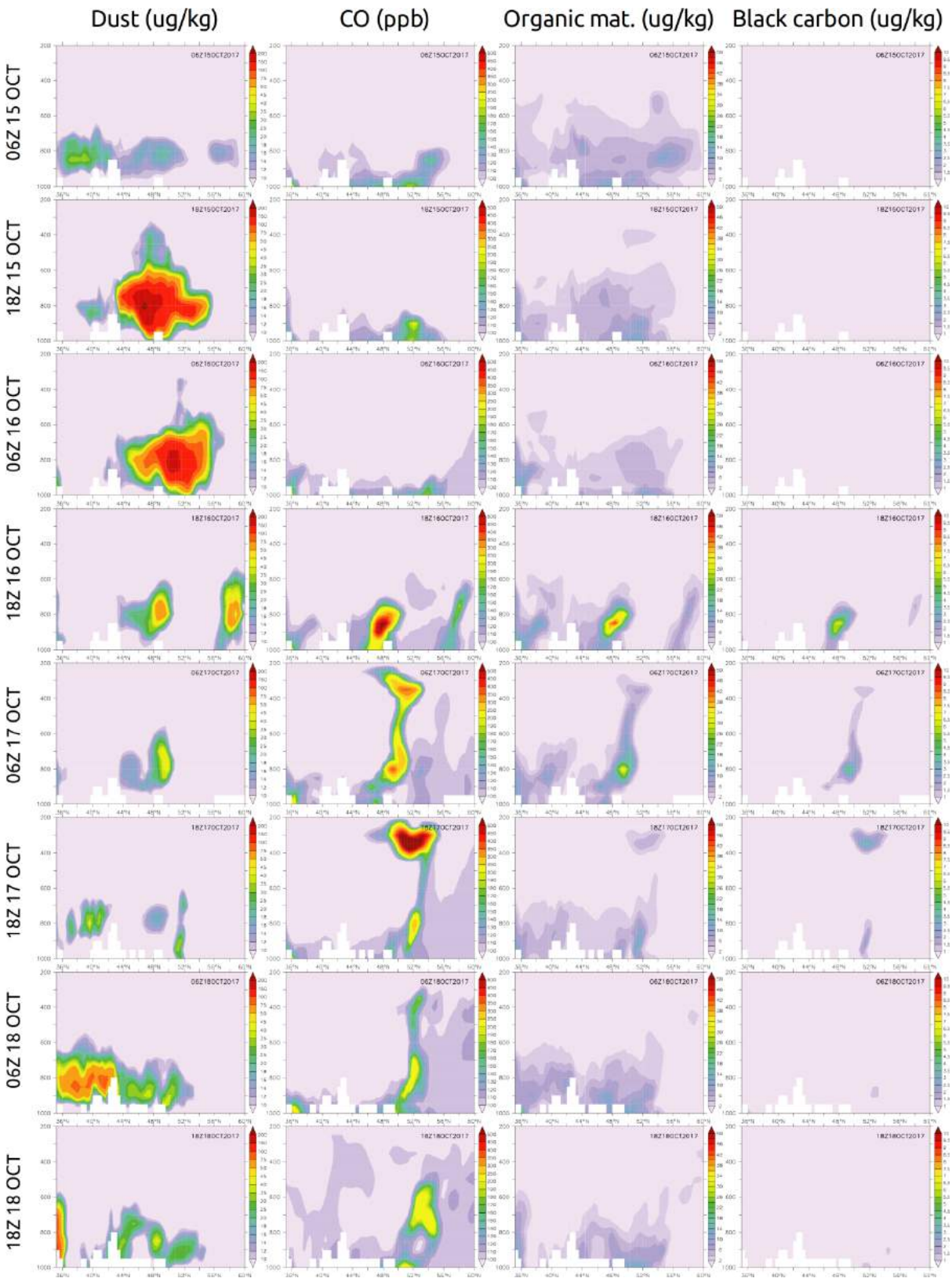


Figure 6.2.4. Latitude-pressure cross sections at 0$^{o}$ E of CAMS-global dust (ug/kg), CO (ppb), organic matter (ug/kg) and black carbon (ug/kg) over the period 06Z 15 Oct 2017 to 18Z 18 Oct 2017 (12 hour interval).

## 6.3 Athens heatwave, June-July 2017

*This work has not been published elsewhere.*

Athens (Greece) experienced a heatwave during the last week of June and early July 2017 with surface temperatures reaching 45$^{o}$C. These extremely warm conditions resulted in enhanced ozone concentrations with numerous exceedances of the public notification threshold (180 μg/m$^{3}$) set by the Hellenic Ministry of Environment, Energy and Climate Change.

In Figures 6.3.1 to 6.3.3 we present the timeseries of ground-based observations (black), CAMS-global (red) and regional ensemble (blue) for $O_3$, NO and $NO_2$ concentrations respectively, for the time period 20/06/2017-04/07/2017. The observed data were provided by the Hellenic Ministry of Environment, Energy and Climate Change[1]. The observational stations are characterized according to their type (urban/suburban; traffic/industrial/background).

Observed NO/$O_3$ is higher/lower in the **urban traffic** stations compared to all other types of stations, because of the high NO traffic emission resulting in higher $O_3$ removal rates. NO is severely underestimated by both global and regional forecast systems, a fact which partly related to the coarser model resolution of the regional and global modeling systems and the modelled strength of sources. Ozone over the same type of stations is nicely temporally correlated with observations, generally following the day-to-day variations.

NO and $O_3$ observations agree well with the forecasts over the **suburban background** stations, however CAMS-global occasionally underestimates nighttime surface $O_3$ (Thrakomakedones), while ENS captures well its diurnal variability range.

Observed $NO_2$ is on average underestimated in all types of stations by the regional ensemble. CAMS-global manages to capture the variability and often the magnitude of $NO_2$ variability.

Evaluation of regional/global models over urban stations is not performed usually, as it is generally unfair for the coarse resolution models. In this case, the comparison gives us an idea of the performance of the specific modeling systems, under extreme weather conditions in urban agglomerations, where the population density is the highest. Both models perform reasonably well, taking into consideration the aforementioned constrains, eventually NOx emissions in urban environments could be revisited by the modelers.

[1] There was no quality control on the delivered observational dataset

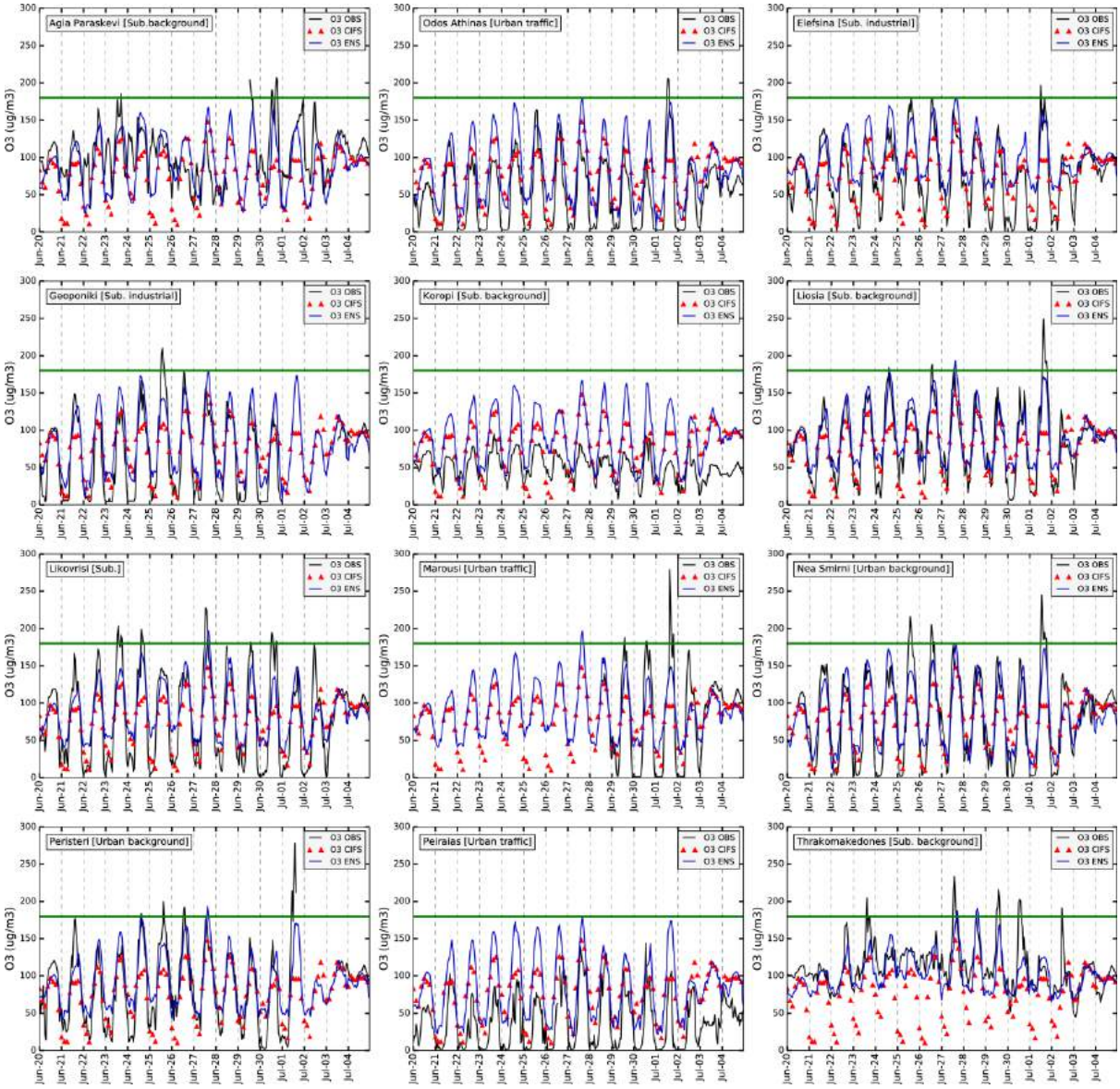


Figure 6.3.1. $O_3$ concentrations (ug/$m^3$) for 12 stations of the greater Athens region for observations (hourly; black line), CAMS-global (3-hourly; red triangles) and regional ensemble (hourly; blue line). The green horizontal line denotes the public notification level of 180 ug/$m^3$ for ozone. Dates are in local time (UTC+3).

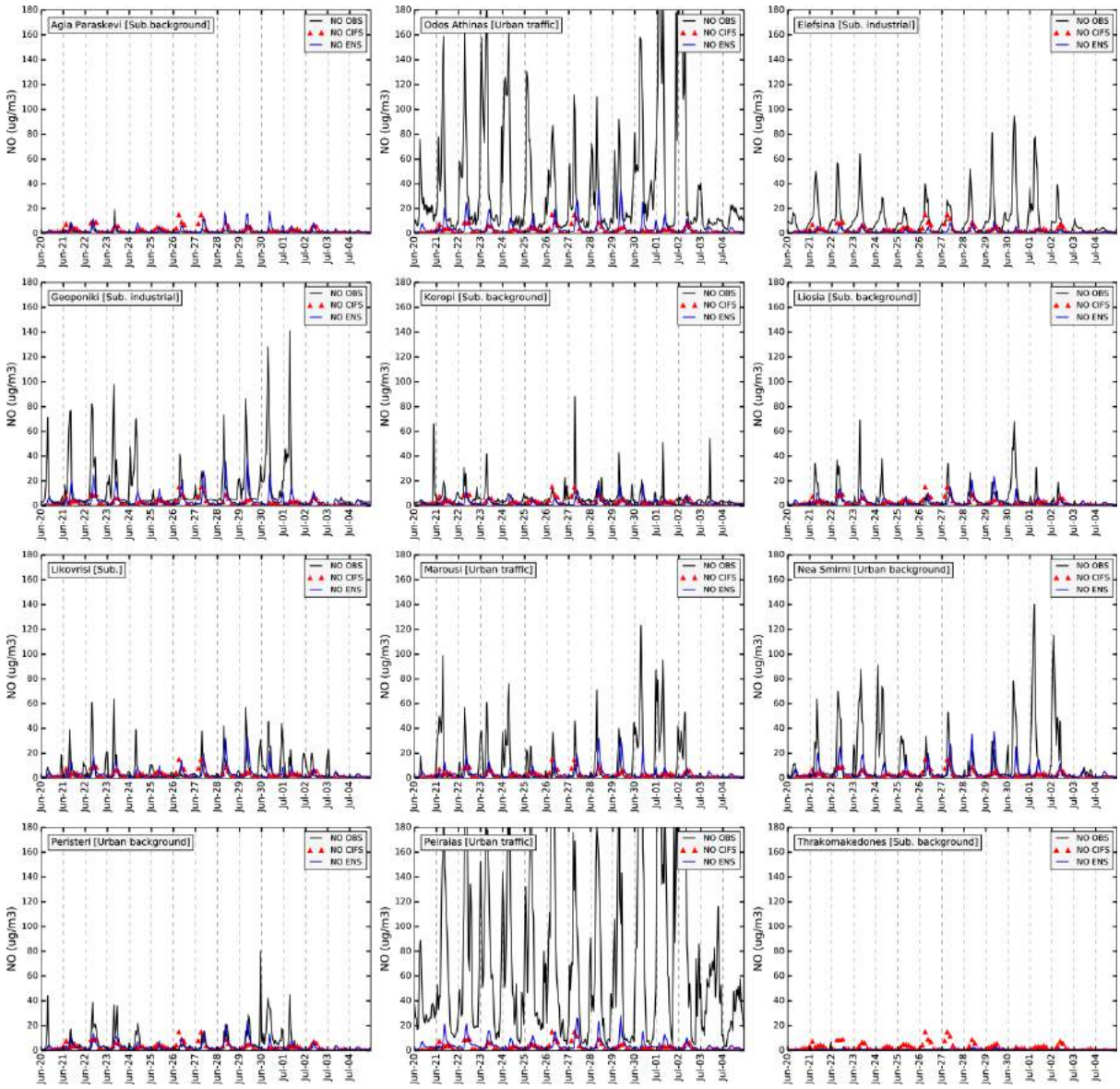


Figure 6.3.2. NO concentrations (ug/m$^3$) for 12 stations of the greater Athens region for observations (hourly; black line), CAMS-global (3-hourly; red triangles) and regional ensemble (hourly; blue line). Dates are in local time (UTC+3).

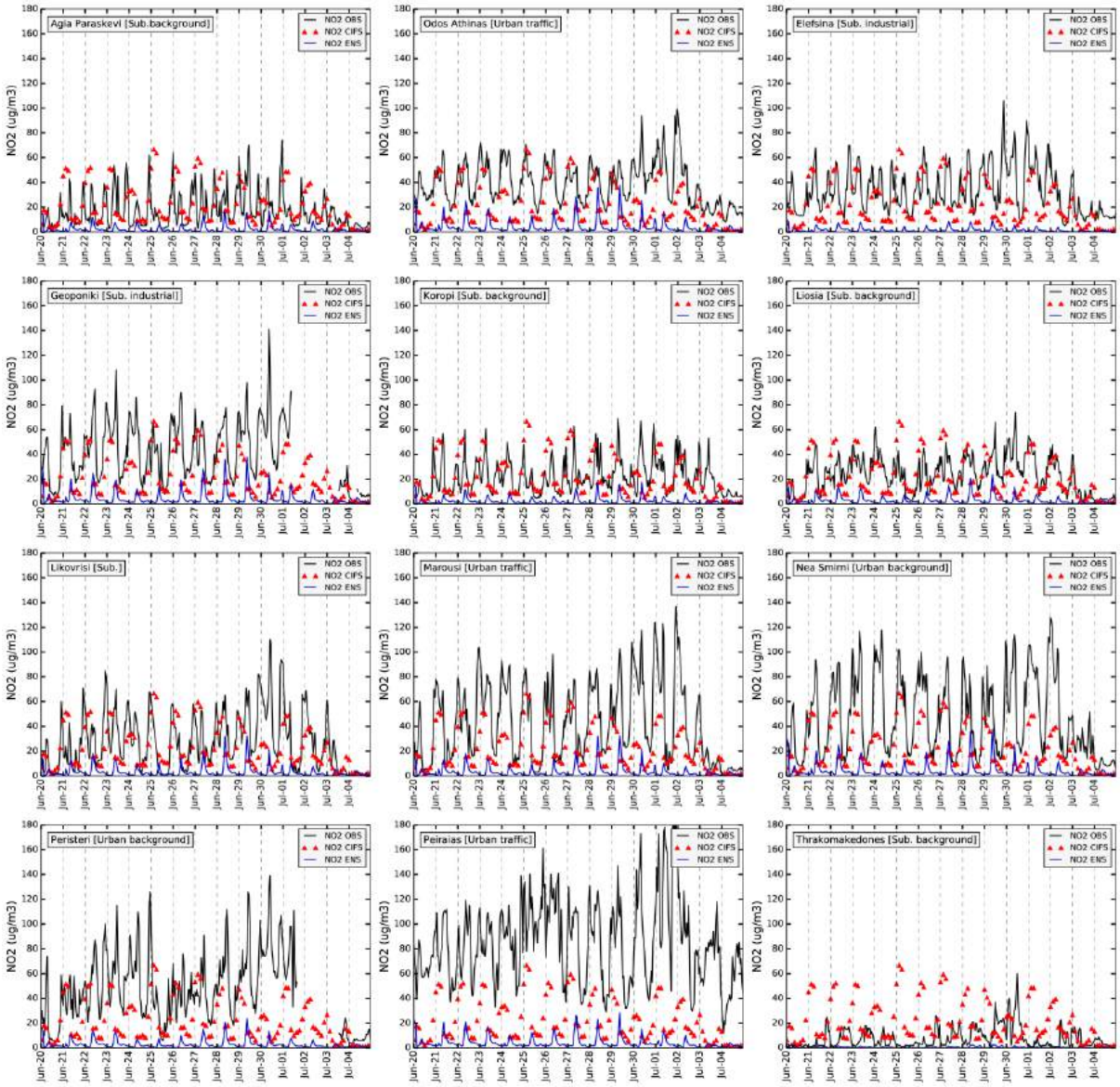


Figure 6.3.3 $NO_2$ concentrations (ug/$m^3$) for 12 stations of the greater Athens region for observations (hourly; black line), CAMS-global (3-hourly; red triangles) and regional ensemble (hourly; blue line). Dates are in local time (UTC+3).

## 6.4 Air pollution episode in January 2017

*This work has not been published elsewhere.*

During the period 20-24 Jan 2017 an air pollution event occurred over north-west and central Europe, associated with a diffluent omega blocking pattern (Fig. 6.4.1). Stagnation of the lower level air led to pollution build-up during this time period, as indicated by the very low wind speeds over central continental Europe.

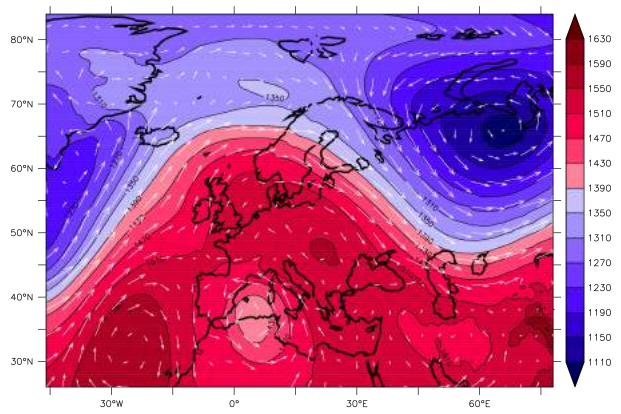


Figure 6.4.1. CAMS global geopotential height (gpm) (shaded) and wind direction (white arrows) at 850 hPa during the time period 21-23 Jan 2017.

To investigate if and how this pollution event is reproduced by the CAMS global and regional ensemble forecasts, and how the two products compare with each other, we present the time evolution of the respective mean daily fields for various trace gas species. Figure 6.4.2, depicts the mean daily CO concentrations for CAMS-global (Fig. 6.4.2a) and the regional ensemble (Fig. 6.4.2b), showing a gradual increase in CO concentrations over south UK and Benelux in both forecast products. The respective NO fields (Fig. 6.4.3) resemble the previous temporal evolution. However, it is noteworthy that the CAMS-global NO levels are much higher compared to those of the regional ensemble. Regarding $NO_2$, both global and regional products also indicate a pollution episode (Fig. 6.4.4), however, the regional ensemble exhibits higher concentrations compared to CAMS.

Both CAMS-global and regional ensemble show lower $O_3$ over the NOx source regions of UK and Benelux due to titration. However, this O3 decrease from titration is larger in CAMS-global $O_3$ fields than in regional ensemble, due to the fact that the CAMS-global NO levels are higher compared to those of the regional ensemble (Fig. 6.4.5).

Finally, the $SO_2$ fields depict higher concentrations compared to days prior the event (not shown), yet there are conspicuous discrepancies between the two products over the Balkans and the Levant region (Fig. 6.4.6).

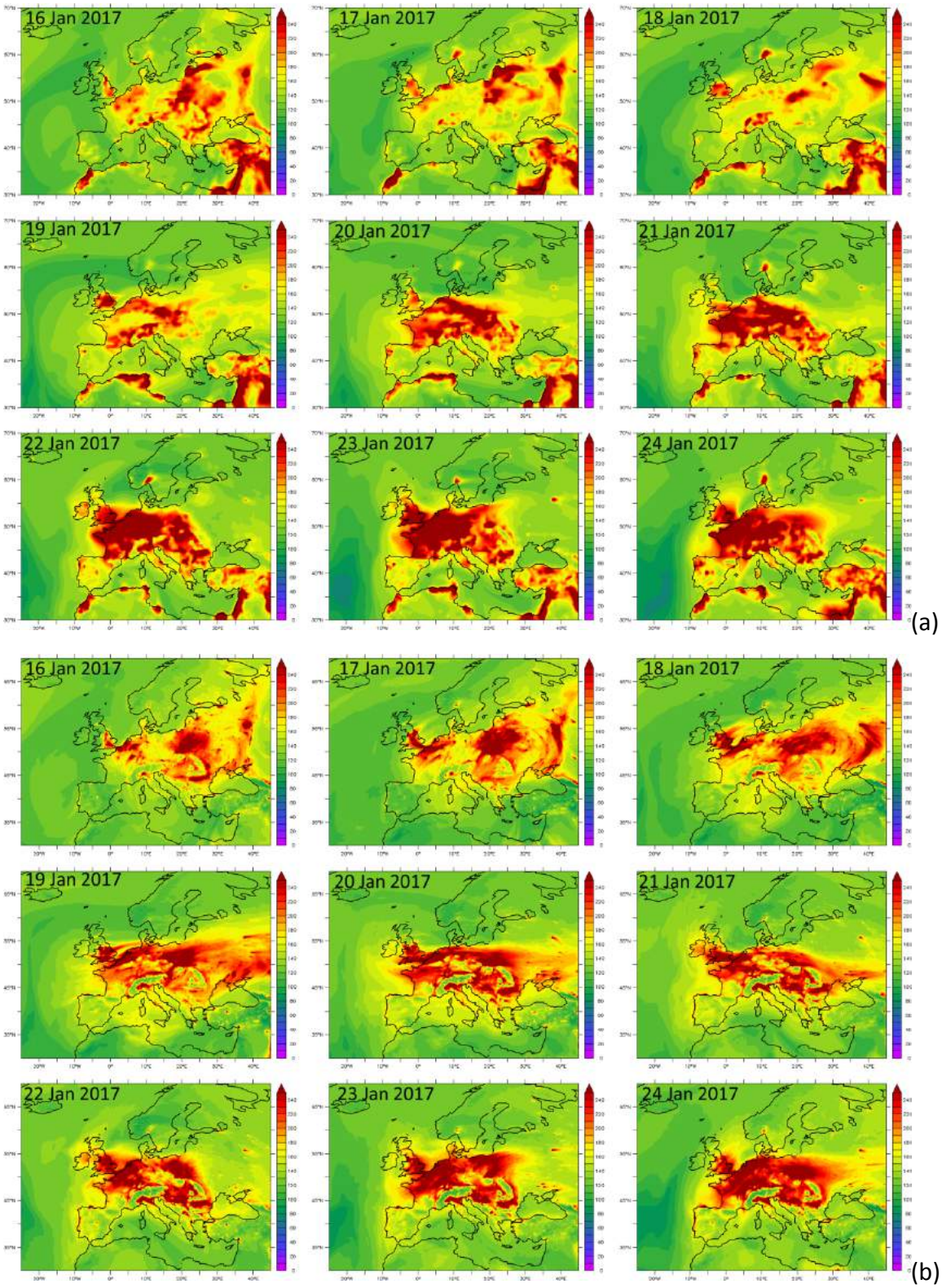


Figure 6.4.2. Mean daily CO surface concentrations (ppb) for (a) CAMS-global and (b) regional ENSEMBLE during the time period 16 Jan 2017 – 24 Jan 2017.

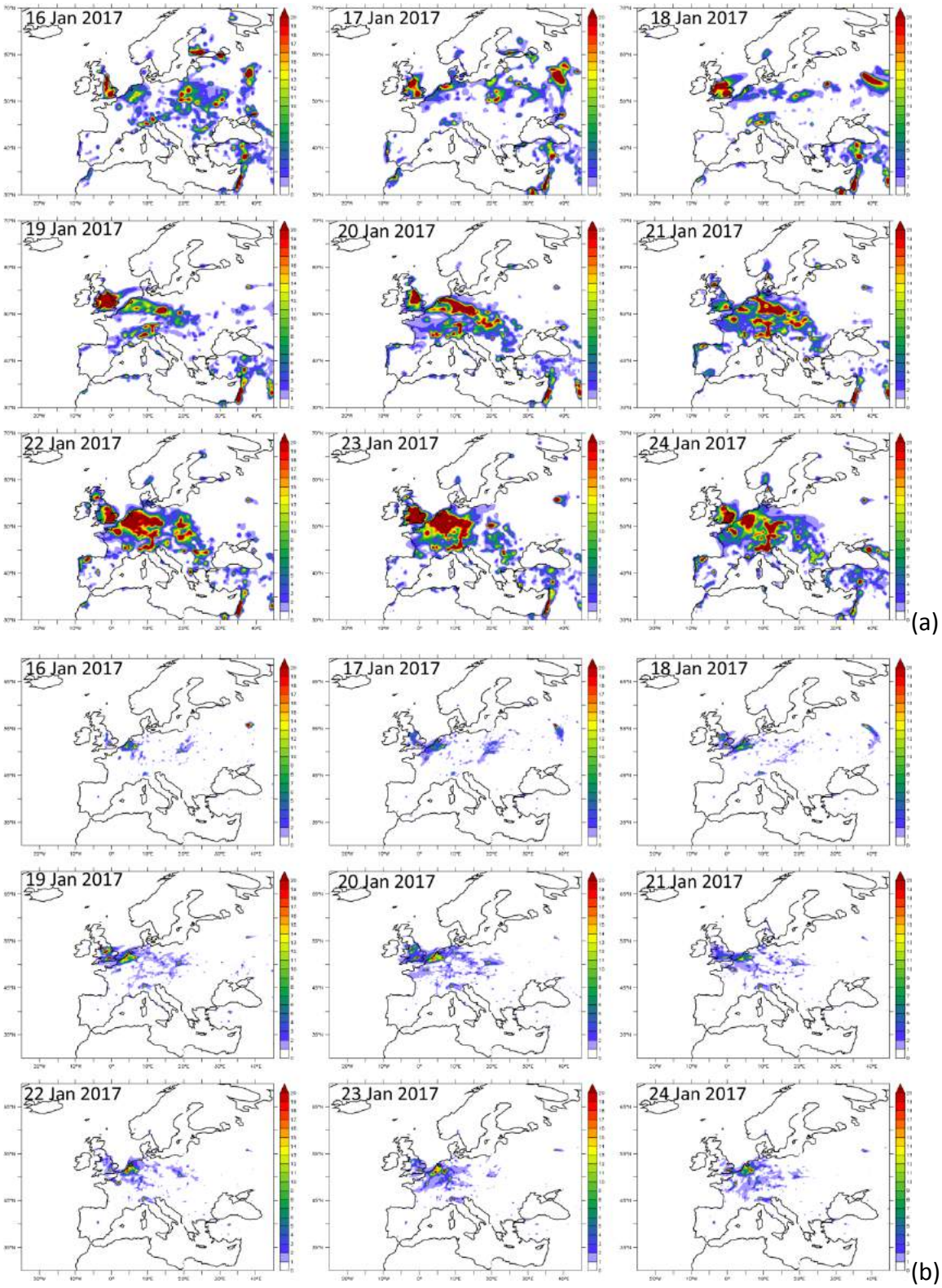


Figure 6.4.3. Mean daily NO surface concentrations (ppb) for (a) CAMS-global and (b) regional ENSEMBLE during the time period 16 Jan 2017 – 24 Jan 2017.

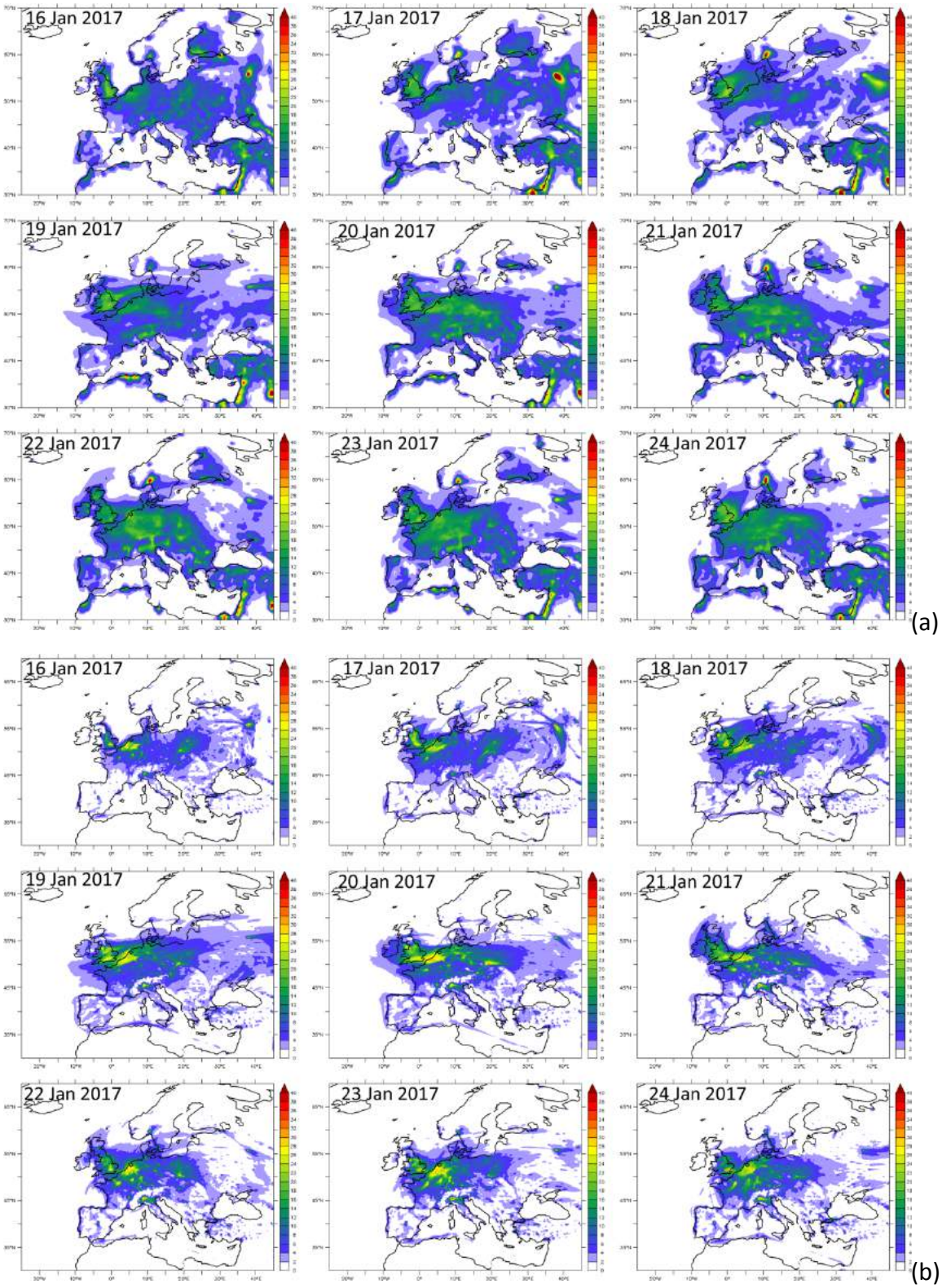


Figure 6.4.4. Mean daily $NO_2$ surface concentrations (ppb) for (a) CAMS-global and (b) regional ENSEMBLE during the time period 16 Jan 2017 – 24 Jan 2017.

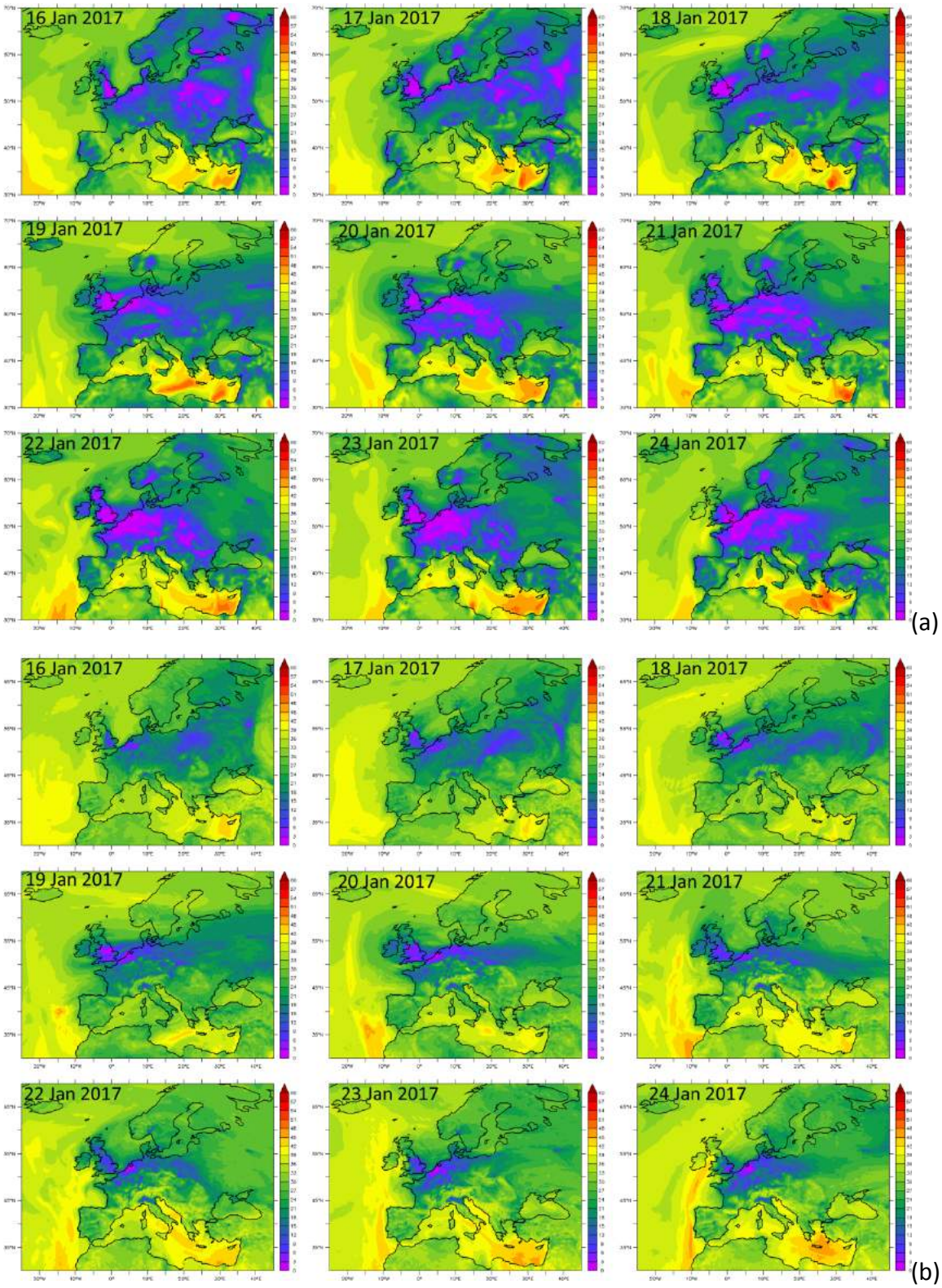


Figure 6.4.5. Mean daily O3 surface concentrations (ppb) for (a) CAMS-global and (b) regional ENSEMBLE during the time period 16 Jan 2017 – 24 Jan 2017.

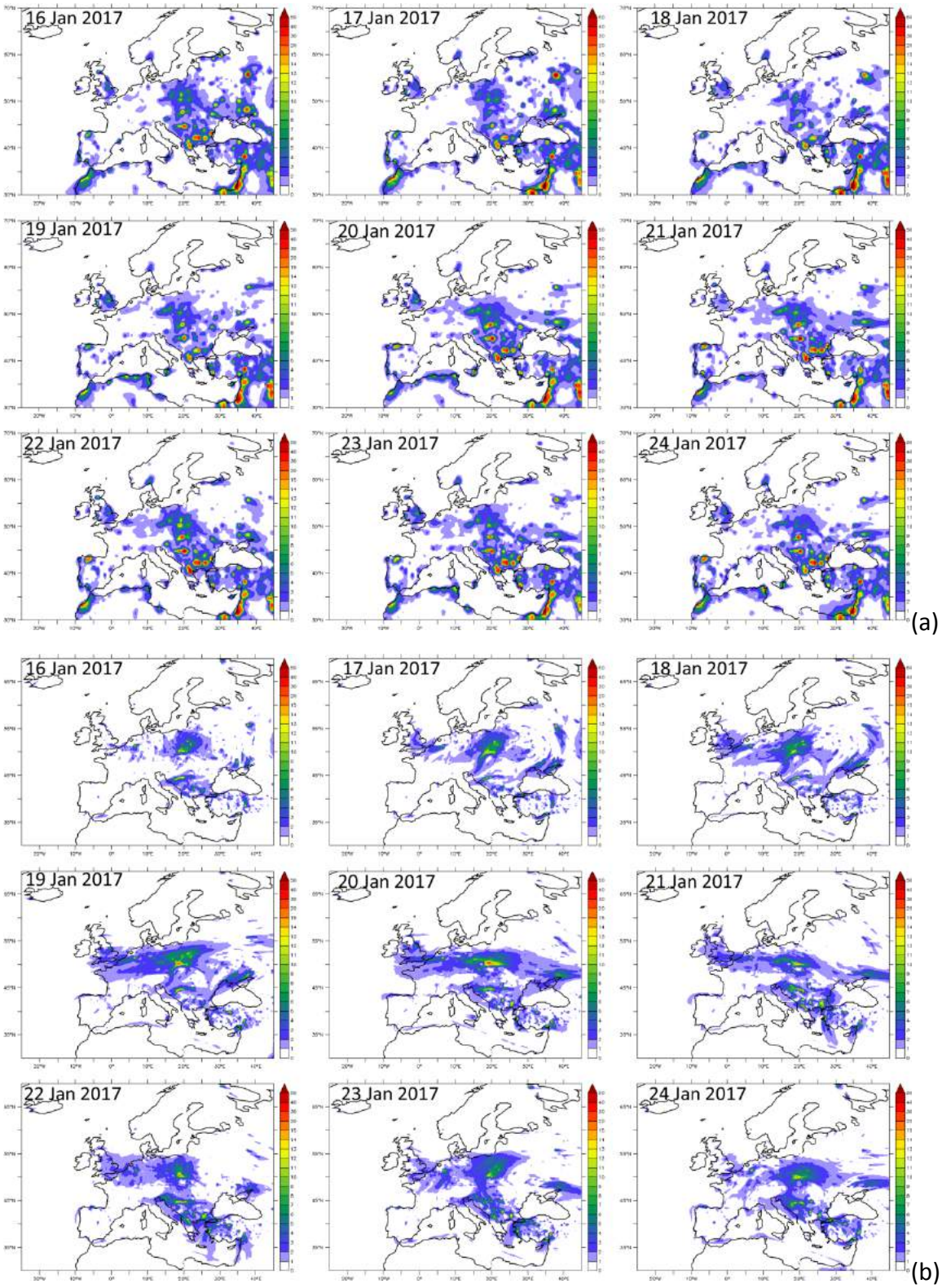


Figure 6.4.6. Mean daily SO2 surface concentrations (ppb) for (a) CAMS-global and (b) regional ENSEMBLE during the time period 16 Jan 2017

## 6.5 Iberian Peninsula, 1-12 September 2016

*Taken from the SON-2016 CAMS-regional validation report [reg2017b].*

In this section we study a case of special interest over the Iberian Peninsula based on the CAMS-global forecast. The period 1-12 September 2016 is presented below and shows two combined events: a dust transport case and an event with high CO/aerosol, which could be eventually identified as biomass burning. The consistency between the CAMS-global and ENS forecasts products is discussed.

During the first days of September CAMS-global CO values over the Iberian Peninsula peaked. The ENS CO forecast did not exhibit any CO maximum during the same days. To identify this CAMS-global CO-rich source, we show the mean daily CAMS-global CO fields over the Iberian Peninsula from the 1$^{st}$ to the 12$^{th}$ of August (Figure 6.5.1). It seems that on September 7th the event reaches its maximum activity. High CO emissions over northern Portugal are emitted this day and disperse in the rest of the IP during the following days. The CAMS-global CO mass densities exceed locally 1000 mg/m3. In order to further investigate the source of this event, we plotted local maxima of other species (Figure 6.5.2) all occurring on September 7th. These species are CAMS-global black carbon, organic carbon, formaldehyde (HCHO), nitric acid (HNO3), nitrogen monoxide (NO), nitrogen dioxide (NO2). Eventually this event could be identified as a biomass-burning event. Figure 6.5.3 shows ENS-CO mass densities for the time period 1-12/9, identifying the same maximum CO sources over northern Portugal during the 8$^{th}$ of September but with considerably lower mass densities. The inconsistency of the North African CO emissions between CAMS-global and ENS is also evident in these figures, and they have been discussed in all our previous reports.

A dust event is also identified in CAMS-global during the period of 1-9 September over the Iberian Peninsula. Figure 6.5.4 shows CAMS-global PM10 and Figure 6.5.5 shows the CAMS-global dust-only contribution which maximizes during 4-7 September. Figure 6.5.6 shows the PM10 contribution of ENS for the same days, using the same colour bar and units to allow for a direct comparison with CAMS-global PM10. During these days CAMS-global indicates high aerosol contributions (exceeding 100 µg/m3 locally) while ENS aerosols are not higher than 50 µg/m3. The detailed species contributions provided by CAMS-global (but not in ENS) shows that the source of aerosol is a mixture of black/organic carbon and dust.

This analysis indicates that for this specific event in the beginning of September the CO and aerosol contributions of CAMS-global are higher than those of ENS. The composition information in CAMS-global is useful in identifying sources of emissions and their relative contribution with respect to the overall pollution burden.

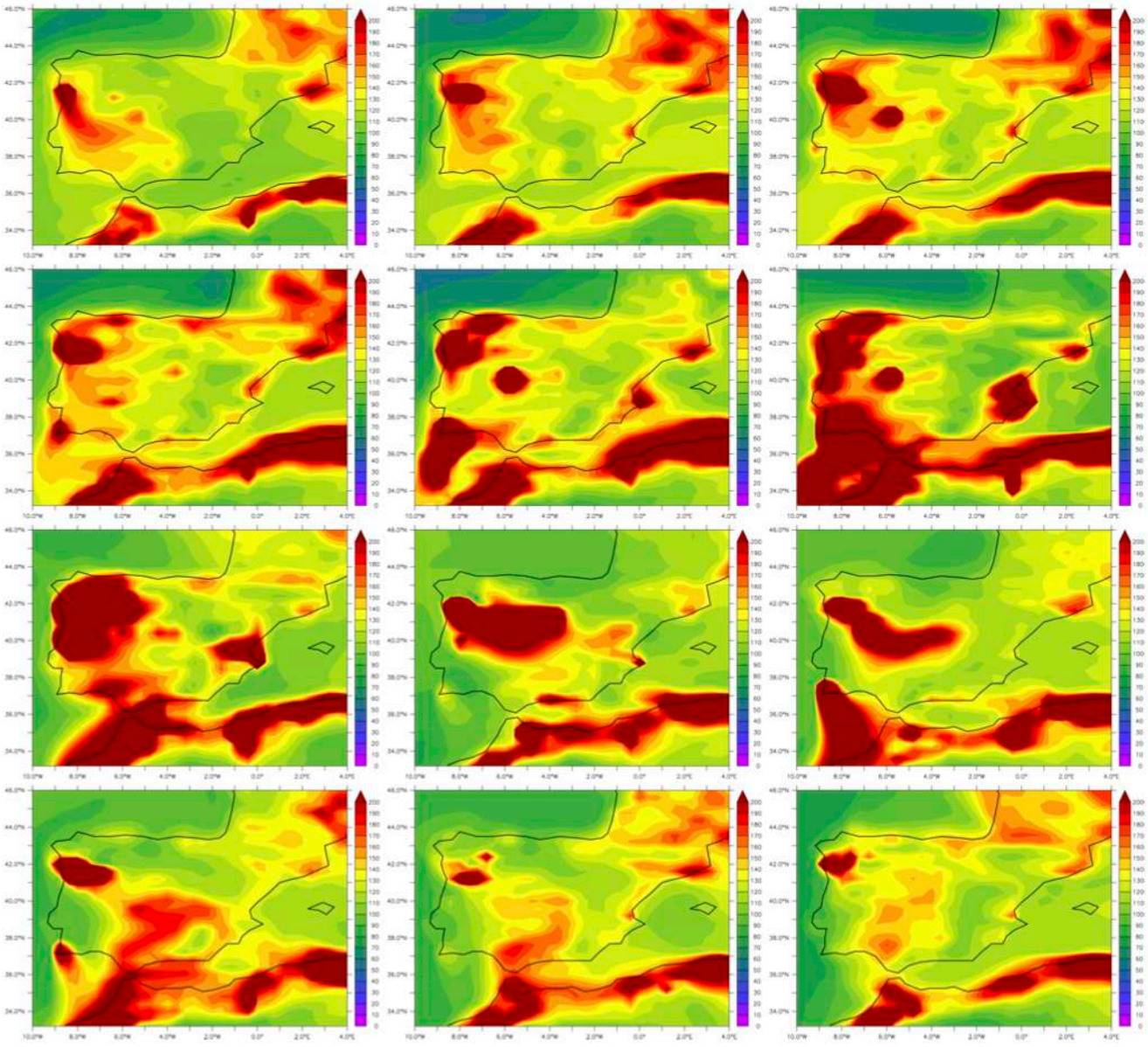

Figure 6.5.1. Mean daily CAMS-global CO over the Iberian Peninsula. Each panel is a mean daily contour starting from 1/9/2016 (top-left) ending 12/9/2016 (bottom-right). Units in µg/m3.

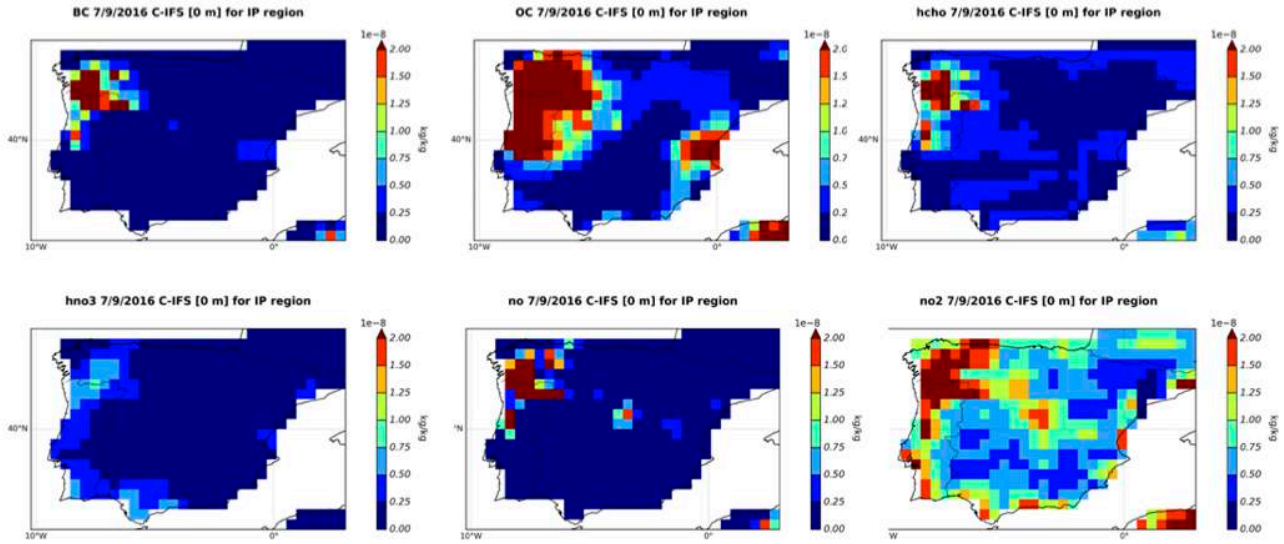


Figure 6.5.2. Mean daily CAMS-global species over the Iberian Peninsula for the 7th of September. The species (from top left to bottom-right) are black carbon, organic carbon, formaldehyde (HCHO), nitric acid (HNO3), nitrogen monoxide (NO), nitrogen dioxide (NO2). Units in Kg/Kg.

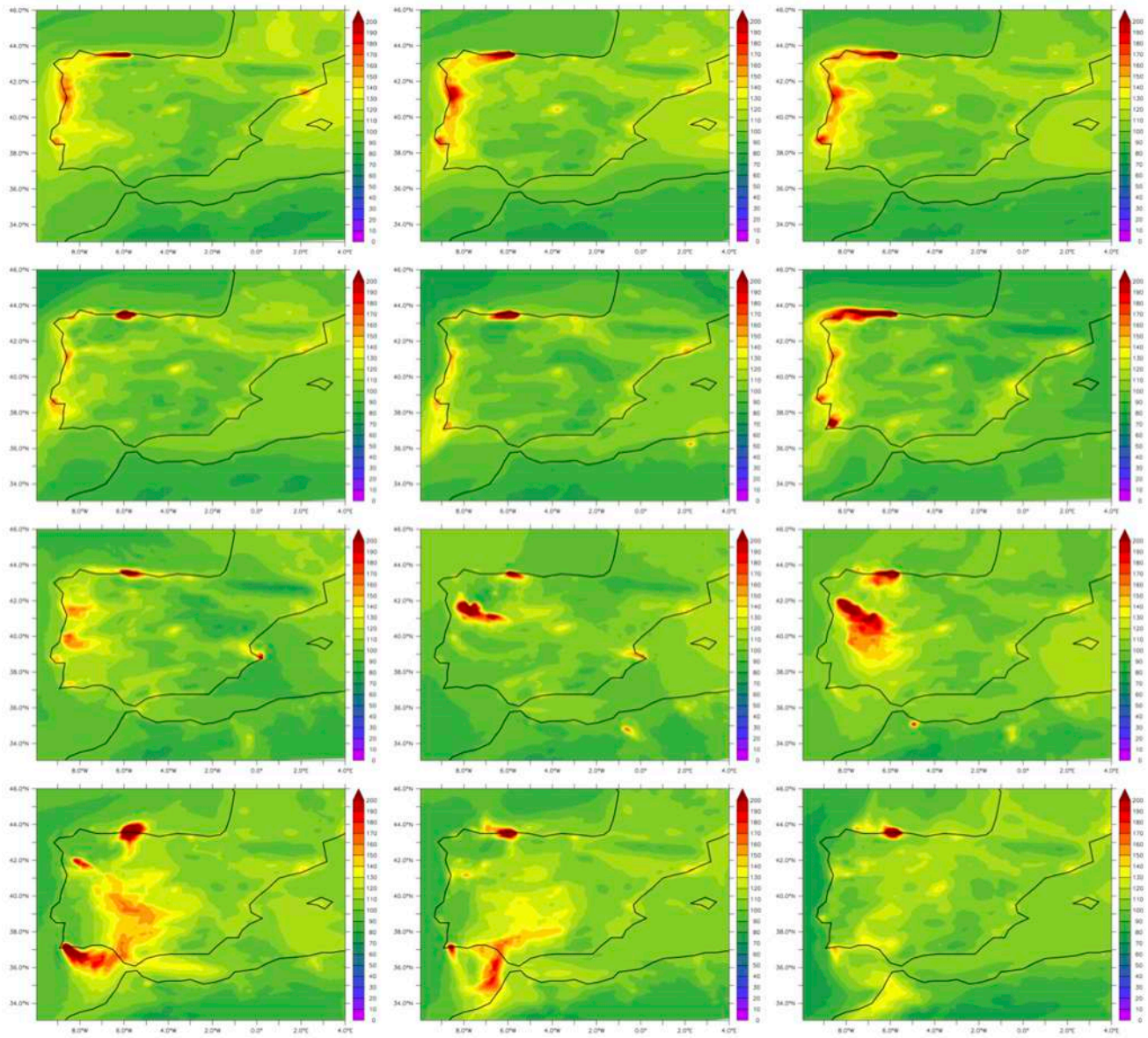

Figure 6.5.3. Mean daily ENS CO over the Iberian Peninsula. Each panel is a mean daily contour starting from 1/9/2016 (top-left) ending 12/9/2016 (bottom-right). Units in mg/m3.

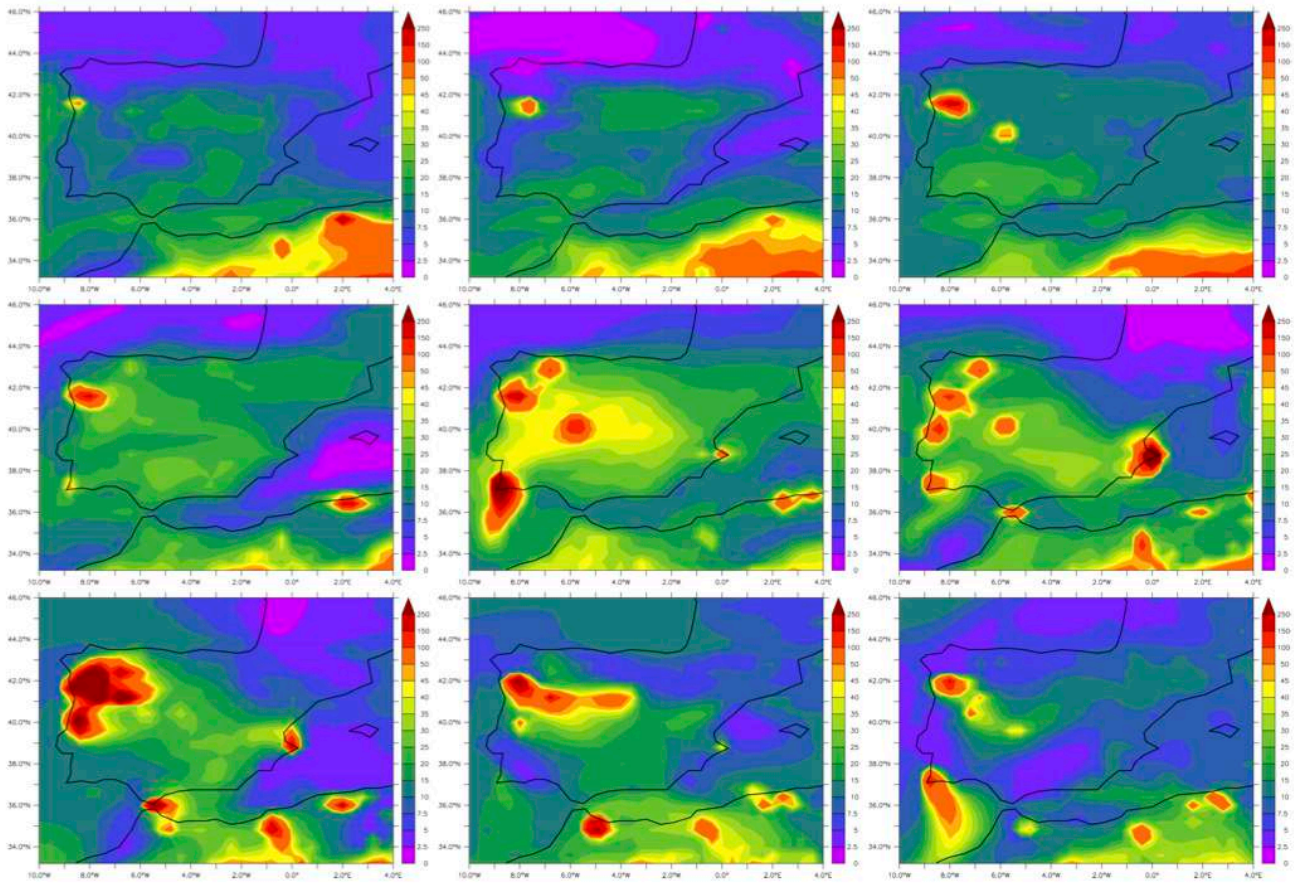

Figure 6.5.4. Mean daily ENS PM10 over the Iberian Peninsula. Each panel is a mean daily contour starting from 1/9/2016 (top-left) ending 9/9/2016 (bottom-right). Units in mg/m3.

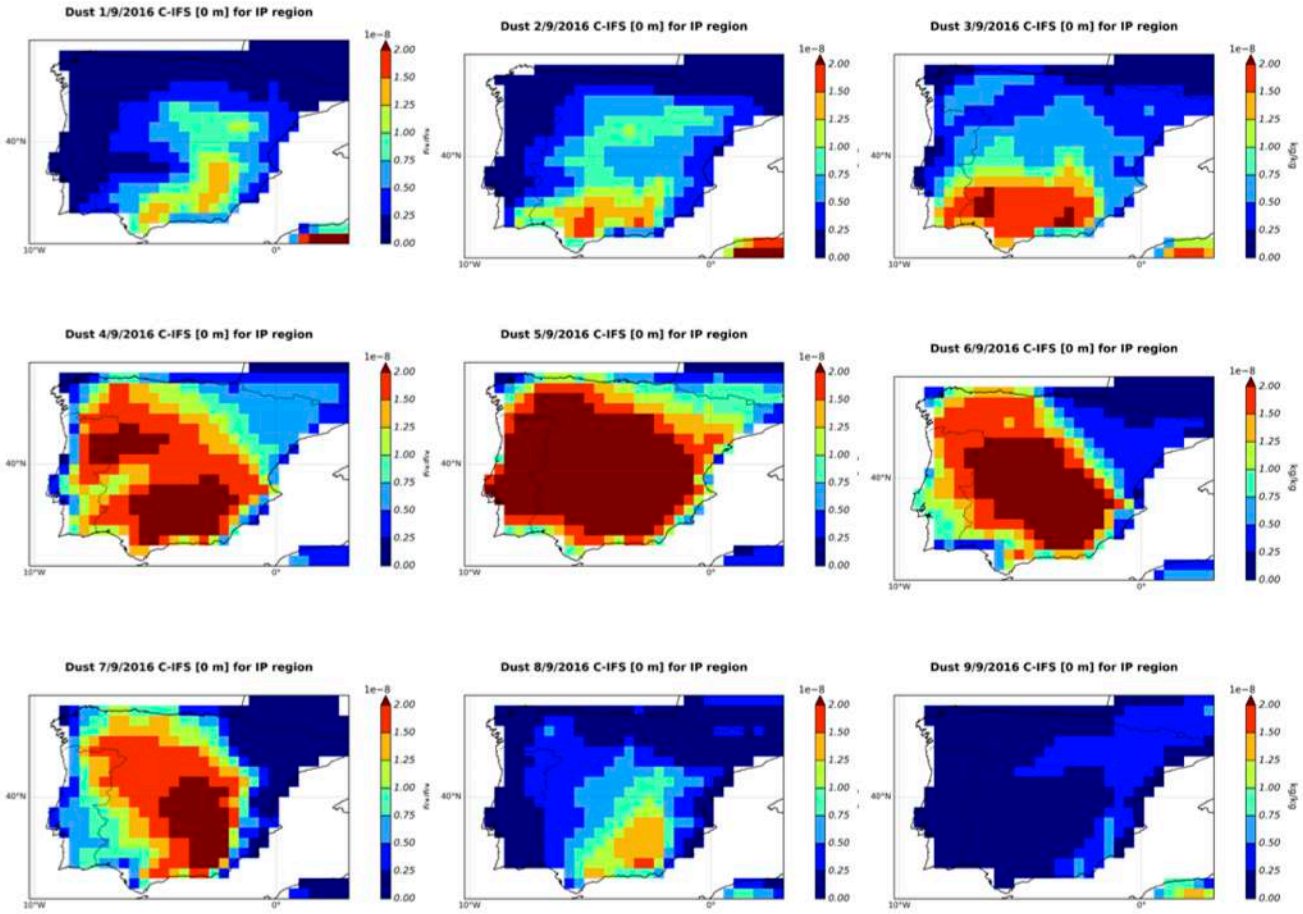


Figure 6.5.5. Mean daily dust aerosol CAMS-global species over the Iberian Peninsula. Each panel is a mean daily contour starting from 1/9/2016 (top-left) ending 9/9/2016 (bottom-right). Units in Kg/Kg.

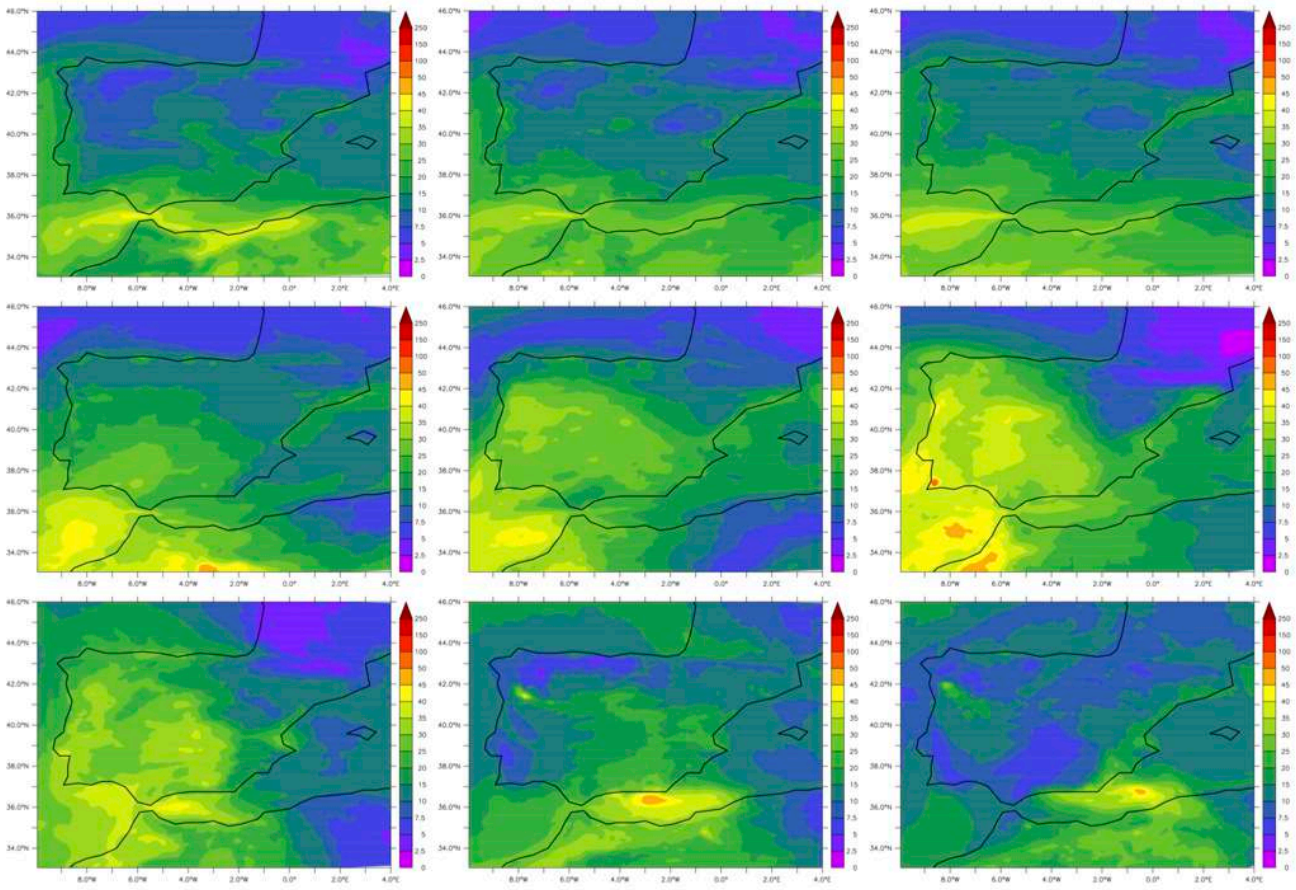

Figure 6.5.6. Mean daily ENS-PM10 species over the Iberian. Each panel is a mean daily contour starting from 1/9/2016 (top-left) ending 9/9/2016 (bottom-right). Units in µg/m3.

## 6.6 Ozone vertical transport, July-August 2016

*Taken from the JJA-2016 CAMS-regional validation report [reg2016a].*

During summer 2016, the eastern Mediterranean region shows a free tropospheric pool of high $O_3$, as suggested by both observational and modeling studies. These high ozone concentrations are mainly attributed to the downward $O_3$ transport from the upper troposphere and the lower stratosphere, as a result of the enhanced subsidence over the region and the development of tropopause folding events. The CAMS-global model reproduces this pool of high $O_3$ concentrations in the middle troposphere over the eastern Mediterranean region during the examined period in July-August (Figure 6.6.1, top). Moreover, the vertical cross sections of the average July-August $O_3$ concentrations at $35^o$ E and $35^o$ N (Figure 6.6.1, left and right) reveal the southeastern and downward transport of high-ozone air masses from the upper troposphere and the lower stratosphere. These high $O_3$ concentrations in middle troposphere were also captured by the regional ENSEMBLE and its individual members.

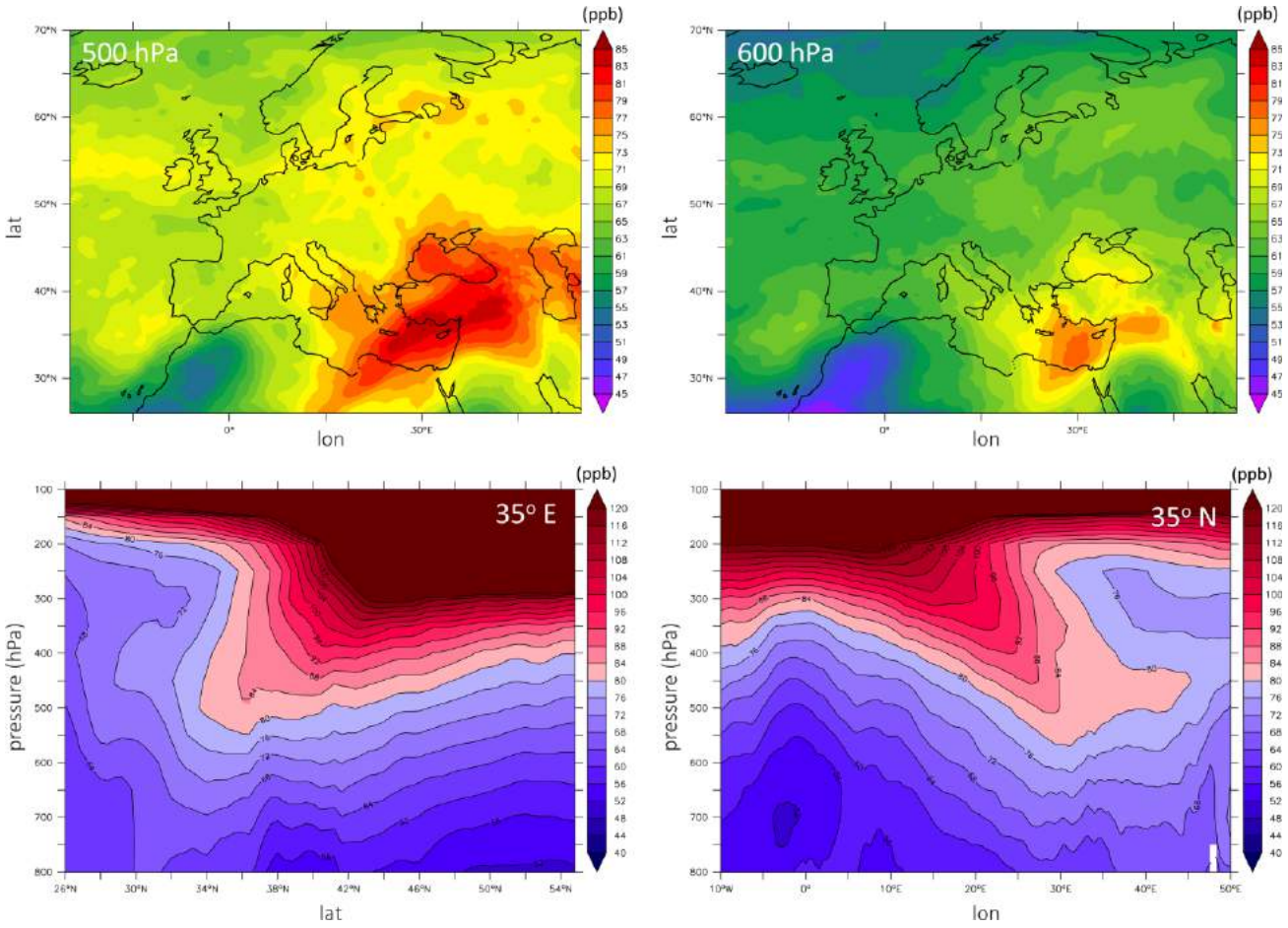


Figure 6.6.1. CAMS-global mean July-August ozone concentrations (ppb) at 500 (top left) and 600 hPa (top right). Latitude-pressure cross section of CAMS-global mean July-August ozone concentrations at 35° E (bottom left) and longitude-pressure cross section of CAMS-global mean July-August concentrations (ppb) at 35° N (bottom right).

## 6.7 Dust episode, May 2016

*Taken from the MAM-2016 CAMS-regional validation report [reg2016b].*

During the period May-June 2016 three dust transport episodes were identified over the Mediterranean region, two of them at 12th and 20th of May and the other one at the 20th of June. The case on the 20th of May has been chosen for further analysis, as it was the most intense. The vertical distribution of PM10 daily mean concentrations for CAMS-global, ENS and the individual regional ensemble members are shown. Three points have been chosen along the dust transport pathway (Figure 6.7.1): i) North Libya, where dust is produced (point A) ii) Mediterranean Sea (point B) and iii) continental Europe (point C).

Figure 6.7.2 shows the fields of mean daily PM10 for CAMS-global, ENS and the regional ensemble members during the 20th of May 2016 at four different vertical layers (0, 250, 2000 and 5000 m). Both the global and regional CAMS forecasts capture the dust transport event, although there are some differences in the transport pathways between the two products. According to the global

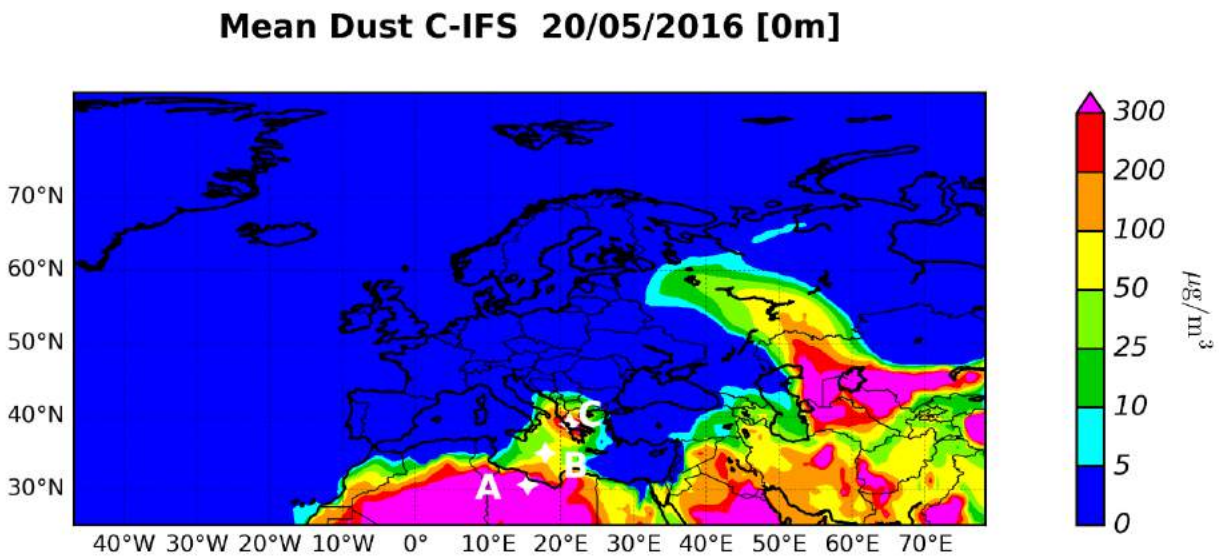


Figure 6.7.1. Daily mean dust field of CAMS-global for 20th of May. The selected points A, B and C for the vertical distribution are indicated with stars.

forecast, dust is transported over the Mediterranean Sea and subsequently is deposited in continental Europe (Greece). In the regional ensemble dust does not reach the European mainland. The differences in the vertical transport between CAMS-global and ENS along the Mediterranean corridor maximize in the upper vertical layers (above 4 Km), where the majority of regional models have higher PM10 compared to CAMS-global.

This feature is better illustrated in Figure 6.7.3, which shows the mean daily PM10 vertical profiles over points A, B and C for CAMS-global, ENS and the regional ensemble members. According to Figure 3, CAMS-global transports dust along the Mediterranean Sea in altitudes from 1 to 3 Km (point B) and when it reaches continental Europe (point C) the dust maximum of aerosol mass in the vertical profile is found below 1 Km altitude. The vertical profiles of ENS and regional ensemble members do not indicate dust transport to continental Europe.

With respect to regional model variability there seems to be a general agreement in model behavior, with a few exceptions.

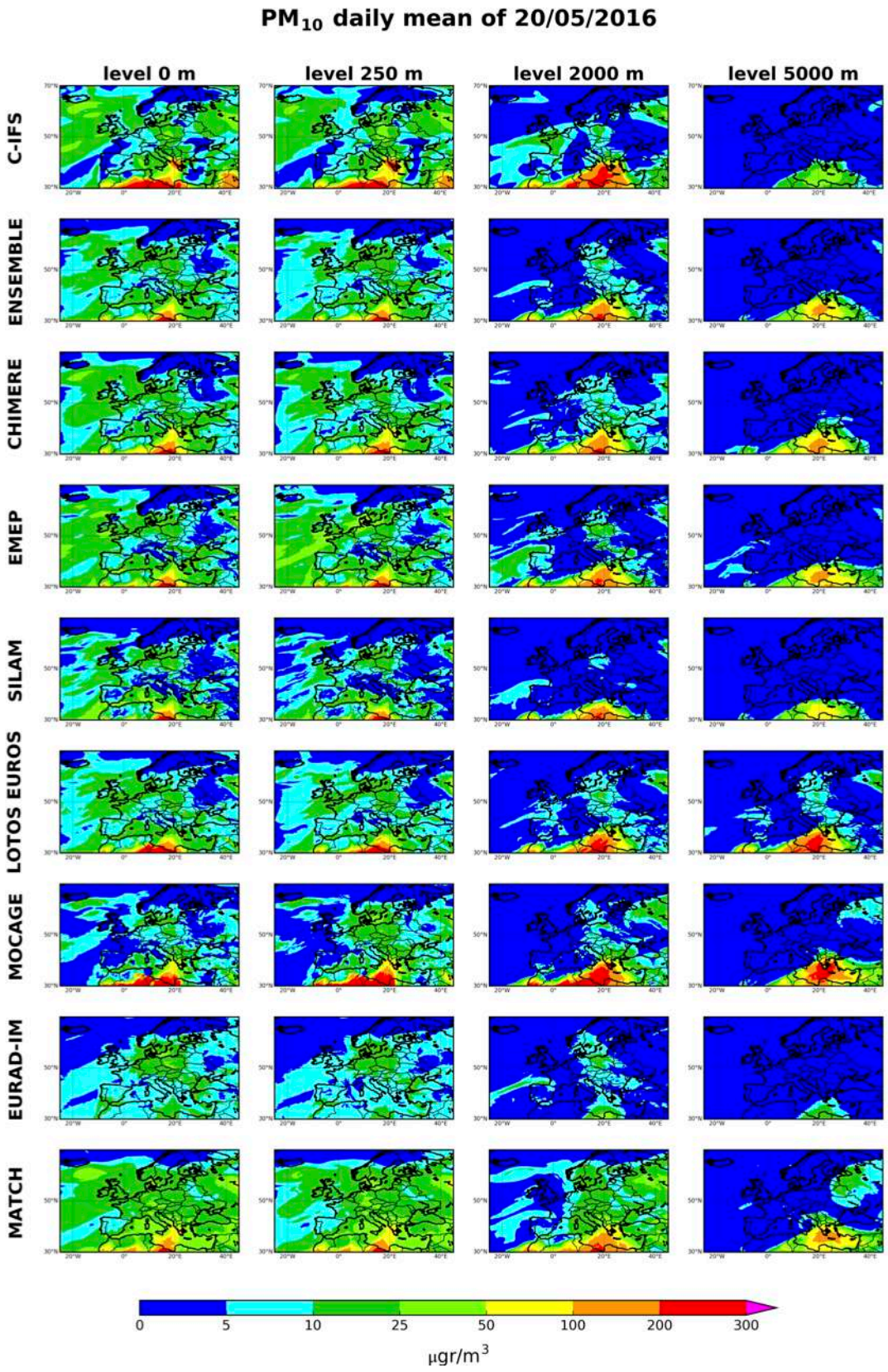


Figure 6.7.2. Mean global and regional ensemble forecast PM10 fields for four different vertical layers (0, 250, 2000, 5000 m) of 20th May.

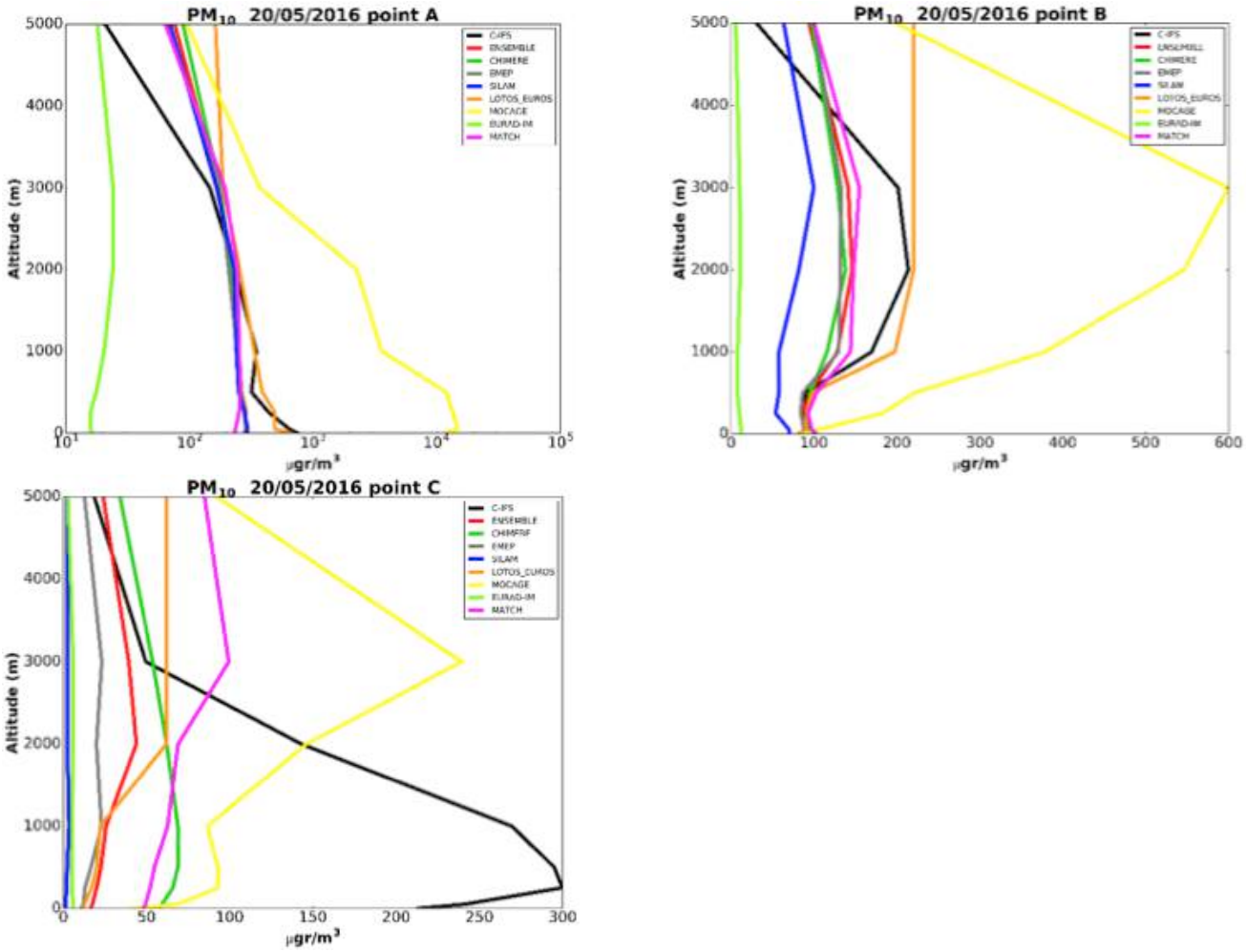


Figure 6.7.3. Daily mean PM10 vertical distribution of CAMS-global, ENS and individual regional ensemble members at the points A (top-left), B (top-right) and C (bottom) for the 20th of May.

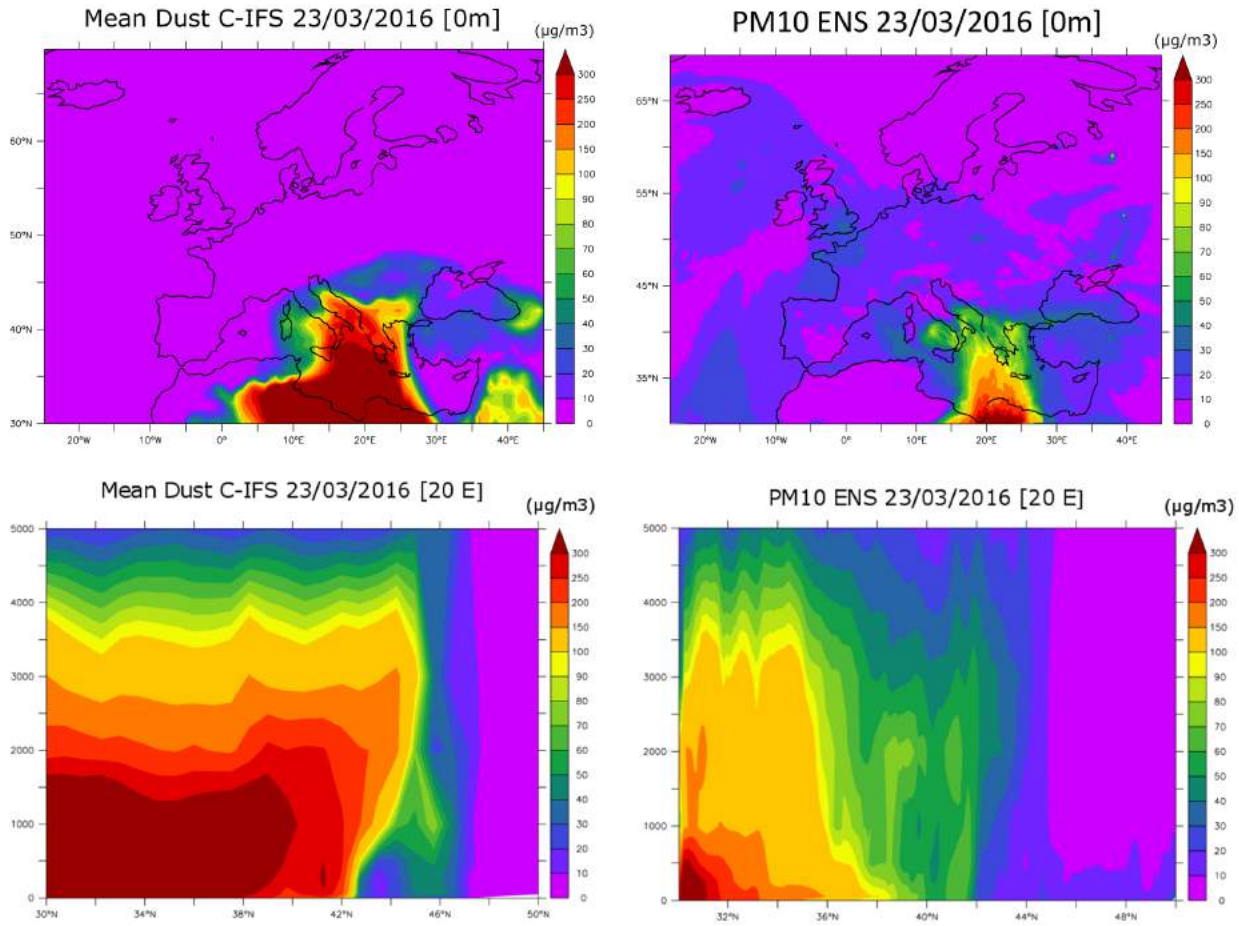


Figure 6.8.1. Mean daily CAMS-global surface dust (top left) and mean daily ENS surface PM10 (top right) for 23/3/2016. Latitude-height cross sections at 20$^{o}$ E of mean daily CAMS-global dust (bottom left) and mean daily ENS PM10 (bottom right) for 23/3/2016.

## 6.8 Dust episode, 23 March 2016

*Taken from the FMA-2016 CAMS-regional validation report [reg2016c].*

During March and April 2016, African dust transport occured from North Africa to Europe. Figure 6.8.1 shows the mean daily global dust product (DU1+DU2+DU3) for the 23$^{rd}$ of March and we compare with surface *P*M10 of the regional ensemble (Fig 25). African dust follows one of its major transport paths to southern Europe, reaching to Italy and the Balkan Peninsula. The differences in the regional and global products partially stems from the fact the global dust includes particles with diameters up to 20 µm, while regional dust up to 10 µm. The dust latitude cross section at 20 deg E is shown in Fig 6.8.1 (bottom) indicating the northward vertical transport of dust extending up to ~5 km altitude.

# 7 Heat waves

## 7.1 Heat wave in Europe, 2003

*Taken from the 2003-2016 CAMS-global reanalysis report [rea2018].*

The CAMS-global reanalysis (period 2003-2016) performance was validated during the 1st half of August 2003. This is the period of the major heat wave over central and north-western Europe (Fig. 7.1.1), with exceptionally warm and dry weather, and a strongly increased surface ozone as recorded by in-situ monitors. This event has been extensively discussed in connection to an increased number of deaths (WHO, 2004).

The peak in surface ozone can even be seen in the GAW observations of high altitude stations like Sonnblick (SNB), see Fig. 7.1.2. The model could correctly reproduce this episode of increased $O_3$ with only little underestimation of the maximum concentrations.

Fig. 7.1.3 shows surface ozone times series (observed and modelled) during August 2003 at four stations located in France, Germany and Switzerland where very high ozone concentrations (up to 120 ppb) were observed during 1-14 August. From these figures it is evident that all reanalysis runs underestimate peak values in surface ozone although there is still a significant improvement over the MACC reanalysis by both the CAMS control and the CAMS reanalysis in terms of both biases and correlations. The August 2003 event provided a unique extreme case to study the performance of the new relative to the old reanalysis. As an overall conclusion, we can see that CAMS control and reanalysis is a significant improvement over the MACC reanalysis, particularly over central and northern Europe and that the differences between models and observations have not worsened in the case of the extreme event in 2003.

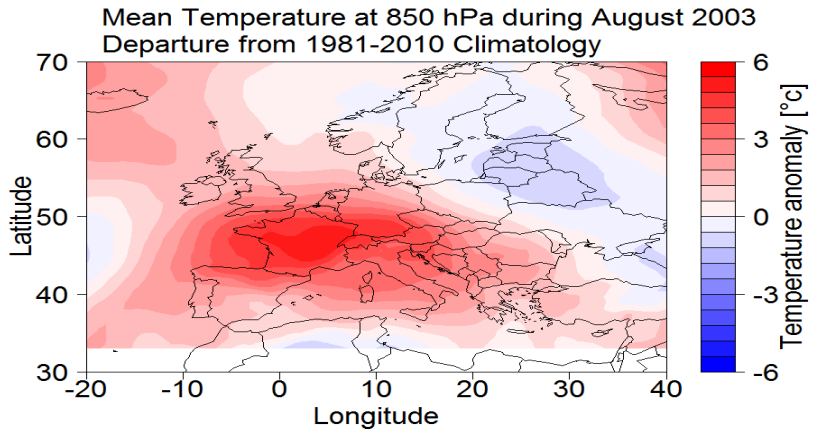


Figure 7.1.1: Spatial distribution of the Air temperature anomaly at 850 hPa in August 2003, compared to the 1981-2010 climatology.

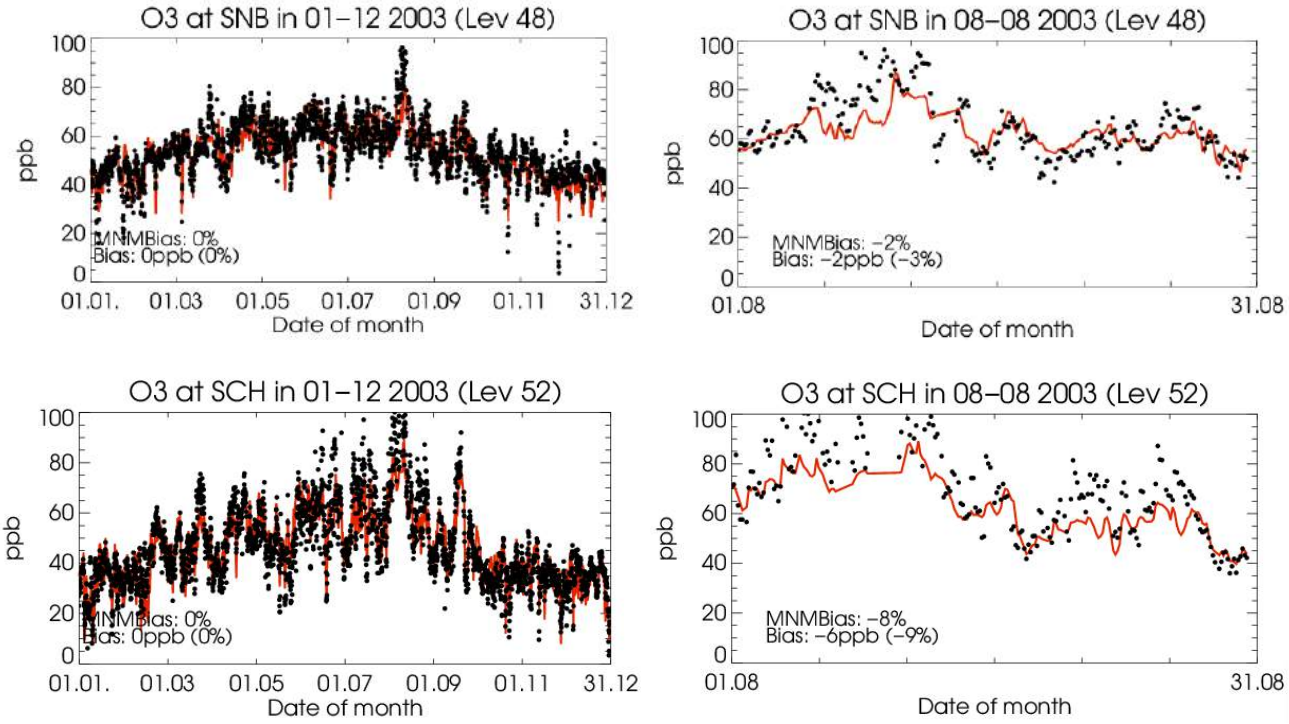


Figure 7.1.2: Time series for $O_3$ for Sonnblick Station (upper panel) and Schauinsland station (lower panel) during the whole year of 2003 (left) and for August 2003 (right).

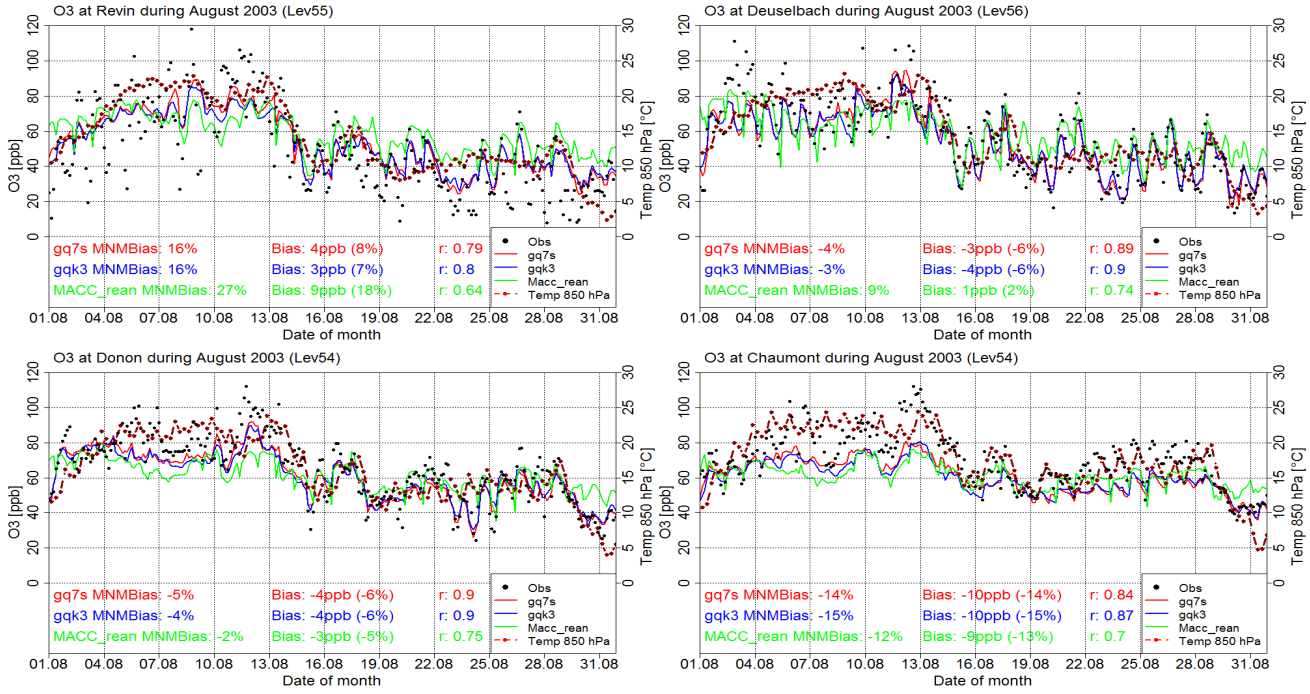


Figure 7.1.3: Time series of ozone over Revin, France (49.90°N, 4.63°E, top left), over Donon, France (48.50°N, 7.13°E, top right), over Deuselbach, Germany (49.76°N, 7.05°E, down left), over Chaumont, Switzerland (47.05°N, 6.98°E, down left) for the period of the intense heat wave over Europe 1 August - 31 August. Observations are in black, the CAMS reanalysis is in red, the CAMS control in blue and the MACC reanalysis in green.

# 8 References

The results above were taken from the following CAMS-84 documents:

*Akritidis, D., Katragkou, E., Zanis, P., Pytharoulis, I., Melas, D., Flemming, J., Inness, A., Clark, H., Plu, M., and Eskes, H.: A deep stratosphere-to-troposphere ozone transport event over Europe simulated in CAMS global and regional forecast systems: analysis and evaluation, Atmos. Chem. Phys., 18, 15515-15534, https://doi.org/10.5194/acp-18-15515-2018, 2018.*

*[nrt2018a] H.J. Eskes, A. Wagner, M. Schulz, Y. Christophe, M. Ramonet, S. Basart, A. Benedictow, Y. Bennouna, A.-M. Blechschmidt, S. Chabrillat, H. Clark, E. Cuevas, H. Flentje, K.M. Hansen, U. Im, J. Kapsomenakis, B. Langerock, K. Petersen, A. Richter, N. Sudarchikova, V. Thouret, T. Warneke, C. Zerefos, Validation report of the CAMS near-real-time global atmospheric composition service: Period March - May 2018, Copernicus Atmosphere Monitoring Service (CAMS) report, CAMS84_2015SC3_D84.1.1.12_2018MAM_v1.pdf, October 2018.*

*[nrt2018b] H.J. Eskes, A. Wagner, M. Schulz, Y. Christophe, M. Ramonet, S. Basart, A. Benedictow, Y. Bennouna, A.-M. Blechschmidt, S. Chabrillat, H. Clark, E. Cuevas, H. Flentje, K.M. Hansen, U. Im, J. Kapsomenakis, B. Langerock, K. PetersEN, A. Richter, N. Sudarchikova, V. Thouret, T. Warneke, C. Zerefos, Validation report of the CAMS near-real-time global atmospheric composition service: Period December 2017 - February 2018, Copernicus Atmosphere Monitoring Service (CAMS) report, CAMS84_2015SC3_D84.1.1.11_2018DJF_v1.pdf, May 2018.*

*[nrt2018c] H.J. Eskes, A. Wagner, M. Schulz, Y. Christophe, M. Ramonet, S. Basart, A. Benedictow, Y. Bennouna, A.-M. Blechschmidt, S. Chabrillat, H. Clark, E. Cuevas, H. Flentje, K.M. Hansen, U. Im, J. Kapsomenakis, B. Langerock, K. PetersEN, A. Richter, N. Sudarchikova, V. Thouret, T. Warneke, C. Zerefos, Validation report of the CAMS near-real-time global atmospheric composition service: Period September-November 2017, Copernicus Atmosphere Monitoring Service (CAMS) report, CAMS84_2015SC3_D84.1.1.10_2017SON_v1.pdf, February 2018.*

*[nrt2017a] H.J. Eskes, A. Wagner, M. Schulz, Y. Christophe, M. Ramonet, S. Basart, A. Benedictow, A.-M. Blechschmidt, S. Chabrillat, H. Clark, E. Cuevas, H. Flentje, K.M. Hansen, U. Im, J. Kapsomenakis, B. Langerock, K. Petersen, A. Richter, N. Sudarchikova, V. Thouret, T. Warneke, C. Zerefos, Validation report of the CAMS near-real-time global atmospheric composition service: Period June - August 2017, Copernicus Atmosphere Monitoring Service (CAMS) report, CAMS84_2015SC2_D84.1.1.9_2017JJA_v1.pdf, November 2017.*

*[nrt2017b] H.J. Eskes, A. Wagner, M. Schulz, Y. Christophe, M. Ramonet, S. Basart, A. Benedictow, A.-M. Blechschmidt, S. Chabrillat, H. Clark, E. Cuevas, H. Flentje, K.M. Hansen, U. Im, J. Kapsomenakis, B. Langerock, K. PetersEN, A. Richter, N. Sudarchikova, V. Thouret, T. Warneke, C. Zerefos, Validation report of the CAMS near-real-time global atmospheric composition service: March - May 2017, Copernicus Atmosphere Monitoring Service (CAMS) report, CAMS84_2015SC2_D84.1.1.7_2017MAM_v1.pdf, September 2017.*

*[nrt2017c] H.J. Eskes, A. Wagner, M. Schulz, Y. Christophe, M. Ramonet, S. Basart, A. Benedictow, A.-M. Blechschmidt, S. Chabrillat, H. Clark, E. Cuevas, H. Flentje, K.M. Hansen, U. Im, J. Kapsomenakis, B. Langerock, K. PetersEN, A. Richter, N. Sudarchikova, V. Thouret, T. Warneke, C. Zerefos, Validation report of the CAMS near-real-time global atmospheric composition service: December 2016 - February 2017, Copernicus Atmosphere Monitoring Service (CAMS) report, CAMS84_2015SC2_D84.1.1.7_2017DJF_v1.pdf, May 2017.*

*[nrt2017d] H.J. Eskes, A. Wagner, M. Schulz, Y. Christophe, M. Ramonet, S. Basart, A. Benedictow, A.-M. Blechschmidt, S. Chabrillat, H. Clark, E. Cuevas, H. Flentje, K.M. Hansen, U. Im, J. Kapsomenakis, B. Langerock, A. Richter, N. Sudarchikova, V. Thouret, T. Warneke, C. Zerefos, Validation report of the CAMS near-real-time*

*global atmospheric composition service: September-November 2016, Copernicus Atmosphere Monitoring Service (CAMS) report, CAMS84_2015SC2_D84.1.1.6_2016SON_v1.pdf, February 2017.*

*[nrt2016a] H.J. Eskes, A. Wagner, M. Schulz, Y. Christophe, M. Ramonet, S. Basart, A. Benedictow, A.-M. Blechschmidt, S. Chabrillat, H. Clark, E. Cuevas, H. Flentje, K.M. Hansen, U. Im, J. Kapsomenakis, B. Langerock, A. Richter, N. Sudarchikova, V. Thouret, T. Warneke, C. Zerefos, Validation report of the CAMS near-real-time global atmospheric composition service. System evolution and performance statistics; Status up to 1 September 2016, Copernicus Atmosphere Monitoring Service (CAMS) report, CAMS84_2015SC1_D84.1.5_201611_v1.pdf, November 2016.*

*[nrt2016b] V. Huijnen, H.J. Eskes, A. Wagner, M. Schulz, Y. Christophe, M. Ramonet, S. Basart, A. Benedictow, A.-M. Blechschmidt, S. Chabrillat, H. Clark, E. Cuevas, H. Flentje, K.M. Hansen, U. Im, J. Kapsomenakis, B. Langerock, A. Richter, N. Sudarchikova, V. Thouret, T. Warneke, C. Zerefos, Validation report of the CAMS near-real-time global atmospheric composition service. System evolution and performance statistics; Status up to 1 June 2016, Copernicus Atmosphere Monitoring Service (CAMS) report, CAMS84_2015SC1_D.84.1.4_2016Q3_201609, September 2016.*

*[nrt2016c] V. Huijnen, H.J. Eskes, A. Wagner, M. Schulz, S. Chabrillat, M. Ramonet, S. Basart, A. Benedictow, A.-M. Blechschmidt, Y. Christophe, H. Clark, E. Cuevas, H. Flentje, K.M. Hansen, U. Im, J. Kapsomenakis, B. Langerock, A. Richter, N. Sudarchikova, V. Thouret, T. Warneke, C. Zerefos, Validation report of the CAMS near-real-time global atmospheric composition service. System evolution and performance statistics; Status up to 1 March 2016, Copernicus Atmosphere Monitoring Service (CAMS) report, CAMS84_2015SC1_D.84.1.3_2016Q2_201605, May 2016.*

*[nrt2016d] V. Huijnen, H.J. Eskes, S. Basart, A. Benedictow, A.-M. Blechschmidt, S. Chabrillat, Y. Christophe, H. Clark, E. Cuevas, H. Flentje, K.M. Hansen, U. Im, J. Kapsomenakis, B. Langerock, A. Richter, N. Sudarchikova, M. Schulz, V. Thouret, A. Wagner, C. Zerefos, Validation report of the CAMS near-real-time global atmospheric composition service. System evolution and performance statistics; Status up to 1 December 2015, Copernicus Atmosphere Monitoring Service (CAMS) report, CAMS84_1_D1.2_201602, February 2016.*

*[nrt2015a] V. Huijnen, H.J. Eskes, S. Basart, A. Benedictow, A.-M. Blechschmidt, S. Chabrillat, Y. Christophe, E. Cuevas, H. Flentje, L. Jones, J. Kapsomenakis, B. Langerock, M. Razinger, A. Richter, M. Schulz, V. Thouret, A. Wagner, C. Zerefos, Validation report of the CAMS near-real-time global atmospheric composition service. System evolution and performance statistics; Status up to 1 September 2015, Copernicus Atmosphere Monitoring Service (CAMS) report, CAMS84_1_D1.1_201512, December 2015.*

*[reg2018a] Eskes, H.J., J. Douros, D. AKRITIDIS, T. Antonakaki, Y. Bennouna, A.-M. Blechschmidt, T. Bösch, H. Clark, C. Gielen, F. Hendrick, J. Kapsomenakis, S. KARTSIOS, E. Katragkou, D. MELAS, A. Mortier, E. Peters, K. Petersen, A. Piters, A. Richter, M. van Roozendael, M. Schulz, N. Sudarchikova, A. Wagner, P. Zanis, C. Zerefos, Validation of CAMS regional services: concentrations above the surface, Status update for September - November 2017, Copernicus Atmosphere Monitoring Service (CAMS) report, CAMS84_2015SC2_D84.5.1.16_D84.6.1.6_2017SON_v1, February 2018.*

*[reg2017a] Eskes, H.J., J. Douros, D. Akritidis, T. Antonakaki, A.-M. Blechschmidt, H. Clark, C. Gielen, F. Hendrick, J. Kapsomenakis, S. Kartsios, E. Katragkou, D. Melas, A. Mortier, E. Peters, K. Petersen, A. Piters, A. Richter, M. van Roozendael, M. Schulz, N. Sudarchikova, A. Wagner, P. ZANIS, C. Zerefos, Validation of CAMS regional services: concentrations above the surface, Status update for June - August 2017, Copernicus Atmosphere Monitoring Service (CAMS) report, CAMS84_2015SC2_D84.5.1.9_D84.6.1.4_2017JJA_v1, November 2017.*

*[reg2017b] Eskes, H.J., D. Akritidis, T. Antonakaki, A.-M. Blechschmidt, H. Clark, H.J. Eskes, C. Gielen, F. Hendrick, J. Kapsomenakis, E. Katragkou, S. Kontos, D. Melas, A. Mortier, E. Peters, A. Piters, A. Richter, M.*

*van Roozendael, M. Schulz, N. Sudarchikova, A. Wagner, P. Zanis, C. Zerefos, Validation of CAMS regional services: concentrations above the surface, Status update for September-November 2016, Copernicus Atmosphere Monitoring Service (CAMS) report, CAMS84_2015SC2_D.84.5.1.6_D84.6.1.1_2016SON_v1, February 2017.*

*[reg2016a] E. Katragkou, D. Akritidis, S. Kontos, P. Zanis, D. Melas, H. Eskes, Copernicus Atmosphere Monitoring Service (CAMS) report, Consistency between the global and regional modelling components of CAMS; Status update for July-August 2016, CAMS84_2015SC1_D84.6.2_201611_v1, November 2016.*

*[reg2016b] E. Katragkou, D. Akritidis, S. Kontos, P. Zanis, D. Melas, H. Eskes, Consistency between the global and regional modelling components of CAMS; Status update for May-June 2016, Copernicus Atmosphere Monitoring Service (CAMS) report, CAMS84_2015SC1_D84.6.2_201609_v1, September 2016.*

*[reg2018c] E. Katragkou, D. Akritidis, S. Kontos, P. Zanis, D. Melas, H. Eskes, Consistency between the global and regional modelling components of CAMS: Status update for February-April 2016, Copernicus Atmosphere Monitoring Service (CAMS) report, CAMS84_2015SC1_D.84.6.2-2016Q2_201606, June 2016.*

*[rea2018] H.J. Eskes, Y. Bennouna, M. Schulz, Y. Christophe, S. Basart, A. Benedictow, A.-M. Blechschmidt, S. Chabrillat, H. Clark, E. Cuevas, H. Flentje, K.M. Hansen, U. Im, J. Kapsomenakis, B. Langerock, K. Petersen, A. Richter, N. Sudarchikova, V. Thouret, A. Wagner, Y. Wang, C. Zerefos, Validation report of the CAMS global Reanalysis of aerosols and reactive gases, years 2003-2016, Copernicus Atmosphere Monitoring Service (CAMS) report, CAMS84_2015SC2_D84.7.1.4_Y14_v1.pdf, September 2018.*

*Solomos, S.; Kalivitis, N.; Mihalopoulos, N.; Amiridis, V.; Kouvarakis, G.; Gkikas, A.; Binietoglou, I.; Tsekeri, A.; Kazadzis, S.; Kottas, M.; Pradhan, Y.; Proestakis, E.; Nastos, P.T.; Marenco, F. From Tropospheric Folding to Khamsin and Foehn Winds: How Atmospheric Dynamics Advanced a Record-Breaking Dust Episode in Crete. Atmosphere 2018, 9, 240*

Copernicus Atmosphere Monitoring Service

ECMWF - Shinfield Park, Reading RG2 9AX, UK

Contact: info@copernicus-atmosphere.eu